PERIOD-N BIFURCATIONS IN MILLING

by

Andrew Honeycutt

A dissertation submitted to the faculty of
The University of North Carolina at Charlotte
in partial fulfillment of the requirements
for the degree of Doctor of Philosophy in
Mechanical Engineering

Charlotte

2018

Approved by:

_____
Dr. Tony Schmitz

_____
Dr. John Ziegert

_____
Dr. Matthew Davies

_____
Dr. Navid Goudarzi

ABSTRACT

ANDREW HONEYCUTT. Period-n bifurcations in milling.
(Under the direction of DR. TONY SCHMITZ)

Period-n bifurcations in milling operations are studied in this dissertation. Period-n bifurcations represent a special type of unstable dynamic behavior because they have a response period that is an integer multiple (n) of the forcing period. The existence of period-n bifurcations is demonstrated both through numerical simulation and experimental validation. Period-2, -3, -6, -7, -8, and -15 bifurcations are identified and verified by using once-per-tooth sampling (i.e. synchronous sampling) of in-process dynamic signals (time-varying system displacement and velocity) and the corresponding Poincaré maps. The sensitivity of period-n bifurcations to variations in the dynamic system's natural frequency and damping ratio is also studied both through numerical simulation and experiments.

A milling time domain simulation is presented that is capable of automatically detecting stable, unstable, and period-n behavior. This enhanced simulation allows the global existence of period-n bifurcations to be studied. Surface location error (SLE), or the difference between the commanded and actual surface locations due to milling dynamic behavior, and surface roughness is predicted and verified for period-2 and stable milling conditions.

ACKNOWLEDGMENTS

I would like to thank my academic advisor and mentor, Dr. Tony Schmitz, for his guidance and support over the past seven years through my undergraduate and graduate career. I was given the freedom to explore and research areas that interest me which allowed me to grow and learn in ways that I will never be able to quantify and for which I will always be grateful.

I would also like to thank my committee members, Dr. John Ziegert, Dr. Matthew Davies, and Dr. Navid Goudarzi for their support and assistance with completing this dissertation. I am especially grateful for all of the attention and care that Dr. Schmitz, Dr. Davies, and Dr. Ziegert put into their lectures and courses which inspired me to continue my education in graduate school.

I would also like to recognize and thank the faculty at the Center for Precision Metrology (CPM) at the University of North Carolina at Charlotte for all their assistance. I would like to thank Christopher Tyler, John Troutman, and Mark Rubeo for all of their guidance, assistance, and patience with me.

Finally, I would like to recognize and thank the Herschel and Cornelia Everett Foundation for the First-Year Graduate Fellowship as well as the National Science Foundation for providing financial assistance for my research.

TABLE OF CONTENTS

LIST OF FIGURES

LIST OF TABLES

CHAPTER 1: INTRODUCTION

1.1   Milling Stability

Computer numerically-controlled (CNC) milling is a subtractive manufacturing

method that can produce discrete parts with high tolerances. Surface roughness is also an

important metric to consider for CNC milled parts. Stable machining behavior is

desirable in order to achieve the required surface finish. Unstable machining, on the other

hand, leads to poorer surface finish. Milling behavior is typically defined as either stable

or unstable. Conventionally, two primary methods exist for determining whether or not

the milling behavior is stable: 1) record the sound (or other representative dynamic

signal) of the milling operation and evaluate it qualitatively or interrogate the frequency

content quantitatively; and 2) evaluate the surface roughness of the features that were

created. These two methods help determine whether or not a part was machined under

stable conditions. Prior research has been devoted to determining the limit of stability for

milling operations and this research has helped manufacturers produce high quality, high

precision parts.

1.2   Dynamic Stability

Dynamic stability in milling is a complex subject and has several metrics for

evaluation. Since stability is typically a binary characterization for milling operations, the

definition for dynamic stability for this study will be the synchronous response of a

dynamic system with the forcing frequency. In other words, the dynamic system is

vibrating at the same frequency as the forcing function. Consequently, this work will

apply a once-per-tooth sampling technique in order to determine if the dynamic response is stable or unstable.

1.3   Unstable Dynamics

Unstable dynamic behavior will be defined as anything that is not stable behavior. Different types of unstable behavior exist and will be described in the following sections. The goal of this research is to explore and describe a special type of unstable dynamic behavior known as a period-n bifurcation.

CHAPTER 2:   LITERATURE REVIEW

In science and engineering fields, new discoveries are typically followed by a burst of follow-on research activity and corresponding publications. These discoveries tend to serve as a catalyst to the research community and often result in new insights, improved understanding of fundamental phenomena, and enhanced modeling capabilities. For machining, one such period of rapid progress began in the mid-19th century [1]. During this time, self-excited vibrations were first described using time-delay differential equations [2]. The notion of "regeneration of waviness" was promoted as the feedback mechanism (time-delay term), where the previously cut surface combined with the instantaneous vibration state dictates the current chip thickness, force level, and corresponding vibration response [3-7]. This work resulted in analytical algorithms that were used to produce the now well-known stability lobe diagram that separates the spindle speed-chip width domain into regions of stable and unstable behavior [4-17] see Figure 2.1.
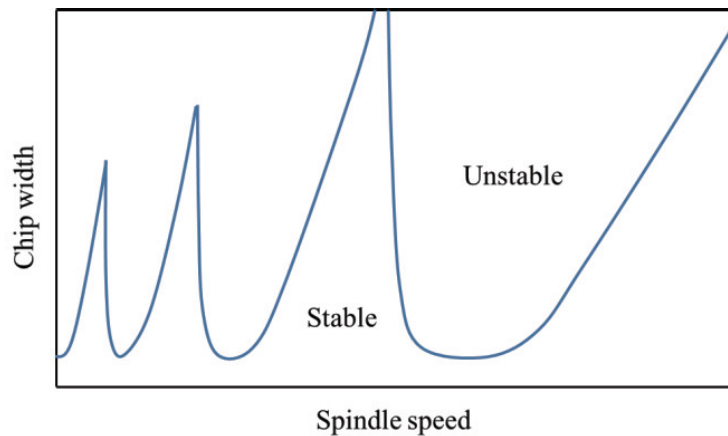
Figure 2.1: Example stability lobe diagram.

In 1998, a similar step forward in the understanding of machining behavior was realized. Davies et al. used once-per-revolution sampling to characterize the synchronicity of cutting tool motions (measured using a pair of orthogonal capacitance probes) with the tool rotation in milling [18]. This approach was an experimental modification of the Poincaré maps used to study state space orbits in nonlinear dynamics. They observed the traditional quasi-periodic chatter associated with the secondary (subcritical) Hopf, or Neimark-Sacker, bifurcation that can occur for systems described by periodic time-delay differential equations [19]. This was an expected result and was observed as an elliptical cluster of once-per-revolution sampled points in the x-y measurement plane perpendicular to the endmill axis as depicted in Figure 2.2 (a). This elliptical collection of points occurred because the chatter frequency was incommensurate with the tooth passing frequency and quasi-periodic behavior was obtained. However, they also recorded period-3 tool motion (i.e., motion that repeated with a period of three cutter revolutions) during partial radial immersion milling. This period-3 motion manifested itself as three distinct clusters of once-per-revolution sampled points in the x-y plane; see Figure 2.2(b). They noted that this behavior was "inconsistent with existing theory" [18].
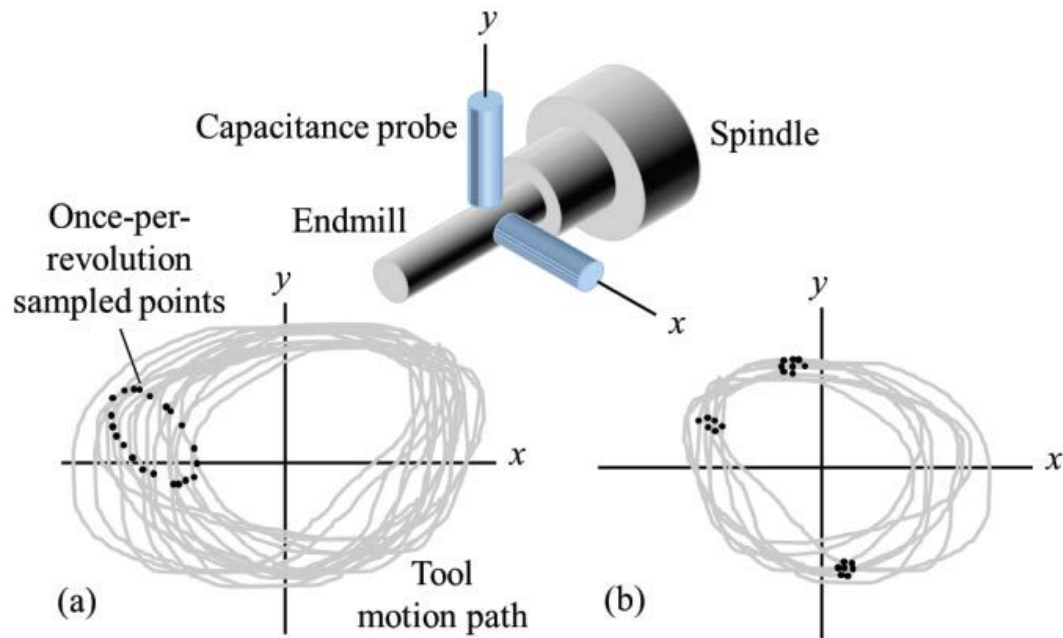
Figure 2.2: Once-per-revolution sampling of cutting tool motions (a) Hopf instability; (b) period-3 instability.

In 2000, Davies et al. further examined the stability of highly interrupted (or low radial immersion) milling [20]. They developed a two-stage map to describe:

1. non-cutting motions governed by an analytical solution (damped free vibration); and

2. motions during cutting using an approximation (fixed tool position with a change in momentum).

They reported a doubling of the number of optimally stable spindle speeds when the time in cut is small (i.e., low radial depth of cut). These extra spindle speeds, Ω (rpm), were defined using the (dominant) damped natural frequency, f_d (Hz), of the structural dynamics, and number of cutter teeth, N_t:

6

$$\Omega = \frac{2f_d}{N_t j} 60 \tag{1}$$

where $j = 1, 3, 5, \ldots$ The traditional secondary Hopf bifurcation lobes correspond to $j = 2, 4, 6, \ldots$ Milling experiments confirmed the new, low radial immersion best speeds.

In 2001, Moon and Kalmár-Nagy reviewed the "prediction of complex, unsteady and chaotic dynamics" in machining [19]. They listed the various contributors to nonlinear behavior, including the loss of tool-workpiece contact due to large amplitude vibration and workpiece material constitutive relations, and highlighted previous applications of nonlinear dynamics methods to the study of chatter [21-26]. They also specified the use of phase-space methods, such as Poincaré maps, to identify changes in machining process dynamics.

Time domain simulation offers a powerful tool for exploring milling behavior and has been applied to identify instability [27-28]. For example, Zhao and Balachandran implemented a time domain simulation which incorporated loss of tool-workpiece contact and regeneration to study milling [29]. They identified secondary Hopf bifurcation and suggested that "period-doubling bifurcations are believed to occur" for low radial immersions [29]. They included bifurcation diagrams for limited axial depth of cut ranges at two spindle speeds to demonstrate the two bifurcation types. Davies et al. extended their initial work in 2002 to present the first analytical stability boundary for highly interrupted machining [30]. It was based on modeling the cutting process as a kicked harmonic oscillator with a time delay and followed the two-stage map concept described previously [20]. They used the frequency content of a microphone signal to establish the existence of both secondary Hopf and period-2 (period-doubling or flip) instabilities.

Mann et al. also provided experimental validation of secondary Hopf and period-2 instabilities for up and down milling [31]. They reported "a kind of period triple phenomenon" [31] observed using the once-per-revolution sampled displacement signal recorded from a single degree of freedom flexure-based machining platform.

The semi-discretization, time finite element analysis, and multi-frequency methods were also developed to produce milling stability charts that demonstrate both instabilities [32-36]. In [37], it was shown using the semi-discretization method that the period-2 bifurcation exhibits closed, lens-like, curves within the secondary Hopf lobes, except for the highest speed stability lobe; see Figure 2.3, where b is the axial depth of cut for peripheral milling. Simultaneous quasi-periodic (secondary Hopf) and period-2 bifurcation behavior was also observed. It was reported that this "combination" behavior occurred at unstable axial depths of cut above the period-2 lobes. Additionally, period-3 instability was seen and it was noted that this "periodic chatter" with period-3 (or higher) always occurred above a secondary Hopf stability limit. The same group [38] reported further experimental evidence of quasi-periodic (secondary Hopf), period-2, period-3, period-4, and combined quasi-periodic and period-2 chatter, depending on the spindle speed-axial depth values for a two degree of freedom dynamic system. A perturbation analysis was performed in [39] to identify the secondary Hopf and period-2 instabilities. Additionally, numerical integration was implemented to construct a bifurcation diagram for a selected spindle speed that demonstrated the transition from stable operation to quasi-periodic chatter as the axial depth is increased.
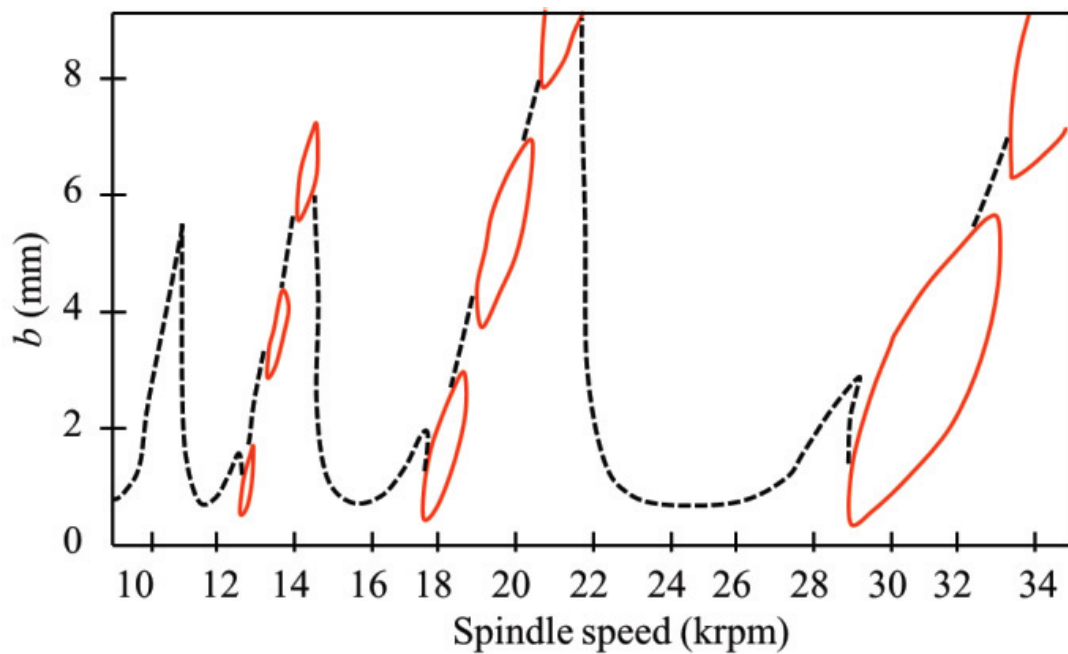
Figure 2.3: Stability lobe diagram with Hopf (dashed) and period-2 (solid) stability boundaries [37].

Stépán et al. continued to explore the nonlinear aspects of milling behavior in 2005 [40]. They described stable period-2 motion where the tool does not contact the workpiece in each tooth period (even in the absence of runout). For a two flute cutter, for example, only one tooth contacts the workpiece per revolution; they referred to this condition as the "fly over effect" and included a bifurcation diagram for these proposed stable and unstable period-2 oscillations.

The effect of the helix angle on period-2 instability was first studied by [41]. They found that, depending on the helix angle, the closed, lens-like, curves within the secondary Hopf lobes change their size and shape. They also found that these closed islands of stability can appear even in the highest speed stability lobe (in contrast to the results when helix angle is not considered). Experimental results were provided. This

work was continued in [42], where the authors emphasized that at axial depths equal to

the axial pitch, *p*, of the cutter teeth:

$$p = \frac{d\pi}{N_t \tan(\gamma)} \tag{2}$$

the equation of motion becomes an autonomous delay differential equation so the period-

2 instability is not possible (*d* is the cutter diameter, N_t is the number of teeth, and γ is the

helix angle). Therefore, axial depths that are integer multiples of *p* form the horizontal

boundaries between the stability islands. Patel et al. also studied the helix effect in up and

down milling using the time finite element approach [43].

CHAPTER 3: STABILITY OF DYNAMIC RESPONSE

3.1   Poincaré Maps and Once-per-tooth Sampling in Milling

In this study, Poincaré maps were developed using both experiments and

simulations. For the experiments, the displacement and velocity of the flexible workpiece

were recorded and then sampled once-per-tooth period. In simulation, the displacement

and velocity were predicted, but the same sampling strategy was applied. By plotting the

displacement versus velocity, the phase space trajectory can be observed in both cases.

The once-per-tooth period samples are then superimposed and used to interrogate the

milling process behavior. For stable cuts, the motion is periodic with the tooth period, so

the sampled points repeat and a single grouping of points is observed. When secondary

Hopf instability occurs, the motion is quasi-periodic with tool rotation because the chatter

frequency is (generally) incommensurate with the tooth passing frequency. In this case,

the once-per-tooth sampled points do not repeat, and they form an elliptical distribution.

For period-2 instability, on the other hand, the motion repeats only once every other cycle

(i.e., it is a sub-harmonic of the forcing frequency). In this case, the once-per-tooth

sampled points alternate between two solutions. For period-n instability, the sampled

points appear at n locations.

3.2   Bifurcation Diagrams

A bifurcation diagram enables the evolution of system behavior (e.g., tool motion)

with a control variable of interest (such as axial depth of cut in milling) to be efficiently

observed. The diagram uses the periodic sampling strategy to identify periodic (or

aperiodic) responses over the selected range of the control variable. For milling, the tool

motion in the feed, *x*, or *y* direction is sampled once-per-spindle revolution for a given axial depth of cut (and fixed spindle speed). This produces a sequence of points over multiple cutter revolutions (see Figure 2.2 for example). This collection of points is then truncated to remove the transient portion of the motion (typically the first few milliseconds).

For stable milling with motion that is periodic with the cutting force (i.e., only forced vibrations are present), these sampled points repeat each revolution because the cutting force and subsequent vibration response is periodic with the spindle rotation. The superposition of all these repeated points therefore gives a single point (or nearly so) on a bifurcation diagram of axial depth (horizontal axis) versus once-per-revolution sampled tool motion (vertical axis).

For a higher axial depth at the same spindle speed, secondary Hopf instability may occur and then the motion is quasi-periodic with tool rotation because the chatter frequency is (generally) incommensurate with the tooth passing frequency. In this case, the once-per-revolution sampled points do not repeat and they form a distribution (as shown in Figure 2.2(a)). When plotted on the bifurcation diagram, this distribution appears as a vertical "spread" of points.

For period-2 instability, on the other hand, the motion repeats only once every other cycle (i.e., it is a sub-harmonic of the forcing frequency). In this case, the once-per-revolution sampled points alternate between two solutions. On the bifurcation diagram, the points appear in two distinct vertical locations (recall that the vertical axis is the sampled tool motion). For period-n instability, the sampled points appear at n vertical

locations. The bifurcation diagram construction from results at multiple axial depths of

cut for a selected spindle speed is depicted in Figure 3.1.
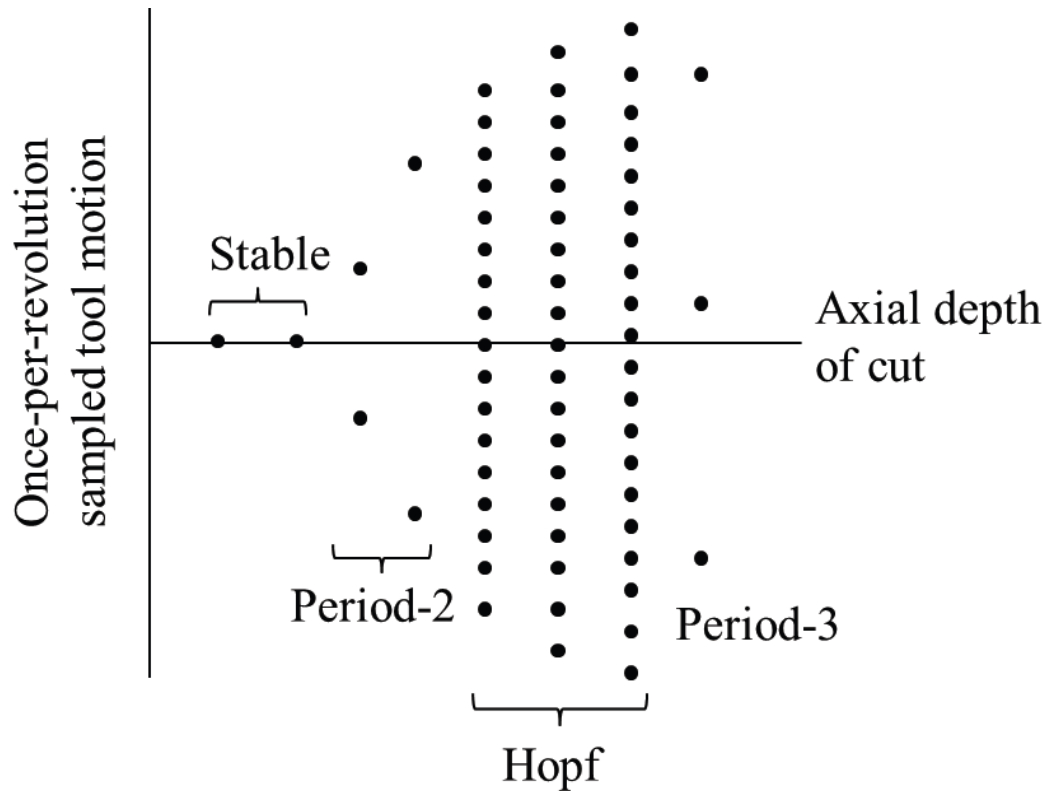
Figure 3.1: Description of stable/unstable behavior for a milling bifurcation diagram.

3.3   Stable, Unstable, and Period-n Responses

A powerful interrogation tool for milling dynamics is the Poincaré map, where the

tool (or workpiece) displacement is plotted versus the velocity and then sampled once-

per-tooth period. This sampling establishes the synchronicity of the motion (response)

with the cutting force (excitation). For stable cutting conditions, only forced vibration is

present, and the sampled point repeats for each tooth passage. For unstable cutting, on the

other hand, the repetition of a single point is not observed, and the character of the

sampled points identifies the type of instability: secondary Hopf or period-n bifurcations.

As an example, consider symmetric, single degree-of-freedom dynamics for 5%

radial immersion up milling with a spindle speed of 30,000 rpm. The modal parameters

are: 721 Hz natural frequency, 0.009 viscous damping ratio, and 4.1×10^5 N/m stiffness.

The cutter has one tooth, a 45 deg helix angle, and an 8mm diameter. The aluminum

alloy cutting force coefficients are: $k_t = 604 \times 10^6$ N/m^2 and $k_n = 223 \times 10^6$ N/m^2 (zero edge

coefficients). The time-dependent x vibration, as well as the once-per-tooth sampled

points, for a stable cut (0.5 mm axial depth), is displayed in Figure 3.2. The

corresponding Poincaré map is also shown; the sampled points repeat with each tooth

period for the forced vibration response.
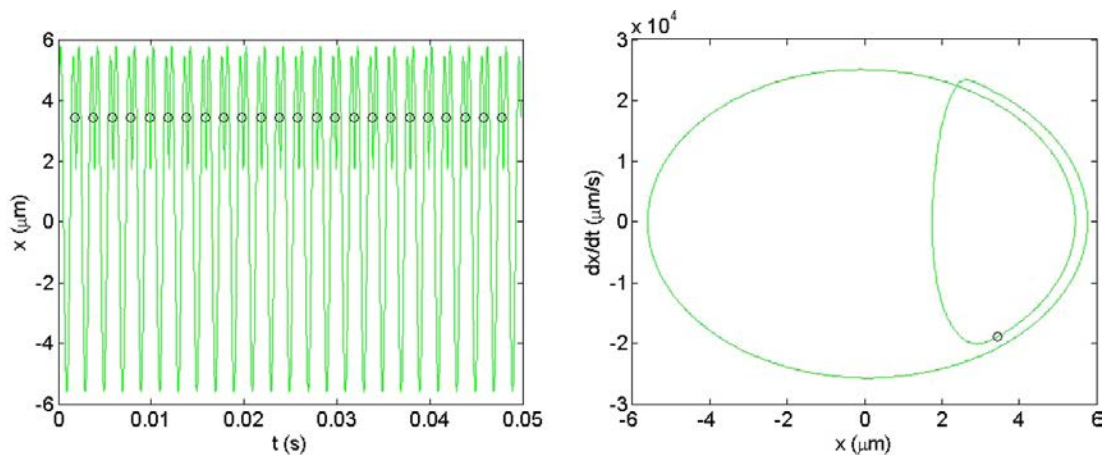
Figure 3.2: Stable cut, $b = 0.5$ mm (left) time response for x (feed) direction displacement; (right) Poincaré map which plots x displacement versus velocity. The once-per-tooth sampled points are displayed as circles

Figure 3.3 shows the results for a period- 2 bifurcation (2.5 mm); here, two clusters of points occur.
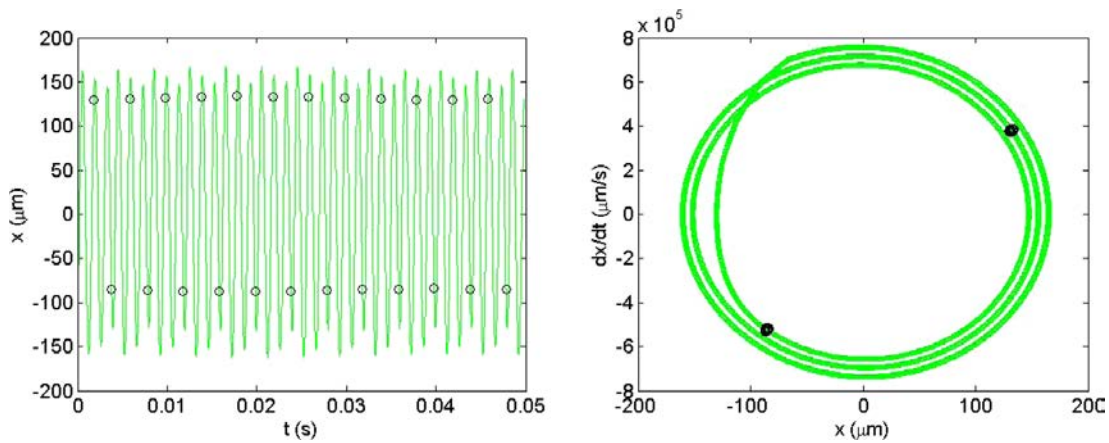
Figure 3.3: Period-2, $b = 2.5$ mm (left) time response for x (feed) direction displacement; (right) Poincaré map

Figure 3.4 represents a secondary Hopf bifurcation (5 mm); an elliptical grouping of points is seen in the Poincaré map for the quasi-periodic response.
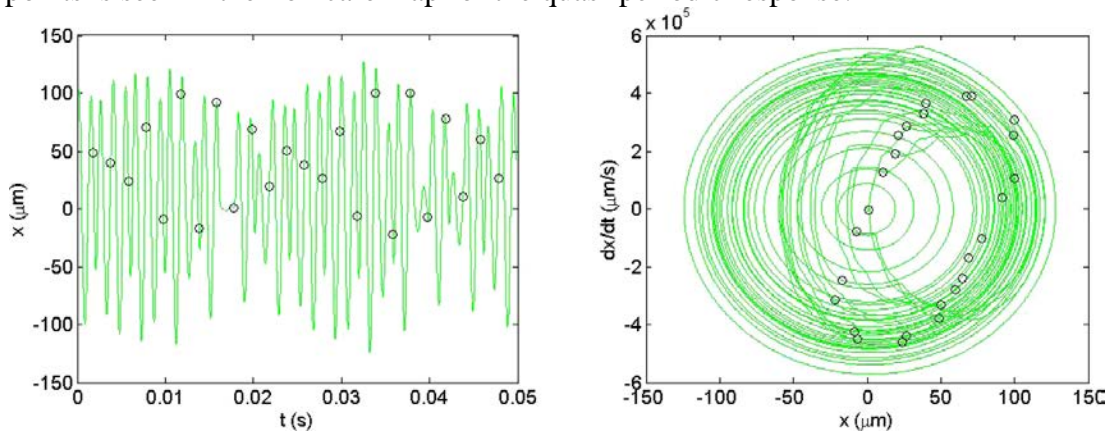
Figure 3.4: Secondary Hopf, $b = 5.0$ mm (left) time response; (right) Poincaré map

This transition in behavior with increasing axial depth (30,000 rpm spindle speed) is conveniently presented using a bifurcation diagram, where the sampled displacement points from the Poincaré maps (e.g., Figure 3.2, 3.3, and 3.4) are plotted versus the control variable, which is axial depth of cut in this case. In the diagram, a stable cut appears as a single point (i.e., the repeating sampled points) for the selected axial depth. A period-2 bifurcation appears as a pair of points offset from each other in the vertical

direction. An example diagram is provided in Figure 3.5, where the stable depths up to

0.77 mm (labeled A, representing Figure 3.2), as well as the period-2 from 0.77 mm to

2.59 mm (B, Figure 3.3) and secondary Hopf (C, Figure 3.4) bifurcation depths, are

observed. The bifurcation diagram also reveals a combination of period-2 and secondary

Hopf instabilities (D) and period-7 bifurcation (E).
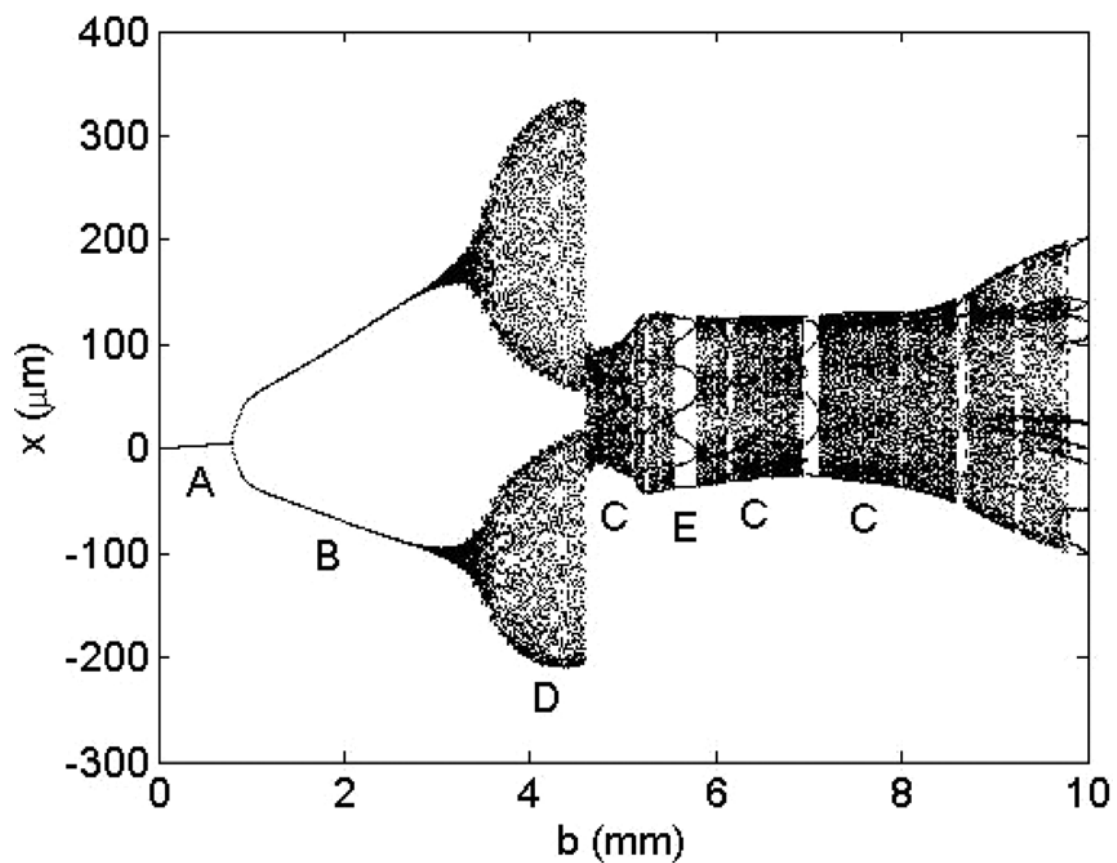
Figure 3.5: Bifurcation diagram for selected spindle speed (30,000 rpm) and system dynamics.

CHAPTER 4: TIME DOMAIN MILLING SIMULATION

Time-domain simulation entails the numerical solution of the governing equations of

motion for milling in small time steps. It is well-suited to incorporating all the intricacies

of milling dynamics, including the nonlinearity that occurs if the tooth leaves the cut due

to large amplitude vibrations and complicated tool geometries (including runout, or

different radii, of the cutter teeth, non-proportional teeth spacing, and variable helix). The

simulation is based on the Regenerative Force, Dynamic Deflection Model described by

[27]. As opposed to stability lobe diagrams that provide a "global" picture of the stability

behavior, time-domain simulation provides information regarding the "local" cutting

force and vibration behavior (at the expense of computational efficiency) for the selected

cutting conditions. The simulation proceeds as follows:
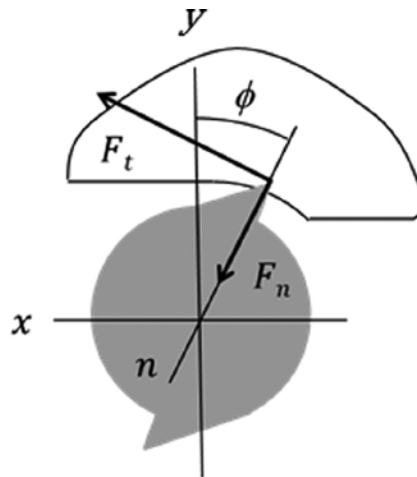
Figure 4.1: Milling simulation geometry. The normal and tangential direction cutting forces, F_n and F_t, are identified. The fixed x and y directions, as well as the rotating normal direction, n, are also shown. The angle ϕ defines the tooth angle. The tool feed is to the right for the clockwise tool rotation and the axial depth is in the z direction.

1. the instantaneous chip thickness is determined using the vibration of the current and previous teeth at the selected tooth angle

2. the cutting force components in the tangential (t) and normal (n) directions are calculated using

$$F_t(t) = k_{tc}bh(t) + k_{te}b \tag{3}$$

$$F_n(t) = k_{nc}bh(t) + k_{ne}b \tag{4}$$

where b is the axial depth of cut, $h(t)$ is the instantaneous chip thickness, and the cutting force coefficients are identified by the subscripts t or n for direction and c or e for cutting or edge effect

3. the force components are used to find the new displacements by numerical solution of the differential equations of motion in the x (feed) and y directions

$$m_x\ddot{x} + c_x\dot{x} + k_x x = F_t(t)\cos(\phi) + F_n\sin(\phi) \tag{5}$$

$$m_y\ddot{y} + c_y\dot{y} + k_y y = F_t(t)\sin(\phi) - F_n\cos(\phi) \tag{6}$$

4. the tooth angle is incremented and the process is repeated. Modal parameters are used to describe the system dynamics in the x (feed) and y directions, where multiple degrees of freedom in each direction can be accommodated.

The instantaneous chip thickness depends on the nominal, tooth angle-dependent chip thickness, the current vibration in the direction normal to the surface, and the vibration of previous teeth at the same angle. The chip thickness can be expressed using the circular tool path approximation as

$$h(t) = f_t\sin(\phi) + n(t - \tau) - n(t) \tag{7}$$

where f_t is the commanded feed per tooth, ϕ is the tooth angle, n is the normal direction, and τ is the tooth period. The tooth period is defined as

$$\tau = \frac{60}{\Omega N_t} \, (sec) \tag{8}$$

where Ω is the spindle speed in rpm and N_t is the number of teeth. The vibration in the direction of the surface normal for the current tooth depends on the x and y vibrations as well as the tooth angle according to

$$n = x sin(\phi) - y cos(\phi) \tag{9}$$

For the simulation, the strategy is to divide the angle of the cut into a discrete number of steps. At each small time step, dt, the cutter angle is incremented by the corresponding small angle, $d\phi$. This approach enables convenient computation of the chip thickness for each simulation step because: 1) the possible teeth orientations are predefined; and 2) the surface created by the previous teeth at each angle may be stored. The cutter rotation

$$d\phi = \frac{360}{SR} \, (deg) \tag{10}$$

depends on the selection of the number of steps per revolution, SR. The corresponding time step is

$$dt = \frac{60}{SR \cdot \Omega} \, (sec) \tag{11}$$

A vector of angles is defined to represent the potential orientations of the teeth as the cutter is rotated through one revolution of the circular tool path, $\phi = [0, d\phi, 2d\phi, 3d\phi, \ldots$

, $(SR - 1)\, d\phi$]. The locations of the teeth within the cut are then defined by referencing entries in this vector.

In order to accommodate the helix angle for the tool's cutting edges, the tool may be sectioned into a number of axial slices. Each slice is treated as an individual straight tooth endmill, where the thickness of each slice is a small fraction, db, of the axial depth of cut, b. Each slice incorporates a distance delay

$$r\chi = db \cdot \tan(\gamma) \tag{12}$$

relative to the prior slice (nearer the cutter free end), which becomes the angular delay between slices:

$$\chi = db \cdot \frac{\tan(\gamma)}{r} = 2db \cdot \frac{\tan(\gamma)}{d}\,(rad) \tag{13}$$

for the rotating endmill, where d is the endmill diameter and γ is the helix angle. In order to ensure that the angles for each axial slice match the predefined tooth angles, the delay angle between slices is $\chi = d\phi$. This places a constraint on the db value. By substituting $d\phi$ for χ and rearranging, the required slice width is

$$db = \frac{d \cdot d\phi}{2\tan(\gamma)} \tag{14}$$

Once the x and y direction displacements are determined (Eqs. (5) and (6)), the final spatial trajectory for each tooth is determined by summing these vibration-induced displacements with the nominal cycloidal motion of the teeth due to the combined translation and rotation. This final spatial trajectory is finally used to define the machined surface and, subsequently, to predict the SLE and surface roughness. The nominal

cycloidal motion components in the *x* and *y* directions are defined in Eqs.(15) and (16) ,

where *i* is the time-step index and *Δf* is the linear feed per time-step (see Eq. (17)).

$$x_{nom} = r\sin(\phi) + i\Delta f \tag{15}$$

$$y_{nom} = r\cos(\phi) \tag{16}$$

$$\Delta f = \frac{f_t N_t}{SR} \tag{17}$$

This simple description can be extended to include:

(1)   Multiple tool modes – the *x* and *y* forces are used to calculate the

acceleration, velocity, and displacement for each tool mode (represented

by the modal parameters) and the results are summed in each direction.

(2)   Flexible workpiece – the *x* and *y* forces are also used to determine the

workpiece deflections, again by numerical integration, and the relative

tool-workpiece vibration is used to calculate the instantaneous chip

thickness.

(3)   Runout of the cutter teeth – the chip thickness is updated by the runout of

the current tooth.

(4)   Unequal teeth spacing – the tooth angle vector is modified to account for

the actual tooth pitch.

Using the time-domain simulation approach, the forces and displacements may be

calculated. These results are then once-per-revolution sampled to generate the bifurcation

diagrams.

4.1   Automated Stability Identification

While bifurcation diagrams (e.g., Figure 4.3) provide an effective visual

representation of the stability behavior using the once-per-tooth sampled data, it is also

beneficial to represent the process stability over a large domain of spindle speeds (in

addition to axial depths). This is the traditional stability lobe diagram. To construct this

stability map, time domain simulations are completed over the desired grid of spindle

speed and axial depth values. A primary challenge for time-domain simulation, however,

is automatically establishing the stability limit. In this research, a new stability criterion

based on the once-per-tooth sampled data is implemented. The metric builds on the

approach in [44–46] where the standard deviation of the periodically sampled milling

audio signal was calculated.

The stability metric is

$$M = \sum_{i=2}^{N} \frac{|x_s(i) - x_s(i-1)|}{N} \tag{18}$$

where x_s is the vector of once-per-tooth sampled x displacements and N is the length of

the x_s vector. Other variables, such as y displacement or cutting force could be selected

as well. With this new stability metric, the absolute value of the differences in successive

sampled points is summed and then normalized. As seen in Figure 3.2, the sampled

points repeat for a stable cut, so the M value is ideally zero. For unstable cuts, however,

$M > 0$.

As an example, consider symmetric, single degree-of-freedom dynamics for 5%

radial immersion up milling with a spindle speed of 30,000 rpm. The modal parameters

are: 721 Hz natural frequency, 0.009 viscous damping ratio, and 4.1×10^5 N/m stiffness.

The cutter has one tooth, a 45 deg helix angle, and an 8 mm diameter. The aluminum

alloy cutting force coefficients are: $k_{tc} = 604 \times 10^6$ N/m^2 and $k_{nc} = 223 \times 10^6$ N/m^2 (zero

edge coefficients). An example stability map is provided in Figure 4.2, where the spindle

speed resolution is 10 rpm, the axial depth resolution is 0.1 mm, and the initial transients

(i.e., the homogeneous part of the differential equation solution) were removed prior to

analysis. Figure 4.2 is a height map of M values, where only one contour line is plotted.

This contour represents an M value of 1 μm and identifies the stability limit as a function

of spindle speed and axial depth ($M = 0$ was not used due to limited numerical precision;

instead, the small value of 1 μm was selected).
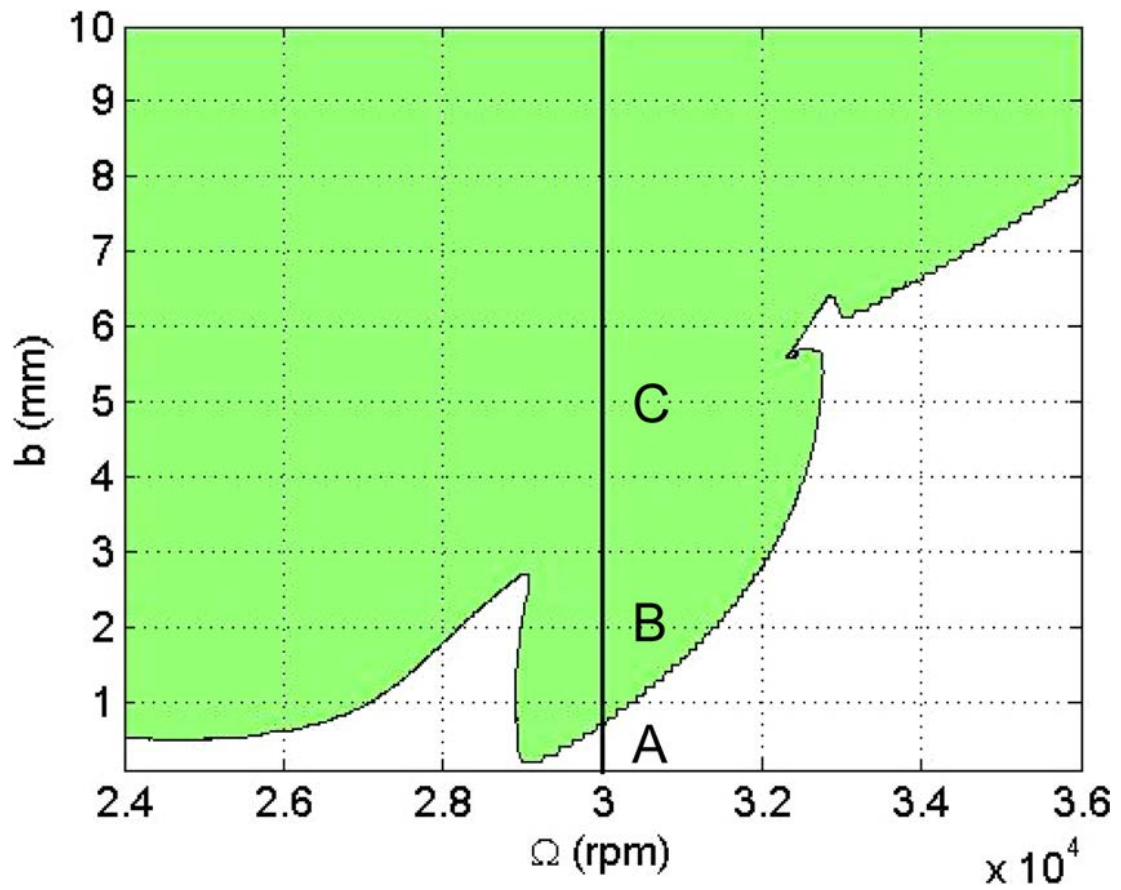
Figure 4.2: Simulated stability map ($M = 1\ \mu$m contour)

Figure 4.2 includes a vertical line at 30,000 rpm. This is the range of axial depths used to generate the bifurcation diagram in Figure 4.3.
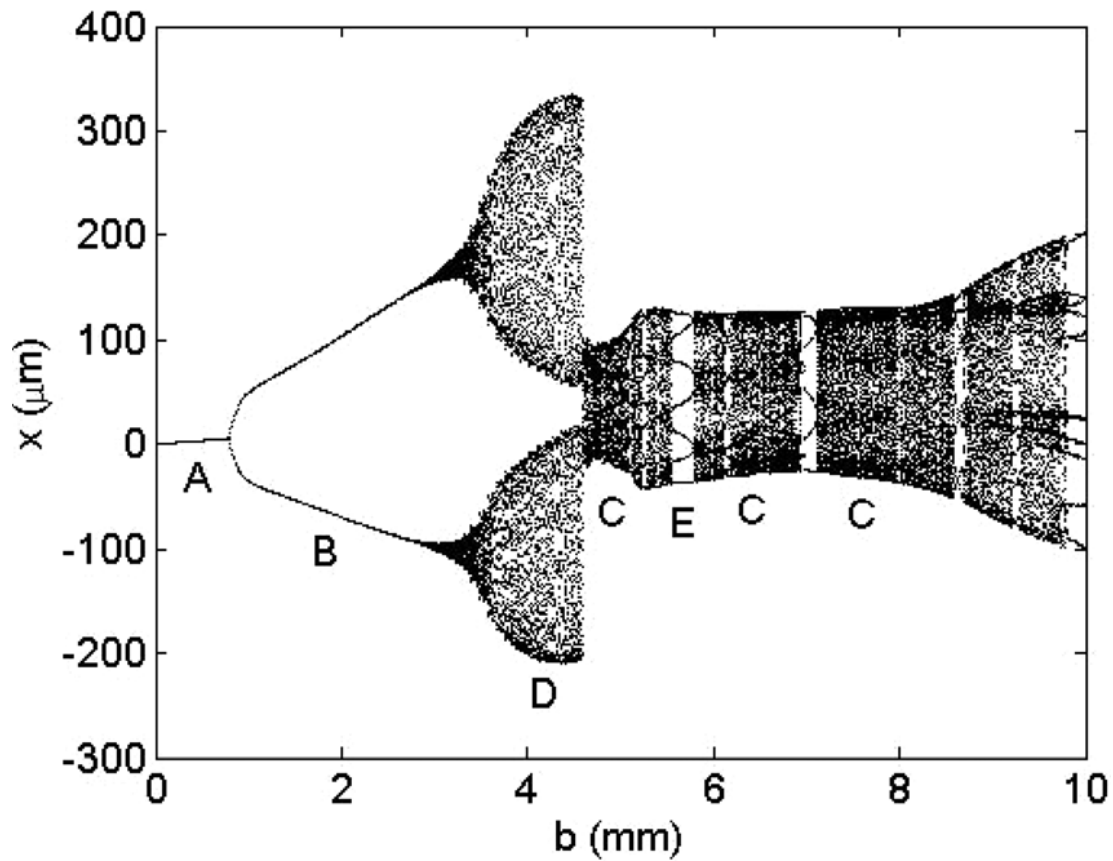
Figure 4.3: Bifurcation diagram for selected spindle speed (30,000 rpm) and system dynamics

It is seen that stable behavior is achieved up to 0.77 mm (A). There is then a transition to

the period-2 bifurcation (B); this is the elliptical-shaped zone immediately above the

stability limit in the 29,000-33,000 rpm range. At higher axial depths, there is a transition

to secondary Hopf instability (C). The stability diagram does not provide the amplitude

and bifurcation behavior, however. In this way, the bifurcation diagram can be

considered to be a data-rich vertical slice of the stability lobe diagram.

4.2   Automated Subharmonic Interrogation for Period-n Identification

Periodic sampling at the tooth period, τ, enables stable and unstable zones to be identified, but this approach does not distinguish between secondary Hopf and period-n instabilities. Consider an example where the workpiece (flexure) dynamics were identified by modal testing to be: 163 Hz natural frequency, 0.007 viscous damping ratio, and 5.2×10^6 N/m stiffness in the flexible (feed) direction. The dynamics for the 19.1 mm diameter, 30 deg helix angle tool (one tooth) were symmetric: 1050 Hz natural frequency, 0.045 viscous damping ratio, and 3.85×10^7 N/m stiffness. The aluminum alloy cutting force coefficients were: $k_t = 792 \times 10^6$ N/m^2, $k_n = 392 \times 10^6$ N/m^2, $k_{te} = 26 \times 10^3$ N/m, and $k_{ne} = 28 \times 10^3$ N/m. As shown in Figure 4.4, the unstable zone is identified, but the different types of instabilities of are not.

A simulated stability map for up milling with a radial depth of 5 mm (26% radial immersion) and 0.15 mm feed per tooth was generated for axial depths of cut from 0.1 mm to 8 mm in steps of 0.1 mm and spindle speeds from 3300 rpm to 4300 rpm in steps of 10 rpm. See Figure 4.4, where the initial transients were removed prior to analysis using Eq. (18) (i.e., the final 75 tooth periods of a 750 tooth period simulation were analyzed). A single filled contour at $M = 1$ μm is displayed to distinguish between stable (white zone below the contour) and unstable (dark zone above the contour) conditions. An unstable "island" is seen starting at approximately 4000 rpm within the large stable zone.
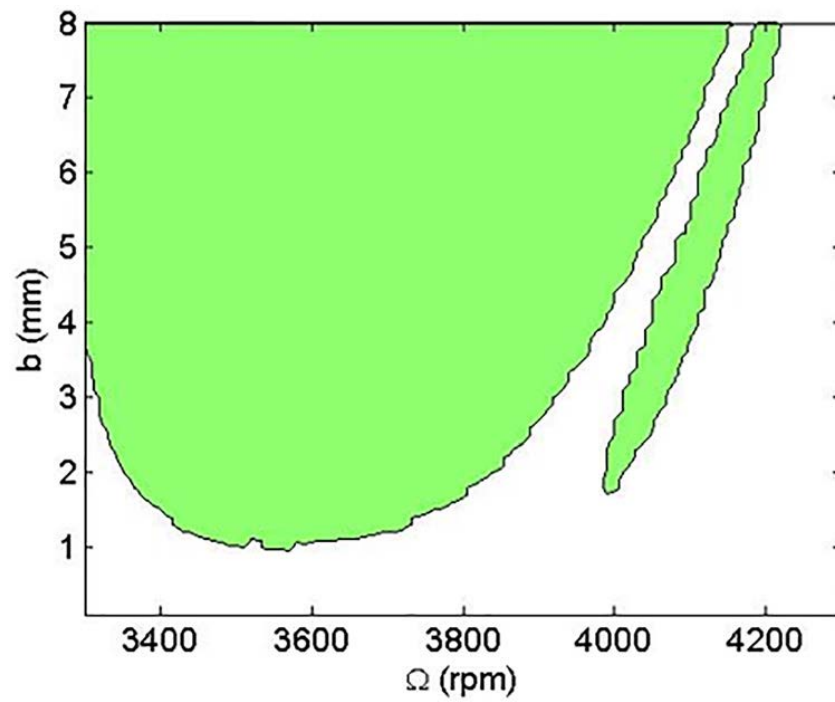
Figure 4.4: Simulated stability map for 26% radial immersion ($M = 1$ μm contour)

For example, from Figure 4.5 it is known that both secondary Hopf and period-3

bifurcations are present at 3800 rpm, but both simply appear in the unstable zone in

Figure 4.4.
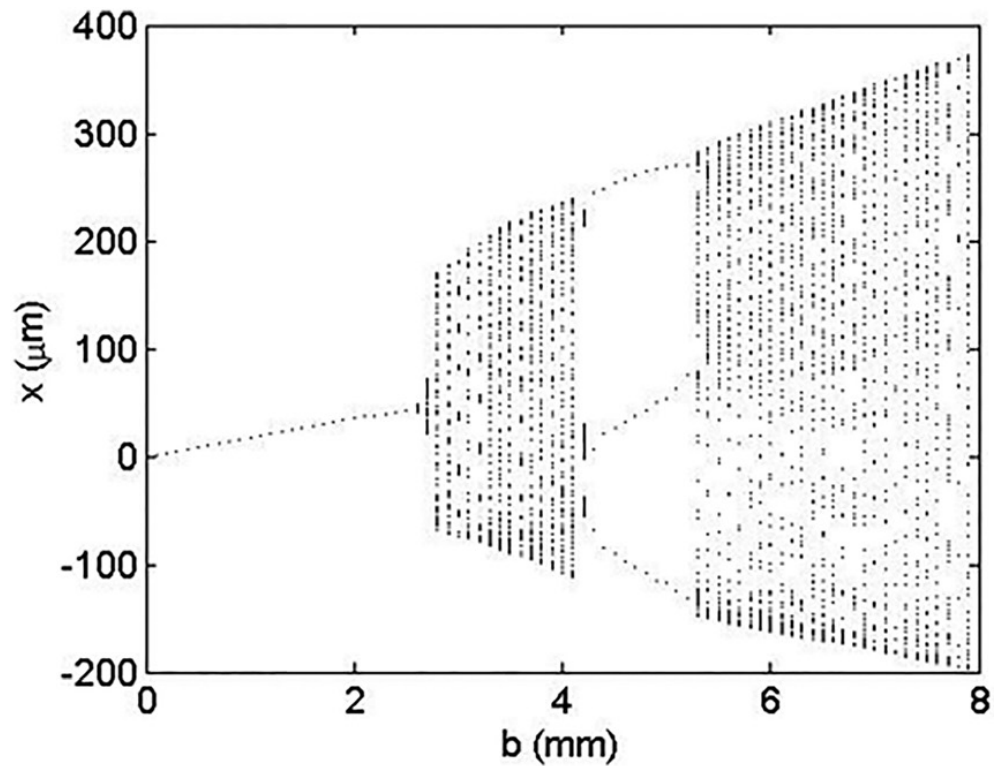
Figure 4.5: Simulated bifurcation diagram for 3800 rpm, 26% radial immersion

However, using subharmonic sampling at $n\tau$ (n = 2, 3, 4,…), the corresponding period-n bifurcations can be separately established. For example, when sampling at 2τ, the stability metric becomes "blind" to period-2 bifurcations. By sampling at every other tooth passage (2τ), the period-2 behavior appears as synchronous motion (stable). The same is true for period-3 bifurcations if the sampling interval is 3τ, and so on.

Considering the same flexure-based dynamic system, a simulation was performed for a spindle speed of 4070 rpm at an axial depth of 3.6 mm. This is within the unstable island in Figure 4.4. The time history and Poincaré map are displayed in the top row of Figure 4.6 for once-per-tooth sampling.
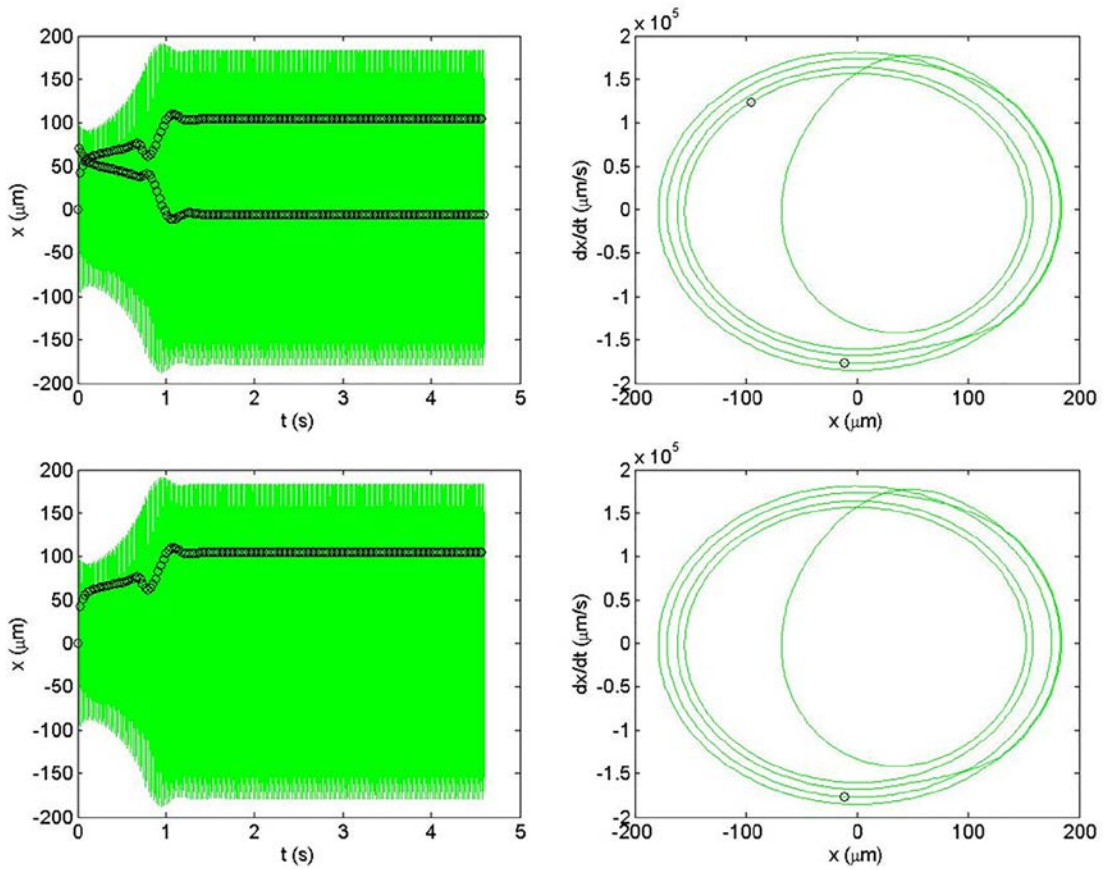
Figure 4.6: Simulation results for a spindle speed of 4070 rpm at an axial depth of 3.6 mm. The workpiece *x* and *y* displacements are shown. (Top row) Time history (left) and Poincaré map (right) for once-per-tooth sampling (τ sampling period). (Bottom row) Time history (left) and Poincaré map (right) for subharmonic sampling at 2τ.

A period-2 bifurcation is observed. The *M* value is 106.7 μm for the period-2 instability; this value was calculated from the flexure (workpiece) *x* direction displacement for the final 75 tooth periods of a 750 tooth period simulation. The bottom row shows the results for 2τ subharmonic sampling. The metric for this case is

$$M2 = \frac{\sum_{i=2}^{N}|x_{s2}(i)-x_{s2}(i-1)|}{N} \qquad (19)$$

where x_{s2} is the vector of x displacements sampled once every other tooth period (i.e., a 2τ sampling period), and N is the length of the x_{s2} vector. It is observed that the cut now appears to be stable; the $M2$ value is 1.2×10^{-9} μm $\cong 0$. Generically, the metric can be expressed as shown in Eq. (20), where the integer n = 1, 2, 3,… defines the sampling period (i.e., nτ)

$$Mn = \frac{\sum_{i=2}^{N}|x_{sn}(i)-x_{sn}(i-1)|}{N} \qquad (20)$$

Next, the stability map shown in Figure 4.4 was developed using nτ sampling with n = 1, 2, 3, and 4. These results are provided in Figure 4.7. In Figure 4.7(a), once-per-tooth sampling (τ sampling period) was applied to calculate $M1$ using Eq. (20). A single contour is plotted at $M1 = 1$ μm. For Figure 4.7(b), the sampling period is 2τ. It is seen that the unstable island no longer appears. This follows from Figure 4.6, where it is seen that the 2τ sampling is blind to period-2 bifurcations. A single contour is plotted at $M2 = 1$ μm according to Eq. (20). In Figure 4.7(c), 3τ sampling is applied. The period-2 bifurcation zone reappears as shown in Figure 4.7(a), but a new "stable" zone is also visible. This is the region of period-3 bifurcations that is demonstrated in Figure 4.5, but was not previously visible with the once-per-tooth sampling approach. Figure 4.7(d) displays the results for 4τ sampling. The period-2 bifurcations are again eliminated because 2τ is a factor of 4τ. However, a new stable band also appears to the left of the period-3 bifurcation zone in Figure 4.7(c). This new band identifies period-4 bifurcations and would not have been discovered without subharmonic sampling. In Figures 4.7(c)

and 4.7(d), the stability metric was updated to accommodate the new sampling periods,

and a single contour at a metric value of 1 μm was plotted.
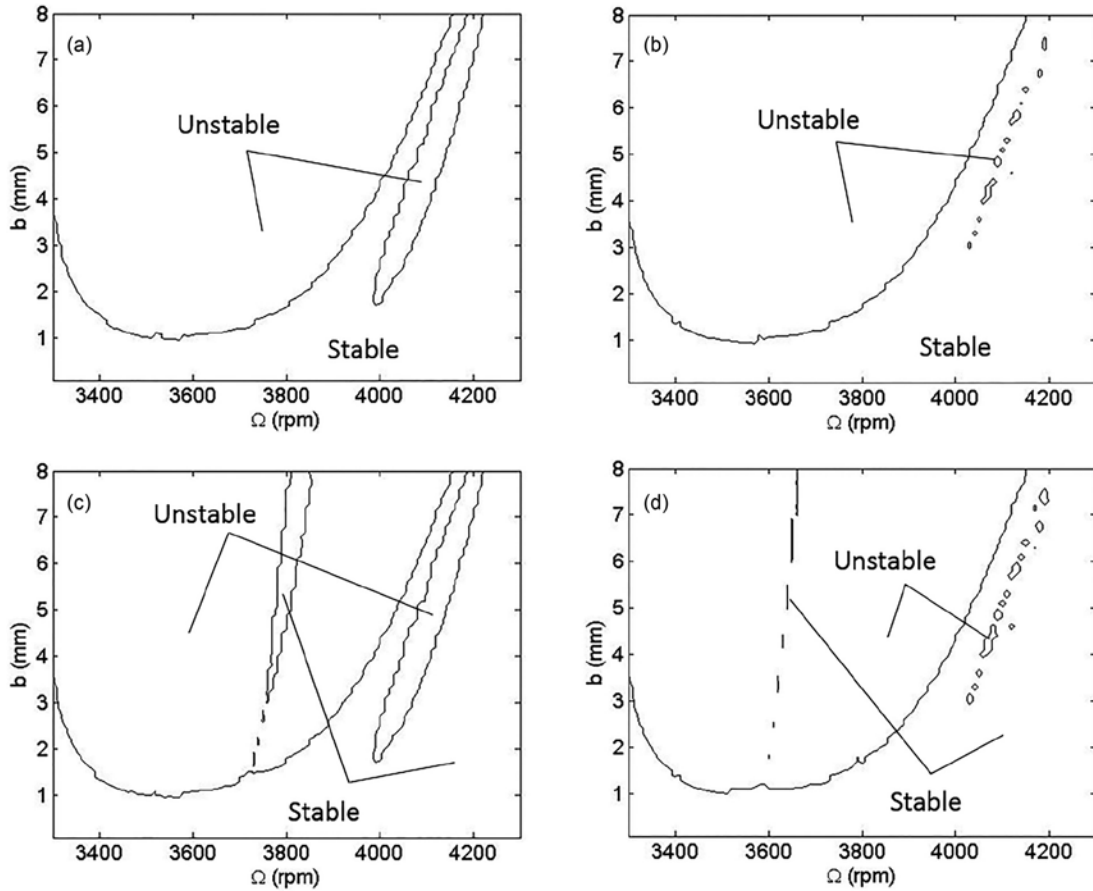
Figure 4.7: (a) Once-per-tooth sampling (τ sampling period), (b) 2τ sampling period, (c) 3τ sampling period, and (d) 4τ sampling period. The zones that appear to be stable and unstable, depending on the sampling period, are marked.

To illustrate the period-4 bifurcations in Figure 4.7(d), a simulation was completed at

3640 rpm with an axial depth of 5.3 mm. The time history and Poincaré map for both τ

and 4τ sampling periods are displayed in Figure 4.8. The period-4 behavior is seen.
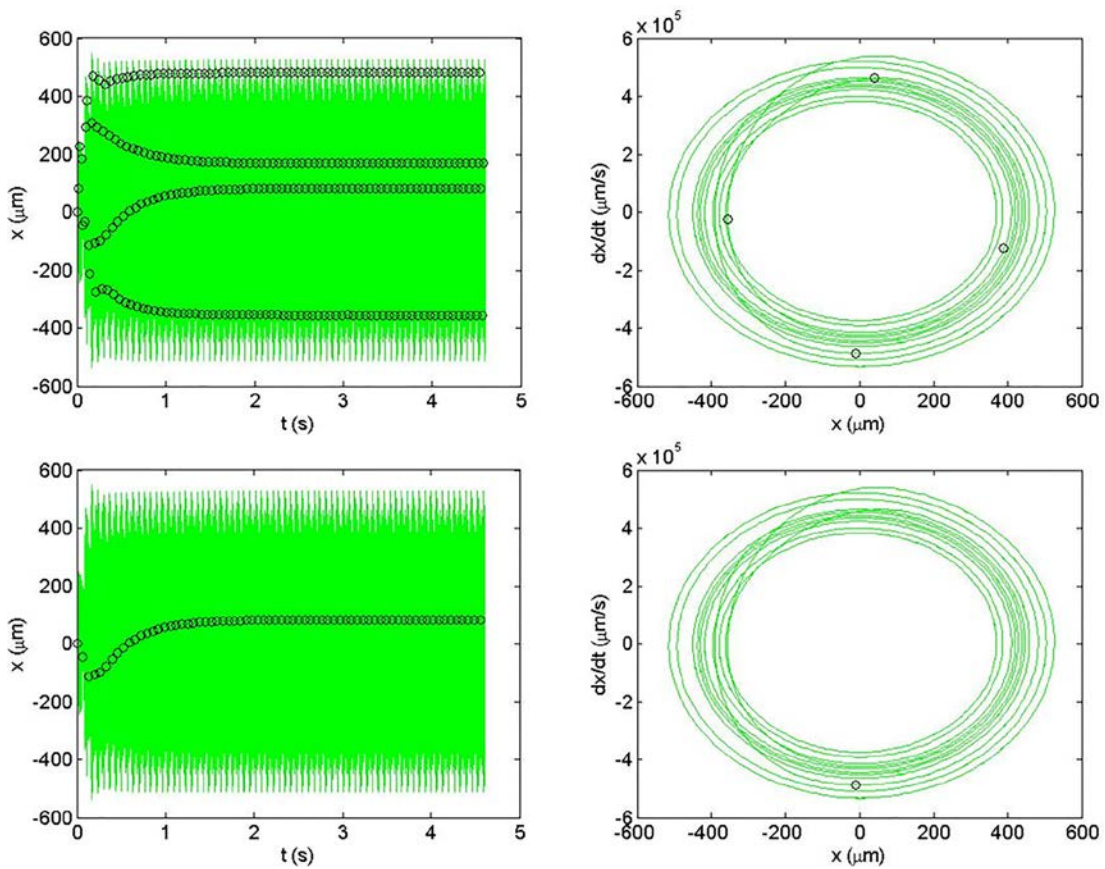
Figure 4.8: Simulation results for a spindle speed of 4070 rpm at an axial depth of 3.6 mm. The workpiece *x* and *y* displacements are shown. (Top row) Time history (left) and Poincaré map (right) for once-per-tooth sampling (τ sampling period). (Bottom row) Time history (left) and Poincaré map (right) for subharmonic sampling at 4τ.

Figures 4.7(b) and 4.7(d) show the residual content where the period-2 bifurcations were previously present prior to the 2τ sampling. To explore these remaining unstable zones, a bifurcation diagram was generated at an axial depth of 6.4 mm for spindle speeds from 3950 rpm to 4150 rpm. This spindle speed range transitions from the unstable zone, to the stable zone, through the residual unstable point, to the period-2 bifurcations, and finally back to the stable zone (to the right of the period-2 island). The diagram is shown in Figure 4.9, and the various behaviors are identified.
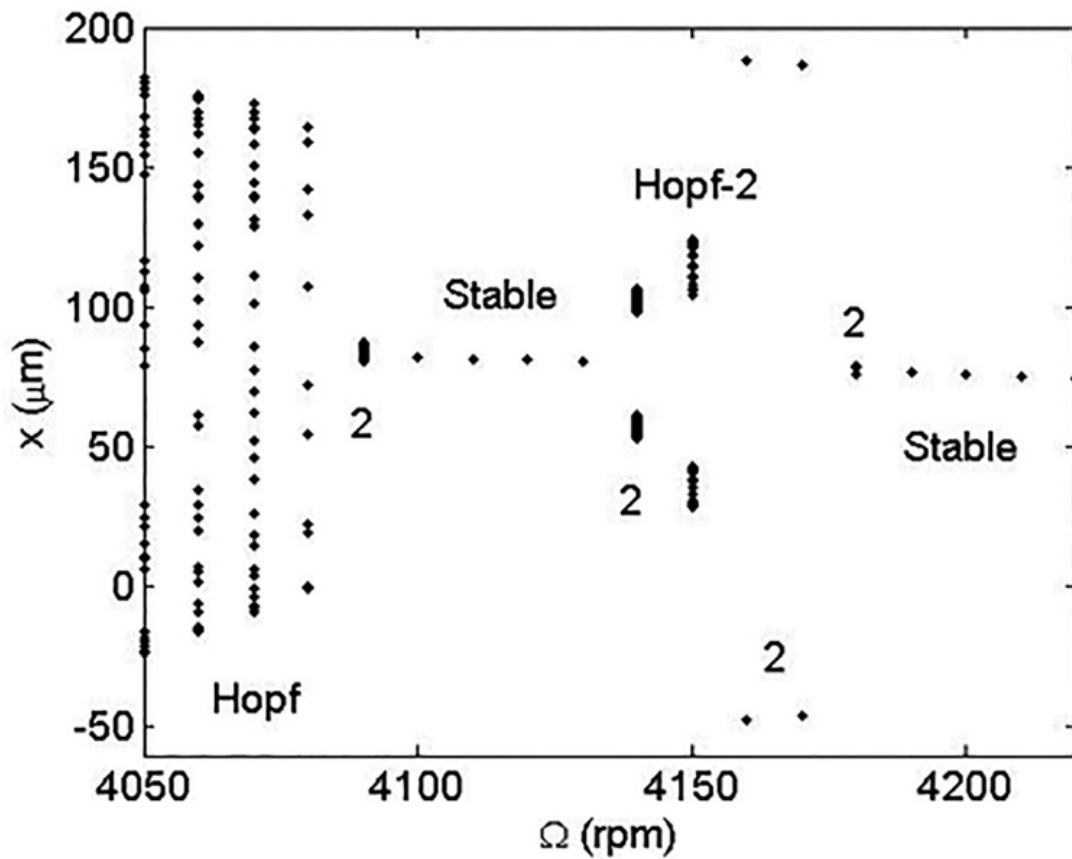
Figure 4.9: Bifurcation diagram for an axial depth of 6.4 mm. Hopf (Hopf), period-2 (2), stable (stable), and combination Hopf and period-2 (Hopf-2) behaviors are specified.

The combination secondary Hopf/period-2 behavior (labeled Hopf-2) is the reason for the

residual unstable zones in Figures 4.7(b) and 4.7(d). This quasi-periodic instability is

shown in Figure 4.10, which displays the time history and Poincaré map for a spindle

speed of 4150 rpm, where two separate ellipses are observed. The elliptical distribution

of once-per-tooth sampled points is characteristic of

secondary Hopf bifurcations; two ellipses indicate the simultaneous presence of period-2

behavior.
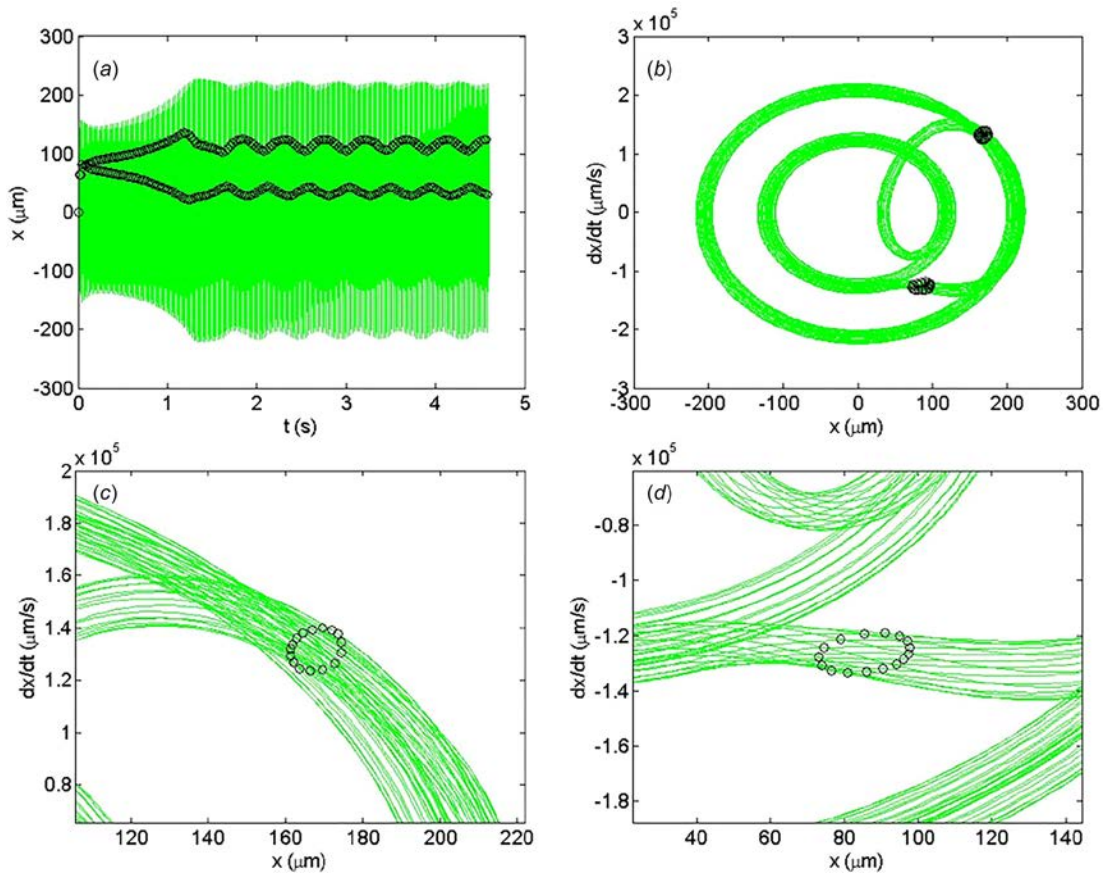
Figure 4.10: Simulation results for a spindle speed of 4150 rpm at an axial depth of 6.4 mm. The workpiece *x* and *y* displacements are shown. (Top row) Time history (left) and Poincaré map (right) for once-per-tooth sampling. (Bottom row) Higher magnification views of the two elliptical distributions of once-per-tooth sampled points.

The subharmonic sampling approach is now implemented to construct a stability map that individually identifies each bifurcation type. The metrics *M1 – M7*, which represent τ–7τ integer sampling periods, are used to isolate the stable zone as well as the different bifurcation types: period-2, -3, -4, -5, -6, -7, and secondary Hopf. The logic used to construct the stability map is as follows:

if $M1 \leq 1$ μm
        (stable, do nothing)

```
        elseif M2 ≤ 1 μm
                plot a circle (period-2)
        elseif M3 ≤ 1 μm
                plot a triangle (period-3)
        elseif M4 ≤ 1 μm and M2 > 1 μm
                plot a square (period-4, excludes period-2)
        elseif M5 ≤ 1 μm
                plot a + (period-5)
        elseif M6 ≤ 1 μm and M2 > 1 μm and M3 > 1 μm
                plot a diamond (period-6, excludes period-2 and period-3)
        elseif M7 ≤ 1 μm
                plot an × (period-7)
        else
                plot a dot (secondary Hopf or high order period-n)
        end
```

The result is displayed in Figure 4.11. The stable zone is the open white area, and the

various instabilities are indicated by the symbols. Note that the behavior shown in

Figures 4.9 and 4.10 is captured in the map at an axial depth of 6.4 mm. The single

unstable point within the period-2 zone is seen. The box in the figure indicates the spindle

speed range and axial depth (6.4 mm) for the bifurcation diagram in Figure 4.9.
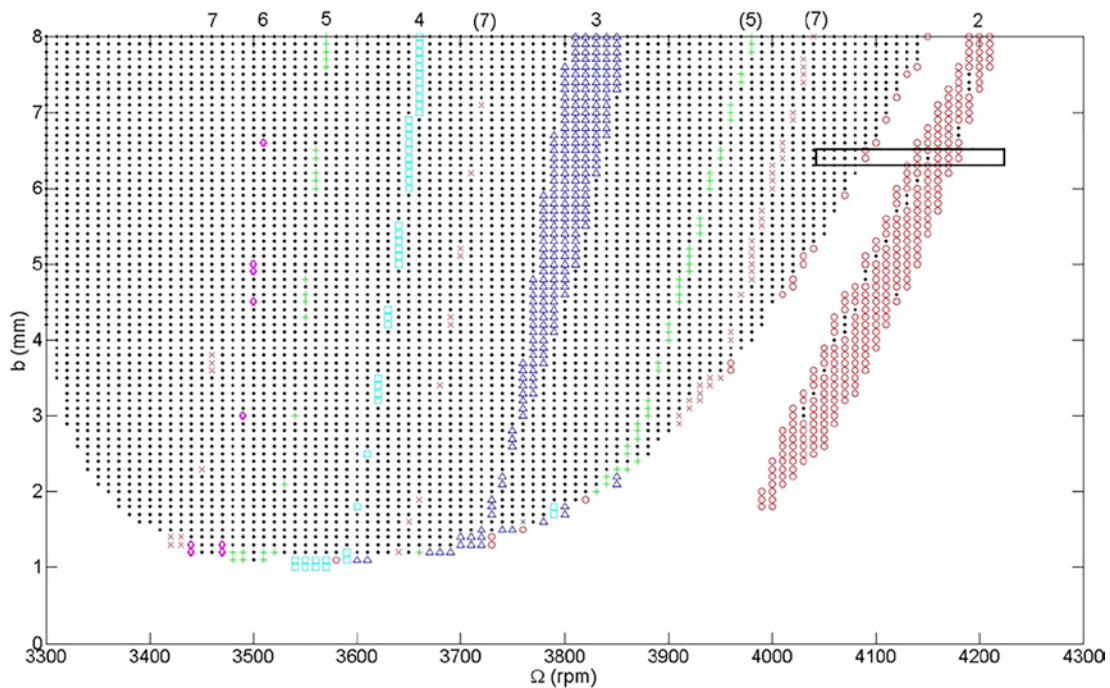
Figure 4.11: New stability map. Period-2 (circle), period-3 (triangle), period-4 (square), period-5 (+), period-6 (diamond), period-7 (×), and secondary Hopf (dot) bifurcations are individually identified. The box indicates the spindle speed range and axial depth (6.4 mm) for the bifurcation diagram in Figure 4.9.

By following the bifurcations in the map from period-2 (circle), to -3 (triangle), to -4 (square), to -5 (+), to -6 (diamond), and to -7 (×), it appears that a pattern is emerging. Within the single stability lobe, the increasing order shifts the period-n zones to progressively lower spindle speeds. Also, the size of the zones diminishes with increasing order. The period numbers for the various zones are provided above the stability map in Figure 4.11. For period-5 and -7 bifurcations, there are additional zones that appear to "fold over" to higher speeds; these are denoted by parenthetical order numbers in Figure 4.11. There is one of these fold over zones for period-5 and two for period-7.

CHAPTER 5: EXPERIMENTAL SETUP

5.1   Cutting Force Coefficients

The cutting force coefficients were determined using a mechanistic linear

regression method described in [57]. This model assumes that the average cutting force in

the *x* and *y* direction increases linearly with the feed per tooth value. A series of cutting

tests are performed over a range of specified feed per tooth values. The average *x* force,

$\overline{F_x}$, and average y force, $\overline{F_y}$ are plotted against the feed per tooth values. The cutting force

coefficients are then extracted via linear regression fitting where the cutting coefficients,

k_{tc} and k_{nc}, can be determined from the slopes of the linear fit, and the edge coefficients,

k_{te} and k_{ne}, can be determined from the y intercepts of the linear fit.

5.2   Flexures for Milling Experiments

Time and frequency domain milling process models maybe implemented to enable

pre-process parameter selection for increased material removal rate, improved surface

finish, and enhanced accuracy [47-49]. To complete these simulations and validate the

results, the system dynamics must be known. Typically, the cutting tool flexibility

dominates the system dynamics, although the workpiece can introduce significant

flexibility in some cases as well.

To realize a validation platform with simple (often single degree of freedom)

dynamics, flexures may be used to support the workpiece (Figure 5.1). In this

configuration, the flexure stiffness maybe selected to be much lower than the tool

stiffness so that the tool dynamics can be effectively ignored.

The basis for the milling platform designed and tested in this study is a parallelogram, leaf-type flexure. By selecting the leaf geometry and workpiece/platform mass, the stiffness and natural frequency can be defined to meet the experimental requirements. The design approach is described in [50] and, for brevity, is not discussed here. As noted, however, the damping for this geometry, particularly monolithic designs, is low.
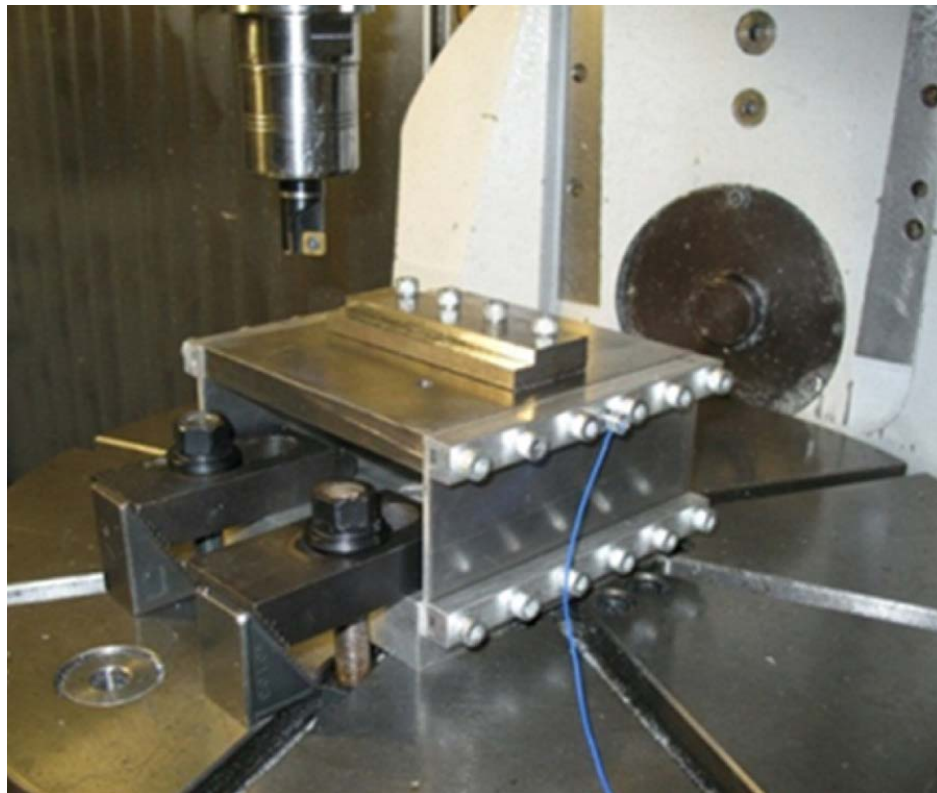
Figure 5.1: Example parallelogram, leaf-type flexure used for milling experiments. A workpiece is mounted to the top of the flexure, an accelerometer is used to measure the vibration during cutting, and an inserted cutting tool is pictured.

5.3   Variable Damping Flexure

In order to study the effect of damping on period-n bifurcations, a variable damping flexure is used. The variable damping flexure allows the damping ratio of a flexure to be adjusted through the use of an eddy current damper. To introduce higher damping using a first principles model, the addition of an eddy current damper to the flexure setup is investigated here. The viscous (velocity-dependent) damping force for an eddy current damper can be described analytically. Figure 5.2 displays the motion of a conductor relative to a magnet (or magnet pair) with the motion perpendicular to the magnet pole direction. The eddy current density, $\vec{J}$, depends on the conductivity, σ, and the cross product of the velocity, $\vec{v}$, and magnetic field, $\vec{B}$ (see Eq. (21)). The eddy current force is then calculated as the volume integral of the product of the eddy current density and the magnetic field (see Eq. 22). Mathematically, the two cross products yield a damping force which acts in the direction opposite to the velocity.

$$\vec{J} = \sigma(\vec{v} \times \vec{B}) \tag{21}$$

$$\vec{F} = \int_V \left(\vec{J} \times \vec{B}\right) dV \tag{22}$$

The damping force magnitude, $\vec{F}$, is described by Eq.(23) , where δ is the conductor thickness, $\vec{B}$ is the magnetic field strength, S is the magnet surface area, α_1 incorporates surface charge effects, α_2 describes end effects from the finite dimension conductor, and v is the velocity magnitude [51]. As shown, Eq. (23) can be rewritten as the product of a viscous damping coefficient, c, and the velocity magnitude. This viscous

damping coefficient enables model-based damping prediction and selection for milling

simulation and experiments.
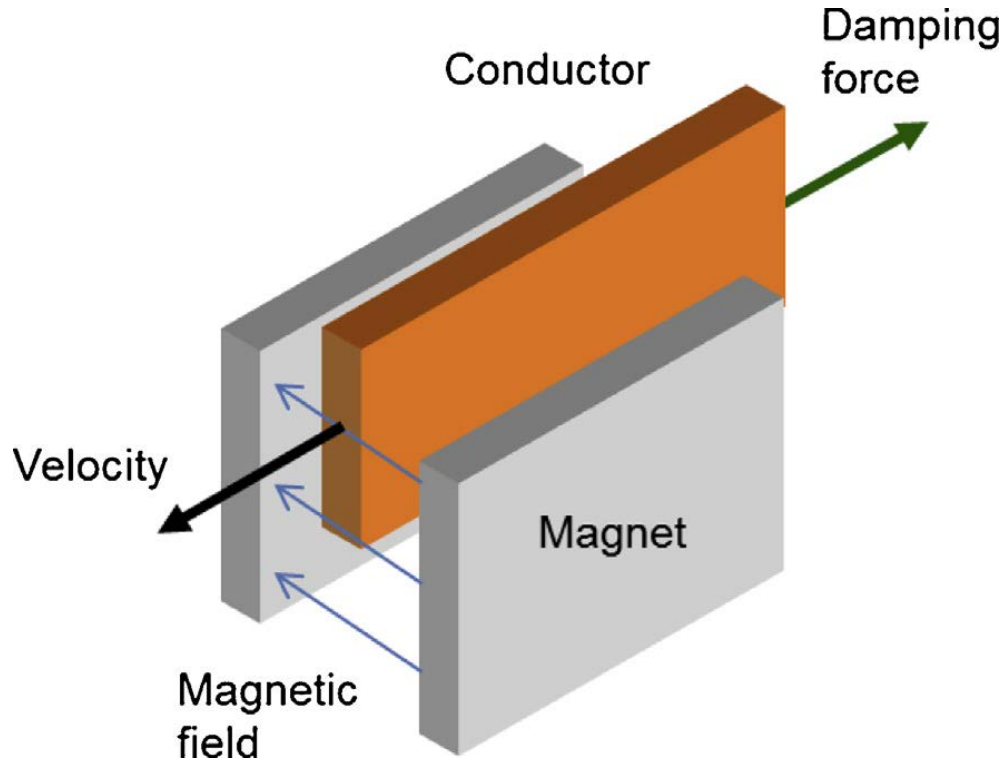
Figure 5.2: Schematic of an eddy current damper.

$$F = \big(\sigma\delta B^2 S(\alpha_1 + \alpha_2)\big)v = cv \qquad (23)$$

The surface charge effects term, α_1, is calculated using Eq. (24),where $2a$ is the

height of the magnet area and $2b$ is the width. For the setup described here, $a = 25.4$ mm

and $b = 50.8$ mm so that $\alpha_1 = 0.352$.

$$\alpha_1 = 1 - \frac{1}{2\pi}\left[4\,tan^{-1}\left(\frac{b}{a}\right) + \left(\frac{b}{a}\right)\ln\left(1 + \frac{a^2}{b^2}\right) - \frac{a}{b}\ln\left(1 + \frac{b^2}{a^2}\right)\right] \qquad (24)$$

The end effects term for the conductor, α_2, is determined using Eq. (25), where I_1

and I_2 are defined by Eqs. (26) and (27). In these equations, $2H$ is the height of the

conductor, $h = ba^{-1}$, and $w = Ha^{-1}$. For the eddy current damper designed and

constructed in this study, $H = 38.1$ mm and $\alpha_2 = $ -0.177.

$$\alpha_2 = -\frac{1}{2\pi}(I_1 + I_2) \tag{25}$$

$$I_1 = 4w \tan^{-1}\left(\frac{h}{w}\right) - 4(1-w)\tan^{-1}\left(\frac{h}{1-w}\right) + \frac{w^2}{h}\ln(w^2) -$$
$$\frac{1}{h}(w^2 - h^2)\ln(w^2 + h^2) - \frac{1}{h}(1-w)^2 \ln(1-w)^2 +$$
$$\frac{1}{h}((1-w)^2 - h^2)\ln((1-w)^2 + h^2) \tag{26}$$

$$I_2 = 4w \tan^{-1}\left(\frac{h}{w}\right) - 4(1+w)\tan^{-1}\left(\frac{h}{1+w}\right) + \frac{w^2}{h}\ln(w^2) -$$
$$\frac{1}{h}(w^2 - h^2)\ln(w^2 + h^2) - \frac{1}{h}(1+w)^2 \ln(1+w)^2 +$$
$$\frac{1}{h}((1+w)^2 - h^2)\ln((1+w)^2 + h^2) \tag{27}$$

The eddy current damper concept displayed in Figure 5.2 was embedded inside an

aluminum flexure as shown in Figure 5.3. The conductor was attached to the aluminum

flexure platform and two permanent magnet sets were attached to the aluminum flexure

base, one on each side of the conductor. The arrangement of the eight 25.4 mm square

neodymium magnets (K&J Magnetics BXOXO8DCB) is shown in Figure 5.4; aluminum

socket head cap screws were used to avoid disrupting the magnetic field.

The solid model displayed in Figure 5.3 was constructed and tested. As shown in

Eq. (23), the viscous damping coefficient can be predicted using σ, δ, B, S, and the

surface charge/end effect terms, which serve to reduce the damping value (see Table

5.1).The conductor was a 19.1 mm thick copper plate that extended outside the magnet

surface area. The magnetic field strength was measured at 64 locations over the surface

of the eight permanent magnets using a gaussmeter (Integrity Design & Research Corp.

IDR-329-T). Measurements were performed at a distance of 0.8 mm from the surface;

this was the approximate air gap between the magnets and conductor after assembly. The

average value for all 64 measurements at the 0.8 mm distance is listed in Table 5.1.
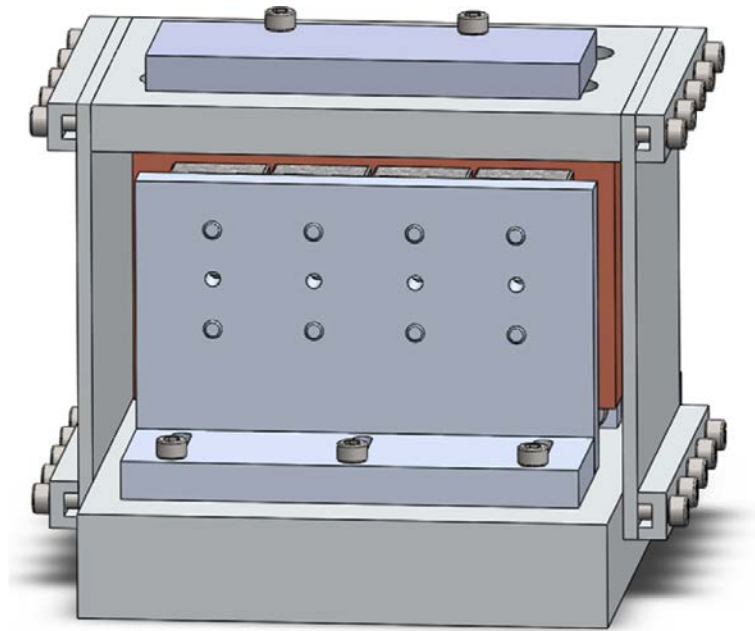
Figure 5.3: Flexure with embedded eddy current damper
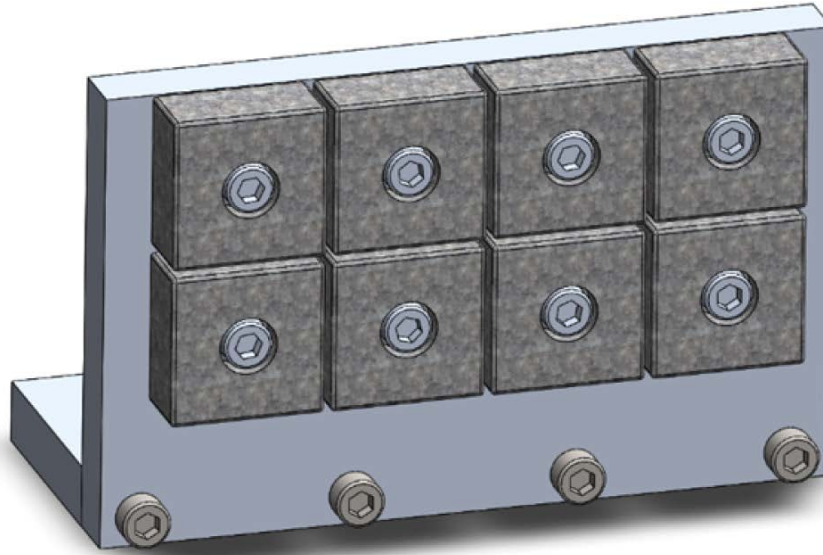
Figure 5.4: Permanent magnet mount. The magnets face the conductor with one mount on each side.

Table 5.1: Eddy current damper design parameters

Parameter	σ	δ	B	S	α_1	α_2
Value	5.96×10^7	19.1	4580	4.60×10^{-3}	0.352	-0.177
units	A/Vm	mm	Gauss	m^2	-	-

For the values listed in Table 5.1, the predicted eddy current damper c value is 192 N s/m. The corresponding dimensionless damping ratio, ζ, is calculated using Eq. (28), where k is the flexure stiffness provided in Eq. (29) and m is the equivalent flexure mass given by Eq. (30) [50]. In Eq. (29), E is the aluminum leaf's elastic modulus (69 GPa), w is the width (101.6 mm), t is the thickness (3.8 mm), and l is the length (88.9 mm). In Eq. (30), m_p is the combined mass of the platform, conductor, top leaf clamps, and fasteners (2.098 kg) and m_l is the leaf mass (0.12 kg). The predicted damping ratio is 0.063 (6.3%). Using the flexure stiffness (1.093×10^6 N/m) and mass values (2.277 kg), the predicted undamped natural frequency is $f_n = 110$ Hz.

$$\zeta = \frac{c}{2\sqrt{km}} \tag{28}$$

$$k = 2Ew\left(\frac{t}{l}\right)^3 \tag{29}$$

$$m = m_p + \left(\frac{26}{35}\right)m_l \tag{30}$$

Modal tests were performed to identify the actual damping ratio for the flexure. The setup is shown in Figure 5.5. An instrumented hammer (PCB 086C04) was used to excite the structure and the response was measured using a low-mass accelerometer (PCB 352C23). The modal parameters extracted from the single degree of freedom frequency response function were: $f_n = 110$ Hz, $k = 1.06 \times 10^6$ N/m, and $\zeta = 0.046$ (4.6%). The disagreement in the damping ratio is attributed to approximations in the surface charge and end effects terms, α_1 and α_2. The eight individual magnets were assumed to comprise a single magnetic surface with the area reduced by the cap screw holes. Also, the actual magnetic field strength is strongly sensitive to the air gap, which was set with a plastic shim during damper assembly, and the viscous damping coefficient varies with the square of this value.

Modal tests were also performed after removing the magnets so that the eddy current damping effect was eliminated, but the structure was not otherwise modified. The modal parameters extracted from the single degree of freedom frequency response function were: $f_n = 108$ Hz, $k = 9.03 \times 10^5$ N/m, and $\zeta = 0.014$. The addition of the eddy current damper provided a 229% increase in damping.

The damping ratio of the flexure can be varied by changing the air gap between the permanent magnets and the conductor. The modal parameters of this flexure were

always measured through impact testing before any experiment was conducted or after

the air gap was adjusted on the flexure. This variable damping flexure was necessary in

studying the effect of damping ratio on period-n bifurcations.
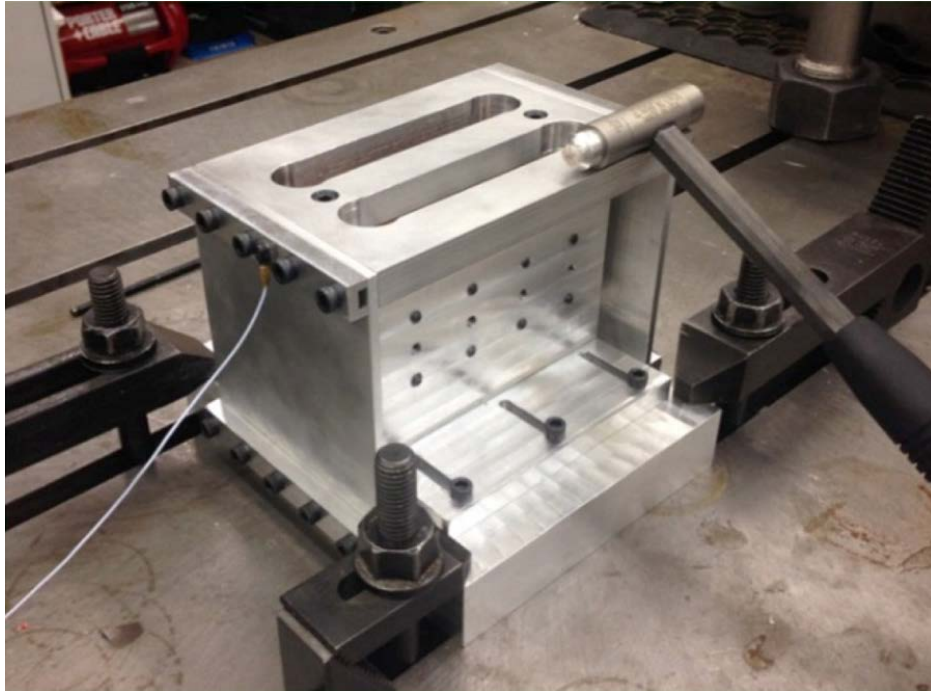
Figure 5.5: Impact testing setup for experimental identification of damped flexure
dynamics.

5.4   Once-per-tooth Sampling of Flexure Dynamic Response

A single degree-of-freedom (SDOF) flexure was used to define the system

dynamics, where the SDOF flexure was much less stiff than the cutting tool. The flexure

setup also simplifies the measurement instrumentation. The flexure motions are measured

using a capacitance probe (CP), laser vibrometer (LV), and low mass accelerometer. In

order to enable once-per-tooth sampling of the vibration signals, a laser tachometer (LT)

is used. A small section of reflective tape is attached to the tool holder and the

corresponding (digital) tachometer signal was used to perform the periodic sampling. The

laser tachometer ensures synchronous sampling of the vibrations signals (ie, laser

vibrometer, capacitance probe, etc.) with the forcing function (ie, the cutting tool). Figure

5.6 shows the experimental setup used to measure and once-per-tooth sample the

response of the SDOF flexure.

Figure 5.6: Milling experimental setup with laser vibrometer (LV), low mass piezo-
accelerometer (PA), laser tachometer (LT), and capacitance probe (CP).

CHAPTER 6: BIFURCATIONS IN MILLING

6.1   Experimental Bifurcation Diagram

A bifurcation diagram for a spindle speed of 3800 rpm, radial depth of 5mm, and

up milling feed of 0.15 mm/tooth was predicted by simulation and then cuts were

performed from 1mm to 7mm axial depths in 0.5mm steps. The capacitance probe (CP)

displacement signal was sampled using the laser tachometer (LT) to construct an

experimental bifurcation diagram; Figure 6.1 provides the comparison between prediction

and experiment. For this axial depth of cut range, period-3 bifurcations were observed.

The flexure dynamics were: 163 Hz natural frequency, 0.0108 viscous damping ratio, and 5.6×10^6 N/m stiffness. For this bifurcation diagram, the cutting tool was a 19.1 mm diameter, single flute carbide square endmill (30 degree helix angle). The cutting tool dynamic response was: 1055 Hz natural frequency, 0.045 viscous damping ratio, and 4.2×10^7 N/m stiffness. The 6061-T6 aluminum alloy cutting force coefficients were: $k_{tc} = 792\times10^6$ N/m^2, $k_{nc} = 352\times10^6$ N/m^2, $k_{te} = 26\times10^3$ N/m, and $k_{ne} = 28\times10^3$ N/m. The experimental setup is shown in Figure 5.6.
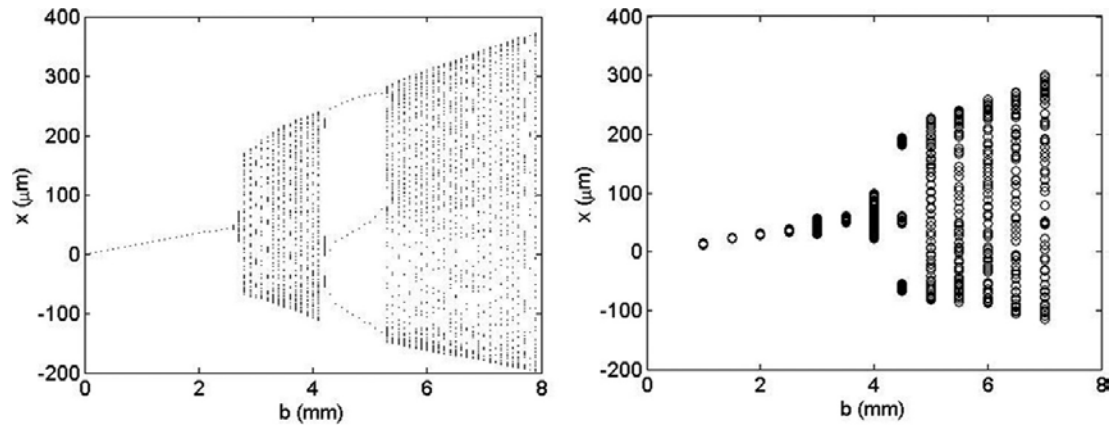
Figure 6.1: Bifurcation diagram for 3800 rpm and 5 mm (26%) radial depth of cut. Simulated diagram (left) and experimental diagram (right).

A simulated stability map for the same axial depth of cut range as Figure 6.1, but spindle speeds from 3300 rpm to 4300 rpm, is displayed in Figure 6.2 (the same dynamics were again used). The diagram was constructed by completing time domain simulations over a grid with a spindle speed resolution of 10 rpm and an axial depth resolution of 0.1 mm. The initial transients were removed and the M value for each simulation was calculated (see Eq. (18)). An arbitrarily small value of 1 μm was selected

to differentiate between stable and unstable parameter combinations; this contour is

shown in Figure 6.2 and identifies the stability limit. The transition from stable to

unstable behavior at 3800 rpm observed in Figure 6.1 is replicated. The transition from

secondary Hopf to period-3 to secondary Hopf seen in the bifurcation diagram is not

detailed in the stability map, however.
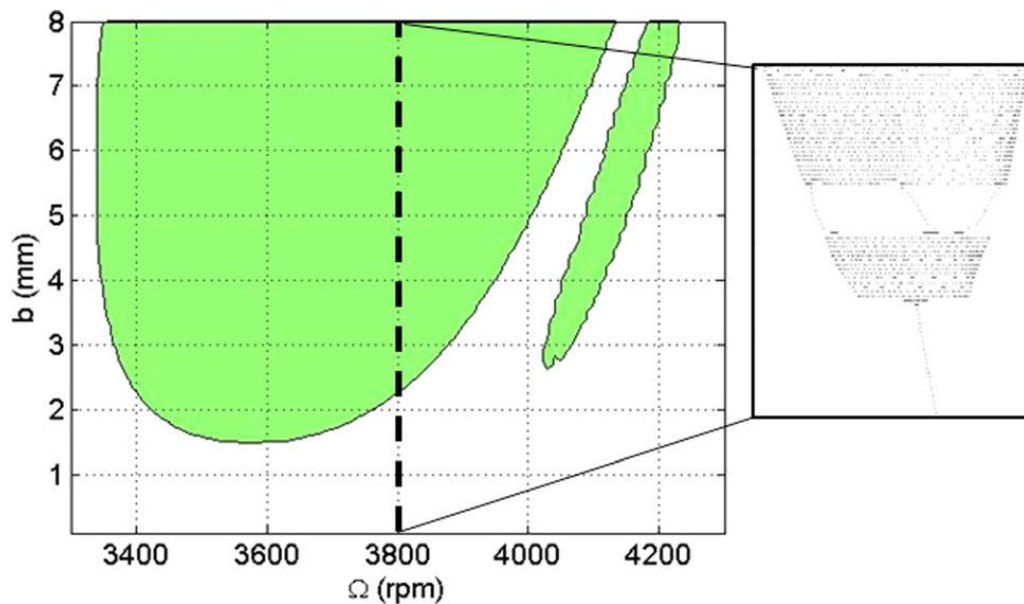
Figure 6.2: Simulated stability map for period-3 experimental setup. The transition from stable to unstable behavior occurs at approximately 2.6 mm for a spindle speed of 3800 rpm. The inset shows the bifurcation diagram progression at 3800 rpm from stable to quasi-periodic instability to period-3 and back to quasi-periodic behavior.

6.2   Existence of High Order Period-n Bifurcations

In this section, comparison is made between time domain simulation predictions

and milling experiments for multiple setups; the presence of period-n bifurcations is

presented. A single degree-of-freedom (SDOF) flexure was used to define the system

dynamics, where the SDOF flexure was much less stiff than the cutting tool [52]. The

cutting tool described in Section 6.1 was used. The aluminum alloy cutting force coefficients were the same as the coefficients described in Section 6.1. The flexure setup also simplified the measurement instrumentation. The flexure motions were measured using a capacitance probe (CP), laser vibrometer (LV), and low mass accelerometer. In order to enable once-per-tooth sampling of the vibration signals, a laser tachometer (LT) was used. A small section of reflective tape was attached to the tool holder and the corresponding (digital) tachometer signal was used to perform the periodic sampling.

Results for period-2, 3, 6, 7, and 8, and 15 bifurcations are displayed in Figures 6.3-6.9. In each figure, the left plot shows the simulated behavior and the right plot shows the experimental result, where the cut entry and exit transients were removed before plotting. Good agreement is observed in each case. The cutting conditions and flexure dynamics for each experiment can be found in Table 6.1.

Table 6.1: Cutting conditions and flexure dynamics for experiments

| Period-n (figure number) | Cutting conditions | | | Flexure dynamics | | |
	Spindle speed (rpm)	Axial depth (mm)	Radial depth (mm)	Stiffness (N/m)	Natural frequency (Hz)	Viscous damping ratio (%)
2 (6.3)	3486	2.0	1.0	9.0×10^5	83.0	2.00
3 (6.4)	3800	4.5	5.0	5.6×10^6	163.0	1.08
6 (6.5)	3200	18.0	1.0	5.6×10^6	202.6	0.28
6 (6.6)	3250	15.5	1.0	5.6×10^6	205.8	0.28
7 (6.7)	3200	14.5	1.0	5.6×10^6	204.1	0.28
8 (6.8)	3310	15.0	2.0	2.1×10^6	130.1	1.47
15 (6.9)	3200	14.0	1.0	5.6×10^6	204.8	0.28
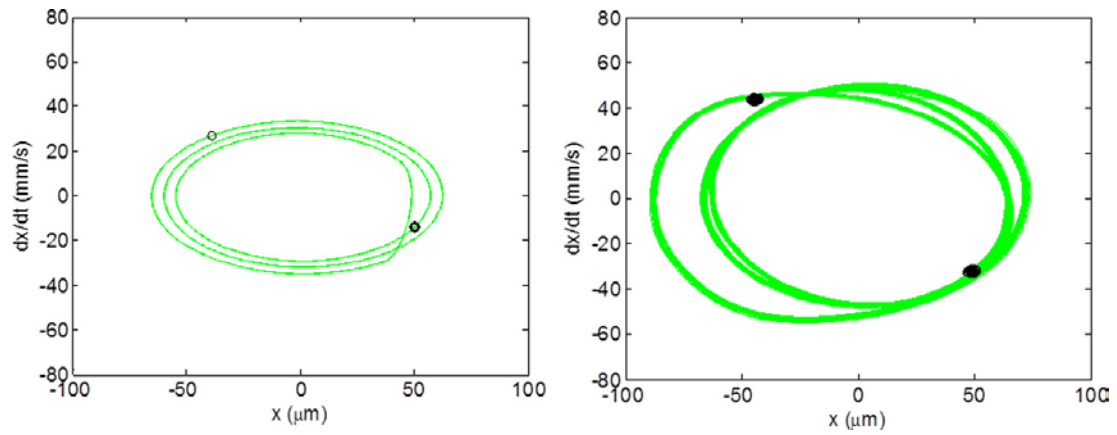
Figure 6.3: Poincaré map for period-2 bifurcation. (Left) simulation and (right) experiment. The phase space trajectory is represented by the solid line and the once-per-tooth sampled points are displayed as circles.
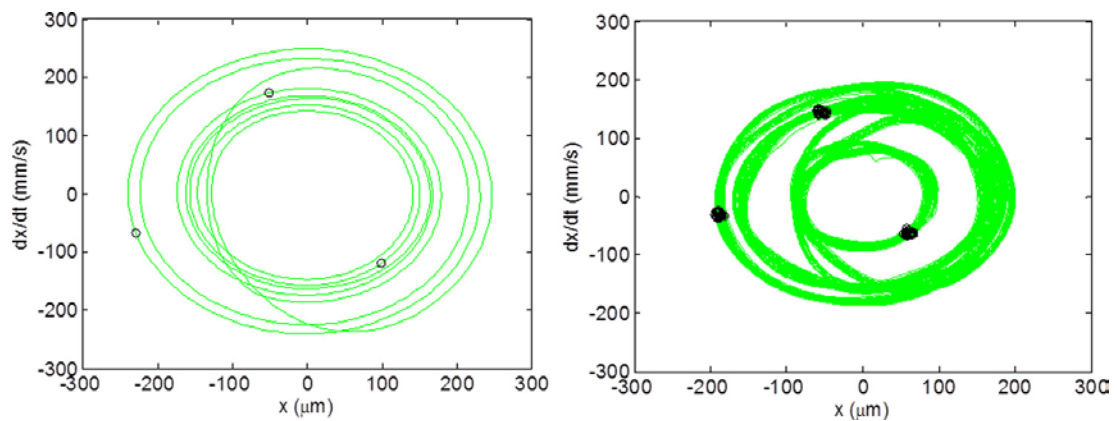
Figure 6.4: Poincaré map for period-3 bifurcation. (Left) simulation and (right) experiment
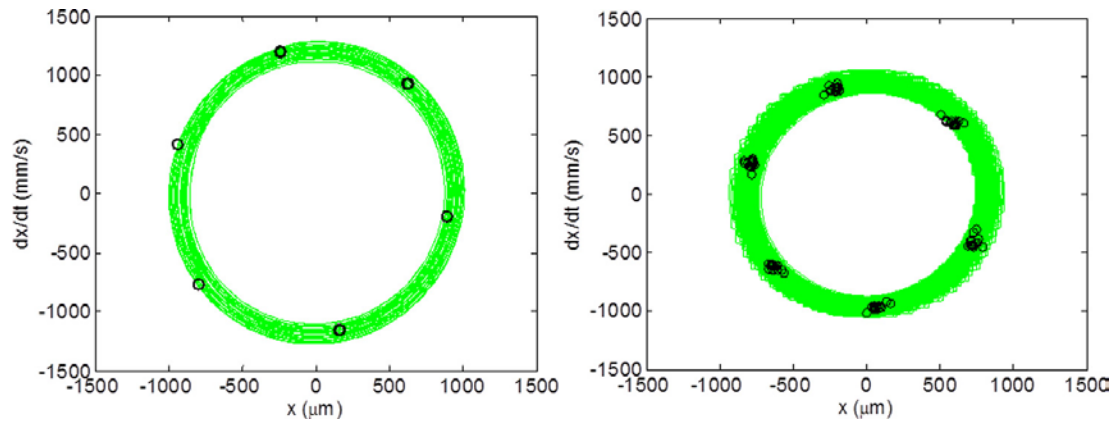
Figure 6.5: Poincaré map for period-6 bifurcation. (Left) simulation and (right) experiment
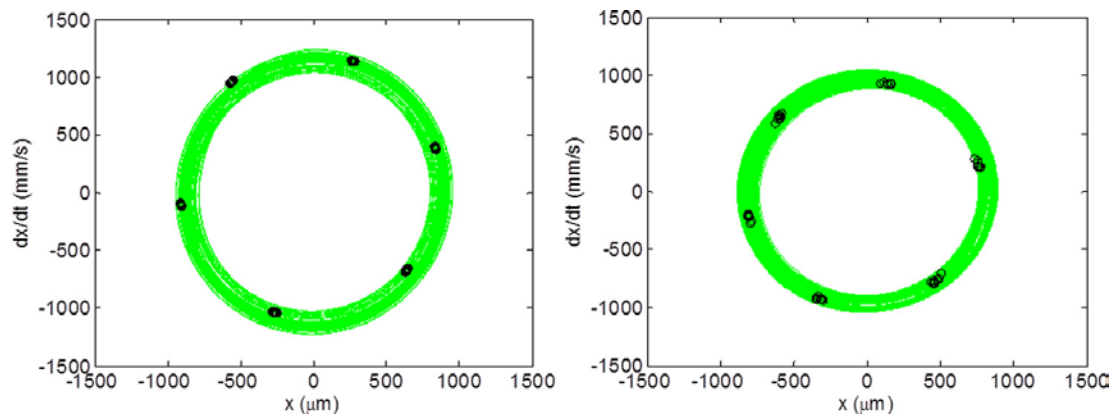
Figure 6.6: Poincaré map for period-6 bifurcation. (Left) simulation and (right) experiment
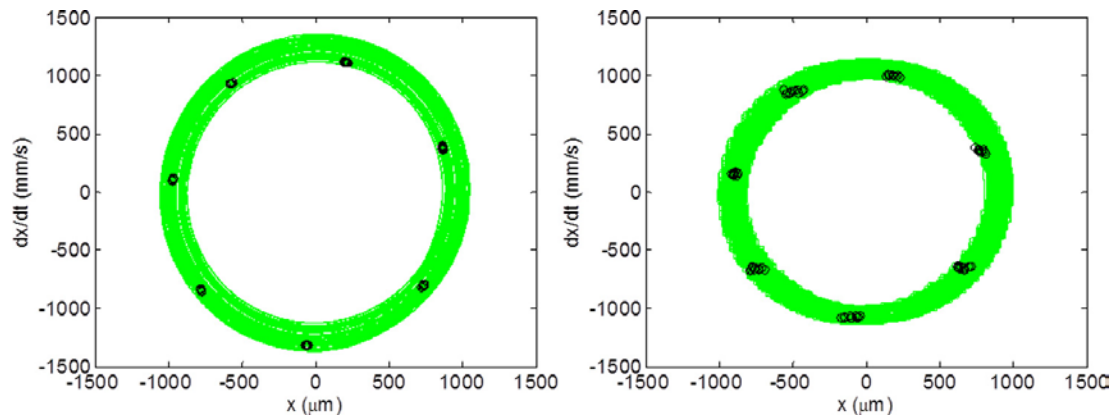
Figure 6.7: Poincaré map for period-7 bifurcation. (Left) simulation and (right) experiment
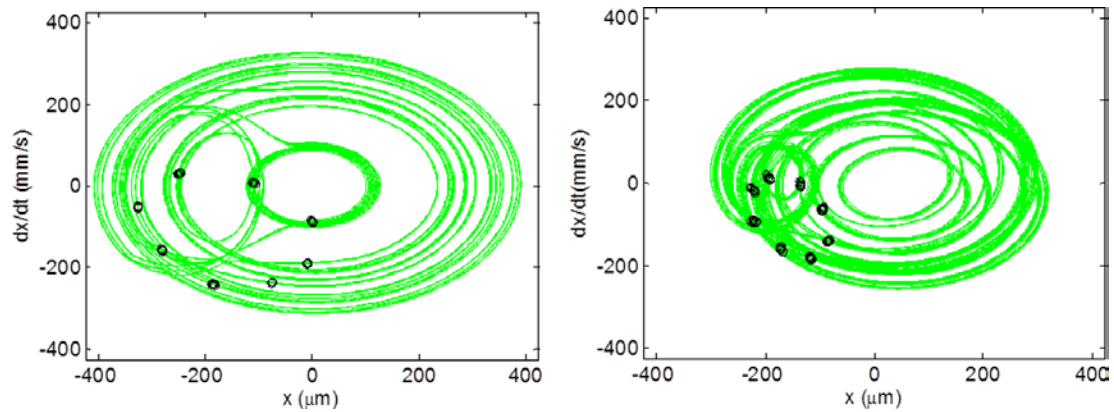
Figure 6.8: Poincaré map for period-8 bifurcation. (Left) simulation and (right) experiment
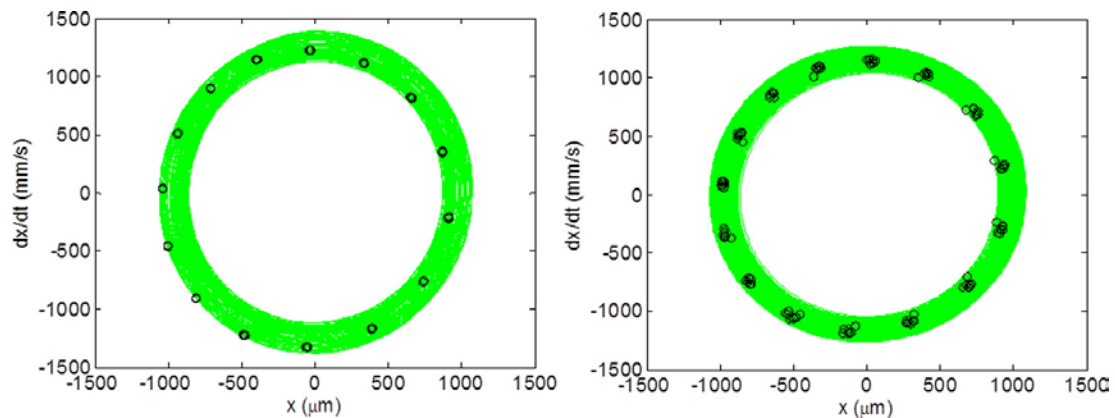
Figure 6.9: Poincaré map for period-15 bifurcation. (Left) simulation and (right) experiment

6.3   Sensitivity of Period-n Bifurcation to System Natural Frequency

Experiments were completed to demonstrate the sensitivity of the period-n

bifurcation behavior to changes in natural frequency. During the up milling cutting trials,

material was removed from the workpiece. This lowered the workpiece mass and,

subsequently, increased the flexure's natural frequency. Since the mass of the

chips is much smaller than the workpiece, this material removal resulted in small changes

in natural frequency. The variation in system dynamics for the results presented in

Figures 6.10-6.13 is provided in Table 6.2 and the cutting conditions are provided in

Table 6.3. The higher period-n bifurcations exhibited sufficient sensitivity to flexure

natural frequency that, within a single cut, both period-n bifurcation and quasi-periodic

behavior (secondary Hopf bifurcation) were observed. For these tests, the cutting tool

described in Section 6.1 was used while feeding at 0.15 mm/tooth. The aluminum alloy

cutting force coefficients were the same as the coefficients described in Section 6.1.

Figures 6.10-6.13 display the flexure's feed direction velocity (dx/dt) in the time

domain. The continuous signal is displayed as a solid line, while the circles are the once-

per-tooth sampled points. In each figure, the left plot shows the simulated behavior and

the right plot shows the experimental behavior. Good agreement is observed. The time

domain simulation was modified to account for the changing natural frequency due to

mass loss. After each time-step, the change in mass was calculated based on the volume

of the removed chip and the density of the workpiece material (2700 kg/m^3). This change

in mass was then used to update the flexure's natural frequency for the next time-step.
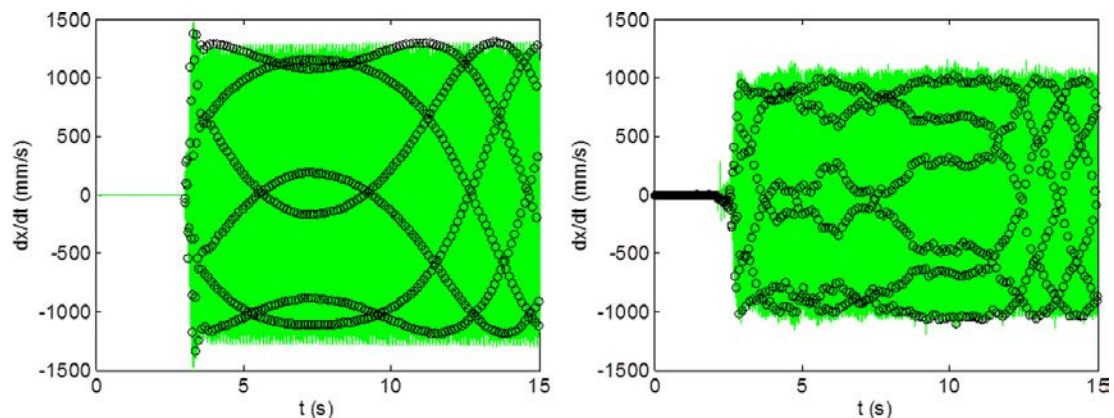
Figure 6.10: Variation in bifurcation behavior with changes in natural frequency. Period-6 bifurcation is observed. (Left) simulation and (right) experiment. Period-6 behavior is observed from 4 to 11 s, followed by quasi-periodic behavior until the end of the cut.
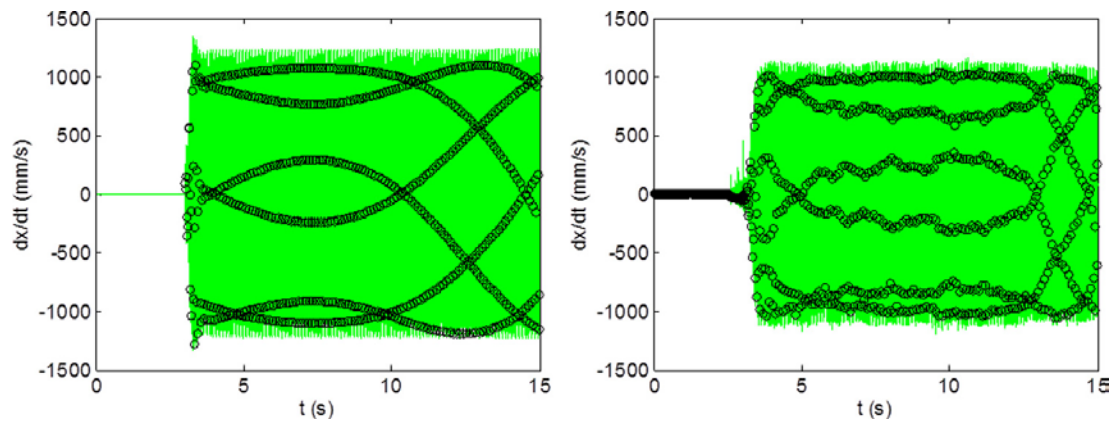
Figure 6.11: Variation in bifurcation behavior with changes in natural frequency. Period-6 bifurcation is observed. (Left) simulation and (right) experiment. Period-6 behavior is observed from 4 to 13 s, followed by quasi-periodic behavior until the end of the cut.
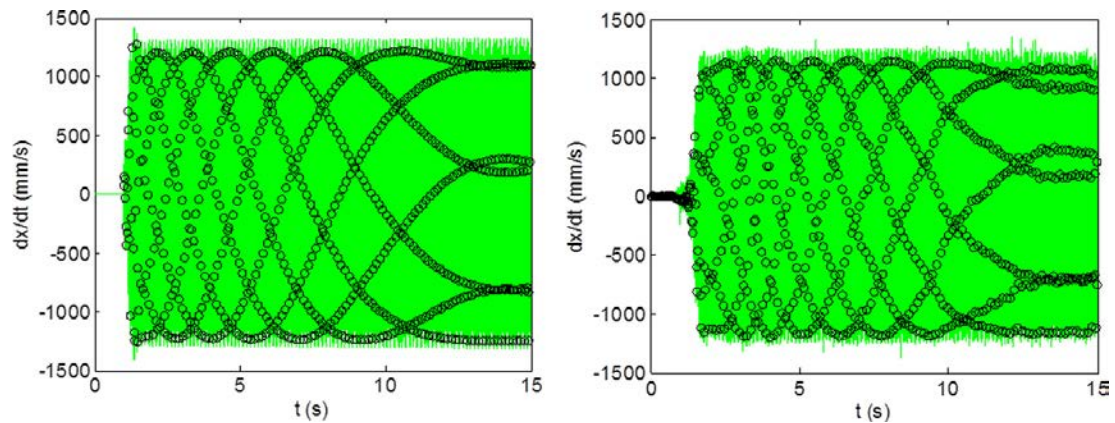
Figure 6.12: Variation in bifurcation behavior with changes in natural frequency. Period-7 bifurcation is observed. (Left) simulation and (right) experiment. Quasi-periodic behavior is observed from the beginning of the cut until 11s and then period-7 behavior from 11 to 15 s.
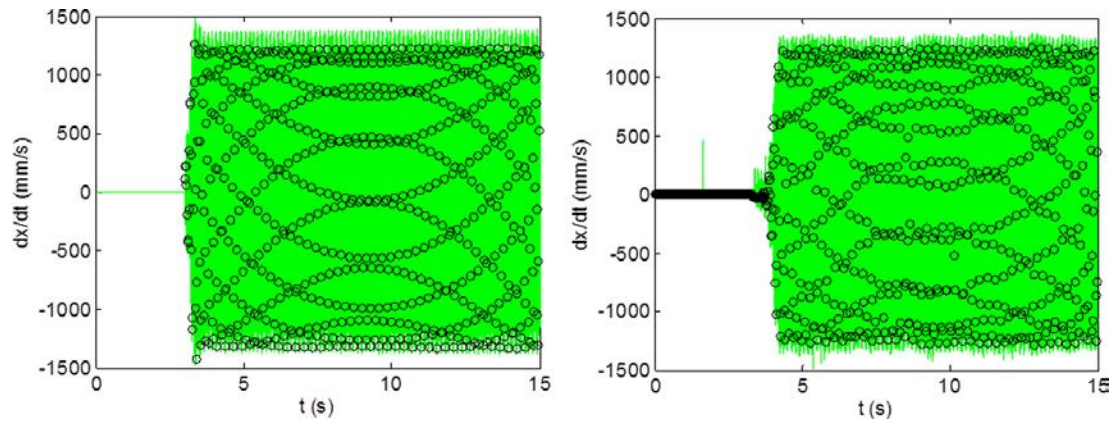
Figure 6.13: Variation in bifurcation behavior with changes in natural frequency. Period-15 bifurcation is observed. (Left) simulation and (right) experiment. Quasi-periodic behavior is observed from the beginning of the cut until 8 s, period-15 behavior from 8 to 13 s, and then quasi-periodic behavior until the end of the cut.

Table 6.2: Changes in natural frequency due to mass removal

| Period-n (figure number) | Flexure dynamics | | | |
	Natural Frequency, beginning of cut (Hz)	Natural frequency, end of cut (Hz)	Change in natural frequency (Hz)	Change in mass (g)
6 (6.10)	202.4	202.7	0.3	4.8
6 (6.11)	205.7	205.9	0.2	4.1
7 (6.12)	204.1	204.3	0.2	3.9
15 (6.13)	204.7	204.9	0.2	3.7

Table 6.3: Cutting conditions for Table 6.2

| Period-n (figure number) | Cutting conditions | | |
	Spindle Speed (rpm)	Axial depth (mm)	Radial depth (mm)
6 (6.10)	3200	18.0	1.0
6 (6.11)	3250	15.5	1.0
7 (6.12)	3200	14.5	1.0
15 (6.13)	3200	14.0	1.0

6.4   Sensitivity of Period-2 Bifurcations to Damping Ratio

To explore the sensitivity of period-n behavior to damping, machining trials were

conducted over a range of axial depths of cut (1 mm to 10 mm) with four different

flexure damping values. In all cases, the spindle speed was 3310 rpm, the radial depth of

cut was 2 mm, and the feed per tooth was 0.1 mm/tooth. For these tests, the cutting tool

described in Section 6.1 was used. The aluminum alloy cutting force coefficients were

the same as the coefficients described in Section 6.1. Table 6.4 details the tunable flexure

dynamics for the four damping values. The experimental setup is shown in Figure 6.18.

Table 6.4: Flexure dynamics for damping sensitivity experiments

Period-n (figure number)	Stiffness (N/m)	Natural frequency (Hz)	Viscous damping ratio (%)
2 (6.14)	2.1×10^6	130.0	1.47
2 (6.15)	2.1×10^6	130.0	1.91
2 (6.16)	2.1×10^6	130.0	2.34
- (6.17)	2.1×10^6	130.0	3.55

Simulated and experimental bifurcation diagrams are presented in Figures 6.14-

6.17 for the dynamics defined in Table 6.4. It is observed that as the damping increases,

the region of period-2 behavior diminishes in size and, in Figure 6.17 with a damping

ratio of 3.55%, it disappears all together. The stable behavior persists up to an axial depth

of approximately 4 mm for Figures 6.14-6.16. The period-2 behavior is then seen for

decreasing ranges of axial depth as the damping increases. It continues to approximately

8.2 mm for 1.47%, to approximately 7.6 mm for 1.91%, and to approximately 6.8 mm for

2.34%. In all cases, the period-2 behavior is followed by a second stable zone at higher

axial depths.
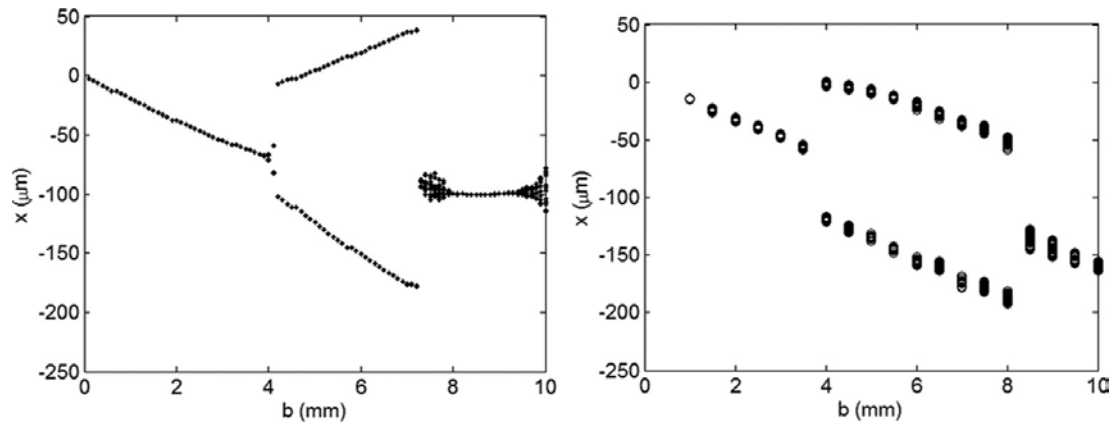
Figure 6.14: Bifurcation diagram for 1.47% damping (3310 rpm). (Left) simulation and (right) experiment. Stable behavior is observed up to approximately 4 mm, period-2 behavior then occurs up to approximately 8 mm, then stable behavior is again seen.
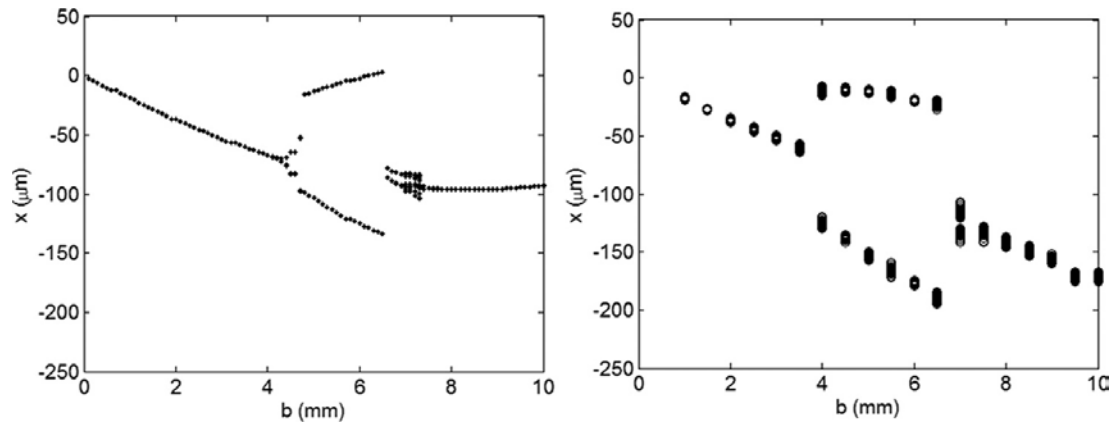
Figure 6.15: Bifurcation diagram for 1.91% damping (3310 rpm). (Left) simulation and (right) experiment.
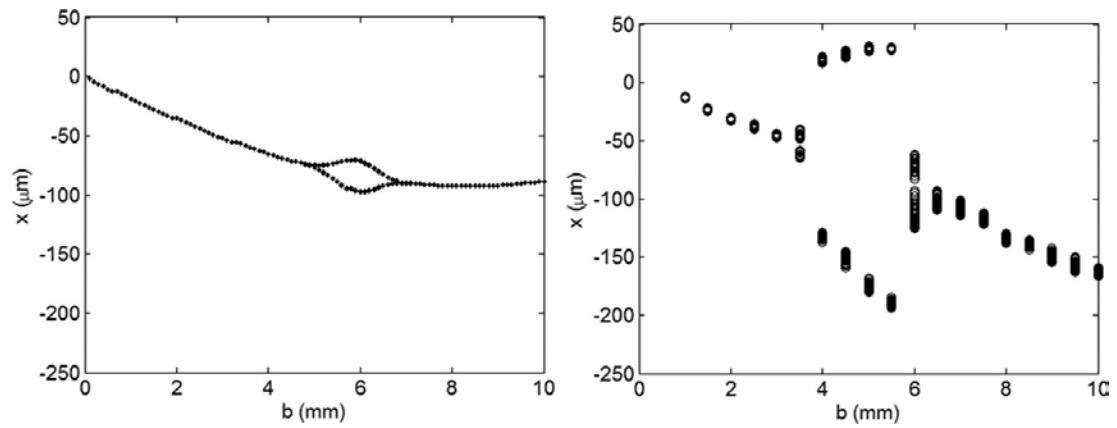
Figure 6.16: Bifurcation diagram for 2.34% damping (3310 rpm). (Left) simulation and (right) experiment.
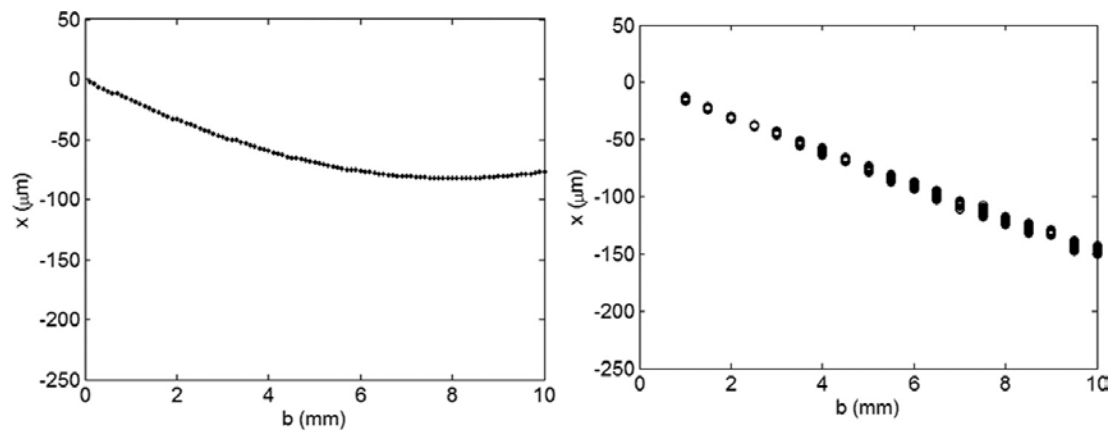
Figure 6.17: Bifurcation diagram for 3.55% damping (3310 rpm). (Left) simulation and (right) experiment.
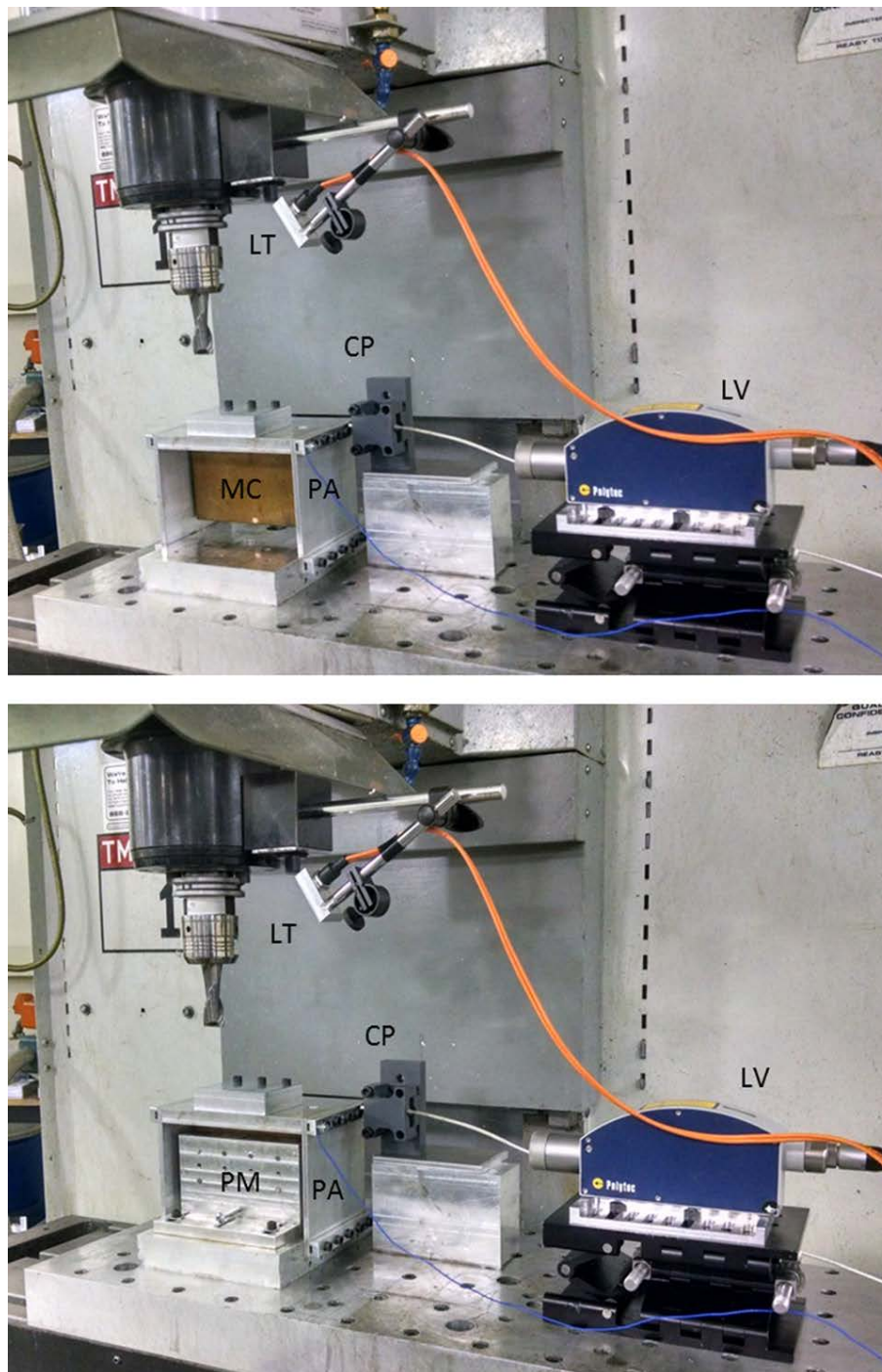
Figure 6.18: Milling experimental setup with variable viscous damping. The setup includes a laser vibrometer (LV), low mass piezo accelerometer (PA), laser tachometer (LT), capacitance probe (CP), moving copper conductor (MC), and permanent magnet (PM); the copper conductor is visible inside the parallelogram leaf-type flexure. The

lower photograph shows the PM in place. The magnets are positioned on both sides of the copper conductor and provide the eddy current damping effect.

To observe the global behavior, stability maps were generated using the same time domain simulation implemented to construct Figures 6.14-6.17. The spindle speed range was 2600 rpm to 3800 rpm in steps of 20 rpm and the axial depth range was 0.2 mm to 10 mm in steps of 0.2 mm. The results are presented in Figures 6.19-6.22, where a vertical line is added to each figure at 3310 rpm to indicate the position of the bifurcation diagrams in Figures 6.14-6.17. The stability metric defined in Eq. (18) was used to identify stable and unstable conditions for each grid point.
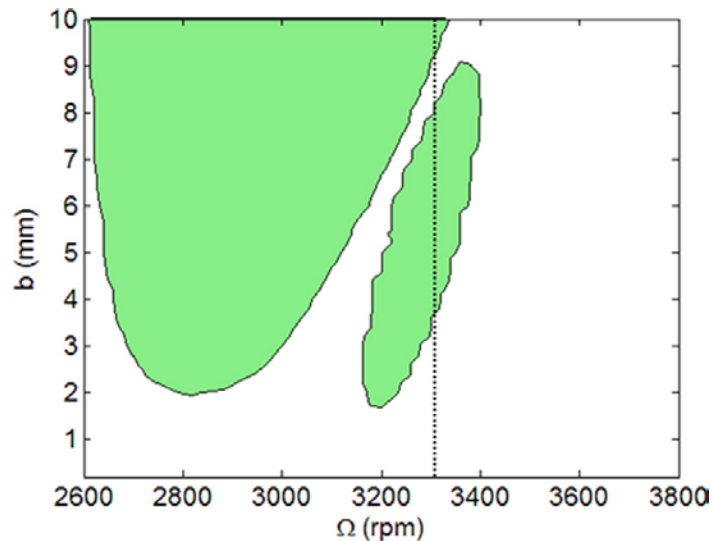
Figure 6.19: Simulated stability map for 1.47% damping ($M = 1$ μm contour). As the axial depth is increased, the transition from stable to period-2 (3.8 mm), period-2 back to stable (8.2 mm), and stable to quasi-periodic behavior (9.2 mm) is observed.
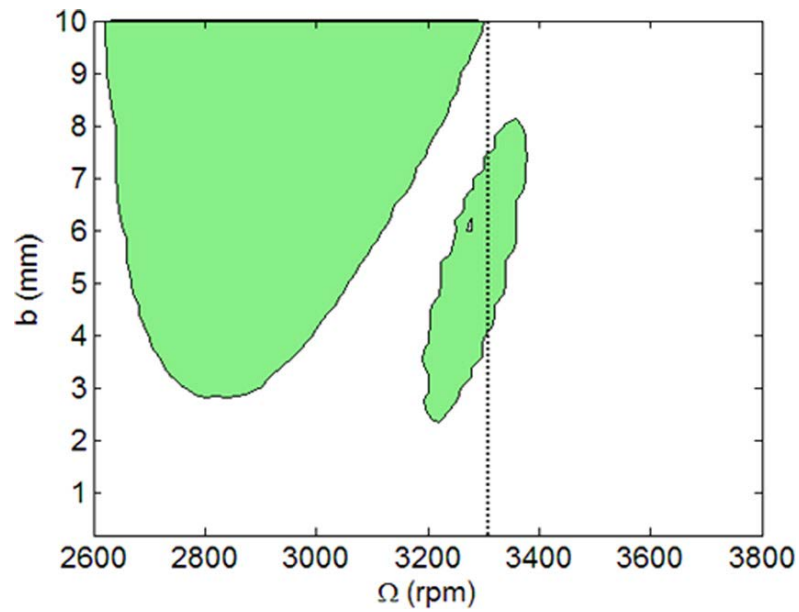
Figure 6.20: Simulated stability map for 1.91% damping ($M = 1\ \mu$m contour). As axial depth is increased, the transition from stable to period-2 (4.2 mm) and period-2 back to stable (7.6 mm) is observed.
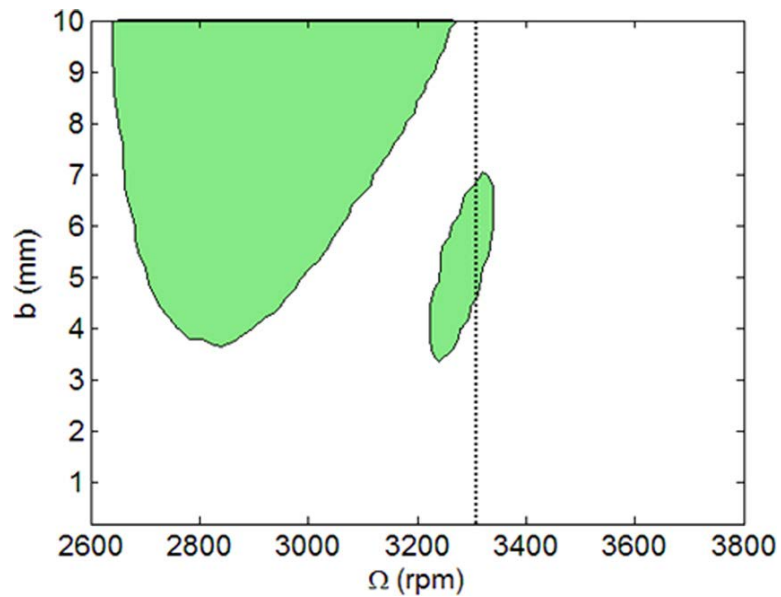
Figure 6.21: Simulated stability map for 2.34% damping ($M = 1\ \mu$m contour). As the axial depth is increased, the transition from stable to period-2 (4.6 mm) and period-2 back to stable (6.8 mm) is observed.
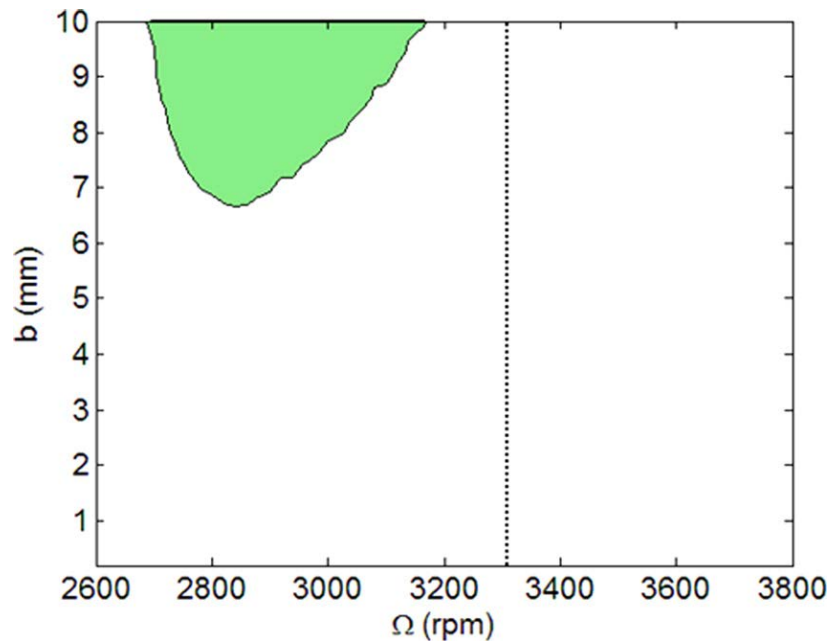
Figure 6.22: Simulated stability map for 3.55% damping ($M = 1$ μm contour). Stable behavior is observed at all axial depths.

6.5 Surface Location Error and Surface Roughness for Period-2 Bifurcations

To demonstrate stability, SLE, and surface roughness results obtained from time domain simulation, a numerical example is presented. The strategy of periodic sampling is applied to differentiate between stable machining and bifurcation behavior. The cutting conditions for the simulation are 5% radial immersion up (conventional) milling at 30,000 rpm with a feed per tooth of 0.1 mm/tooth. The 8 mm diameter, 45 deg helix, single tooth tool has symmetric dynamics with a 721 Hz natural frequency, a viscous damping ratio of 0.009, and a 4.1×10^5 N/m stiffness. The aluminum workpiece cutting force coefficients are $k_{tc} = 604\times10^6$ N/m^2 and $k_{nc} = 223\times10^6$ N/m^2 (zero edge coefficients).

The tool vibration in the feed (x) direction for an axial depth of $b = 0.5$ mm is displayed in Figure 6.23. For this stable cut, the once-per- tooth sampled points (circles) repeat because stable cuts exhibit forced (synchronous) vibrations. The corresponding Poincaré map, which plots displacement versus velocity, is also included in Figure 6.23. It is observed that a single point is obtained from the once-per-tooth (periodic) sampling. This identifies stable behavior that repeats with each tooth passage. Figure 6.24 shows results for $b = 2.5$ mm. This provides an example of period-2 behavior. In this case, the vibration repeats every other tooth passage, so two distinct points are visible in the Poincaré map. Secondary Hopf behavior is demonstrated in Figure 6.25 with $b = 5.0$ mm. Here, the chatter frequency near the system natural frequency causes the quasi-periodic behavior and an elliptical distribution of points appears in the Poincaré map. This distribution is indicative of the traditional, secondary Hopf instability.
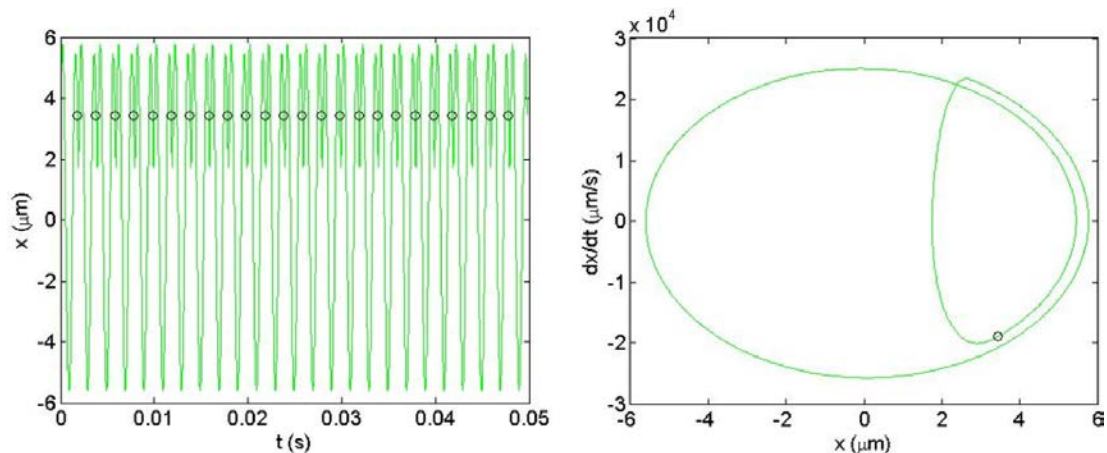
Figure 6.23: (Left) Feed direction (x) vibration versus time with once-per-tooth sampled points (circles) for $b = 0.5$ mm. (Right) Poincaré map with once-per-tooth sampled points. Because the cut is stable, all sampled points appear at the same location.
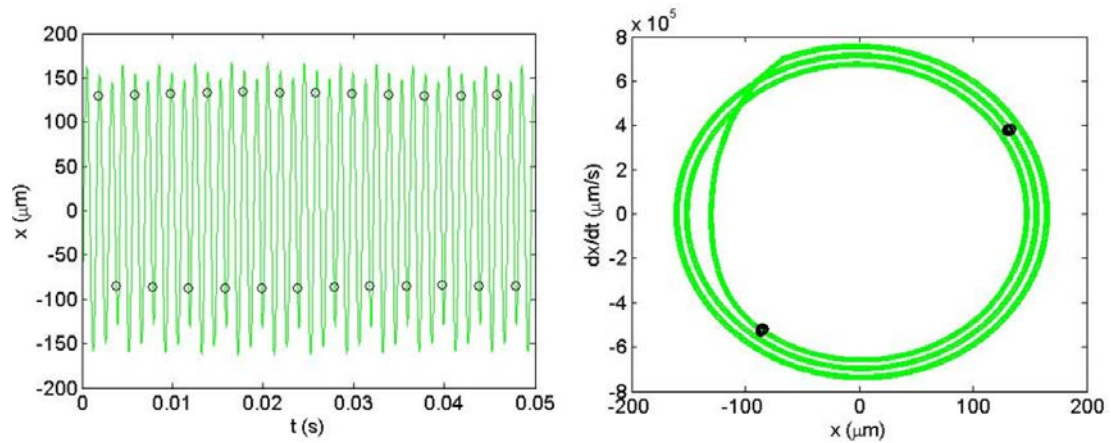
Figure 6.24: (Left) Feed direction (*x*) vibration versus time with once-per-tooth sampled points (circles) for *b* = 2.5 mm. (Right) Poincaré map with once-per-tooth sampled points. The period-2 bifurcation behavior shows two sampled point locations. Because the solution alternates between two values, this is referred to as a flip bifurcation.
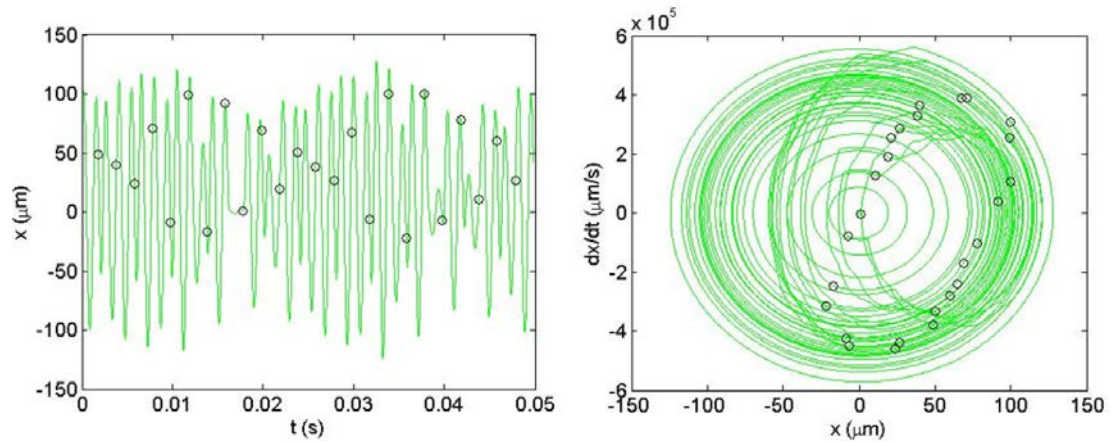
Figure 6.25: (Left) Feed direction (*x*) vibration versus time with once-per-tooth sampled points (circles) for *b* = 5.0 mm. (Right) Poincaré map with once-per-tooth sampled points. The secondary Hopf instability yields an elliptical distribution of sampled points.

The spatial trajectory of the cutter tooth is displayed in Fig. 5. It includes both the nominal path and the vibrations due to the cutting force (i.e., the x solution to Eqs. (5) and (6) is summed with x_{nom} from Eq. (15) and the y solution to Eqs. (5) and (6) is summed with y_{nom} from Eq. (16)). Because this is up milling, the uppermost points define

the machined surface (for down milling, it would be the lowermost points). The upper

surface is shown in more detail in the inset. It is seen that the period-2 behavior causes

the final surface to be defined by every other tooth passage. The trajectories with their

apex at approximately 4006 μm produce the surface, while the alternating trajectories at

approximately 3991 μm remove material, but do not affect the final surface details. In

this case, the surface location error is 6 μm because the 8mm diameter (4mm radius) tool

should leave the surface at 4000 μm. This surface is overcut by 6 μm, i.e., more material

is removed than commanded. The arithmetic average surface roughness for the profile is

Ra = 0.3 μm.
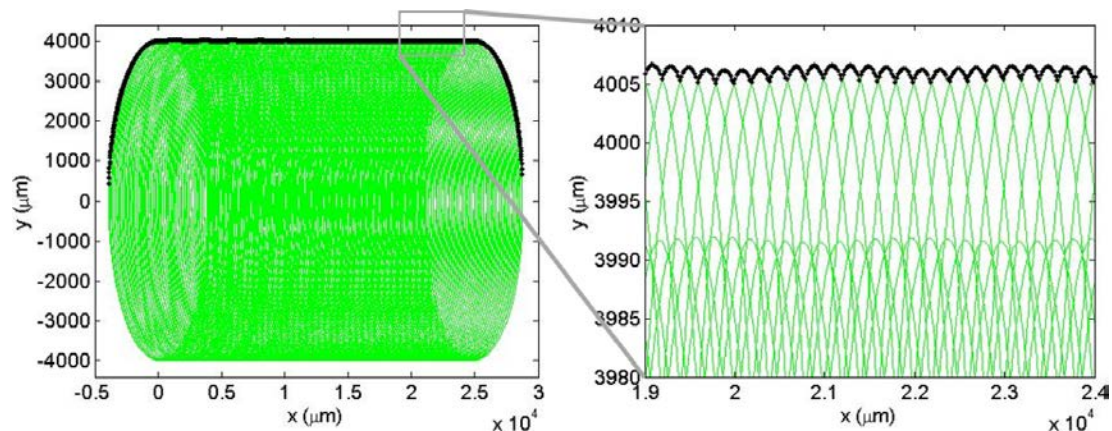
Figure 6.26: (Left) Spatial trajectory of the cutter tooth for $b = 2.5$ mm. (Right) Magnified view of upper surface of tooth trajectory. The machined surface is defined by the points at the top of the trajectory for the up milling cut. The period-2 behavior gives upper and lower tooth paths. The upper path defines the final surface, although material is removed for each tooth passage.

For the selected system dynamics, the traditional stability limit (i.e., the transition

from stable to any bifurcation behavior) at 30,000 rpm is 0.77 mm. At the selected

spindle speed, therefore, the optimum axial depth of cut would be 0.77 mm or less. If the

2.5 mm axial depth that resulted in period-2 behavior was chosen, a 225% increase in material removal rate would be achieved. Provided the 6 μm SLE and 0.3 μm Ra are acceptable for the selected application, this presents a compelling case for machining at the period-2 conditions.

The flexure-based setup displayed in Figure 6.27 was used to define a physical system for simulation and testing [52,53]. The setup included a parallelogram leaf-type flexure with an aluminum workpiece mounted on top. The in-process vibration data were collected using a Polytec OFV-5000 laser vibrometer (velocity) and Lion Precision DMT20 capacitance probe (displacement). Both were aligned with the flexible direction for the single degree-of-freedom flexure. Note that the feed direction is perpendicular to this flexible direction. This orientation was selected to emphasize variations in surface location error and surface finish with machining conditions. Once-per-tooth sampling was accomplished using a laser tachometer (LT), where the reflective target was attached to the rotating tool holder. The flexure dynamics were identified by modal testing: 125.8 Hz natural frequency, 0.0136 viscous damping ratio, and 1.75×10^6 N/m stiffness in the flexible (feed) direction. The dynamics for the 19.1 mm diameter, 0 deg helix angle tool (one insert) were symmetric: 1188 Hz natural frequency, 0.095 viscous damping ratio, and 4.24×10^7 N/m stiffness. The 6061-T6 aluminum alloy cutting force coefficients were: $k_{tc} = 770\times10^6$ N/m^2, $k_{nc} = 368\times10^6$ N/m^2, $k_{te} = 22\times10^3$ N/m, and $k_{ne} = 22\times10^3$ N/m. The up milling cutting conditions were: 5 mm axial depth, 2 mm radial depth, 0.35 mm/tooth, and variable spindle speed. Spindle speed values were selected to span from period-2 to

stable cutting conditions while holding all other parameters constant. These spindle

speeds and the corresponding behavior are listed in columns one and two of Table 6.5.
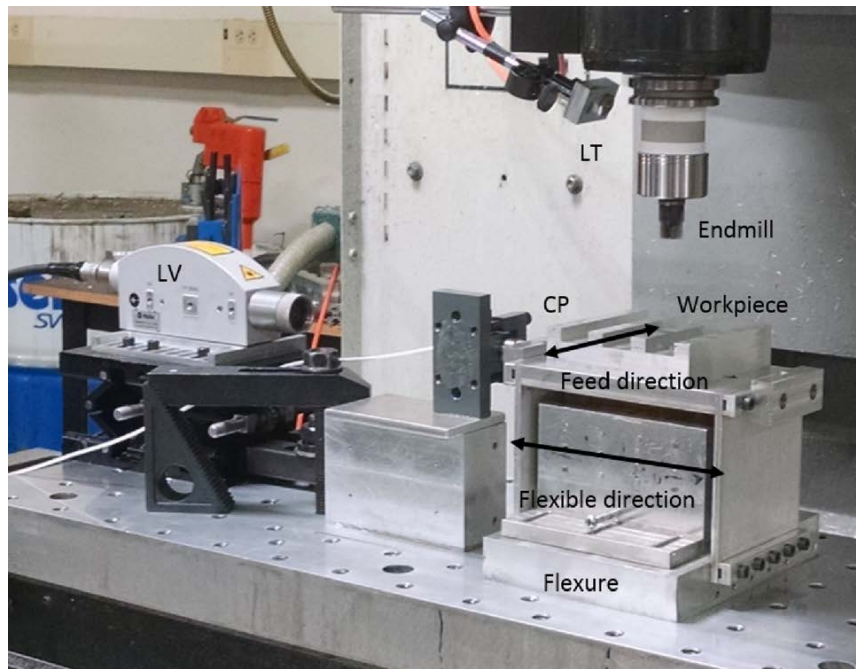
Figure 6.27: Flexure-based experimental setup with laser vibrometer (LV), laser tachometer (LT), and capacitance probe (CP). The feed direction and the flexible direction for the single degree-of-freedom flexure are also identified. The setup was located on a Haas TM-1 CNC milling machine.

The workpiece geometry is presented in Figure 6.28. The initial ribs were

machined directly on the flexure so it could be ensured that the part was aligned with the

machine axes. Low axial and radial depths were selected to minimize vibration levels and

the same conditions were used to machine each rib. Prior to beginning the SLE/Ra

experiments, a test workpiece was machined and the four ribs were

measured on a coordinate measuring machine (CMM) to evaluate the repeatability of the

starting rib dimensions (Zeiss Prismo). The mean value was 9.82 mm with a standard

deviation of 2.8 μm. Given the adequate repeatability of the initial ribs, the 11 spindle

speeds in Table 6.5 were used to machine 11 ribs (three total workpieces). All machining

conditions were identical other than spindle speed.
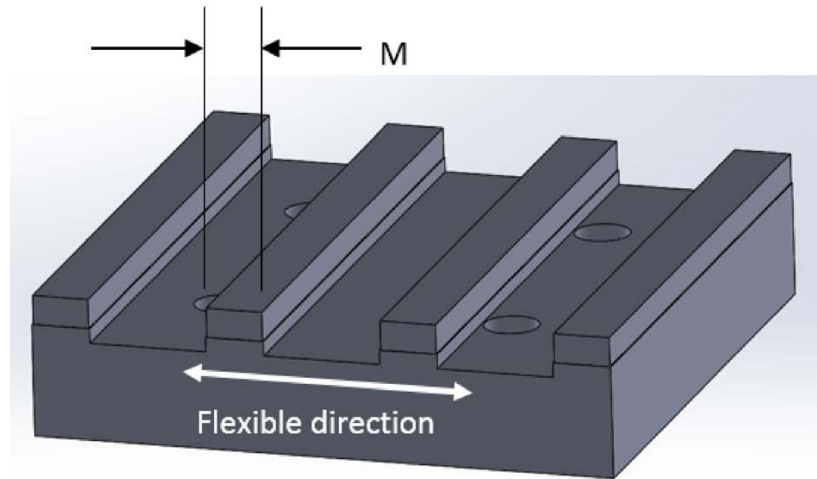
Figure 6.28: The workpiece included four ribs that were initially machined to the same
dimensions. The {5 mm axial depth, 2 mm radial depth} cuts were then performed on one
edge at a different spindle speed for each rib. The SLE was calculated as the difference
between the commanded, C, and measured, M, rib widths. The flexible direction for the
flexure is identified.

Table 6.5: Comparison of measured and predicted SLE results for rib cutting tests

Spindle speed (rpm)	Behavior	Measured SLE (μm)	Predicted SLE (μm)	Error (μm)
3180	Period-2	-4	0	-4
3190	Period-2	-8	-6	-2
3200	Period-2	-13	-15	+2
3210	Period-2	-19	-21	+2
3270	Stable	-29	-30	+1
3300	Stable	-32	-32	0
3330	Stable	-33	-35	+2
3360	Stable	-38	-38	0
3400	Stable	-44	-42	-2
3500	Stable	-55	-58	+3
3600	Stable	-90	-85	-5

The predicted and measured Poincaré maps for three of the 11 spindle speeds are presented in Figures 6.29-6.31. Figure 6.29 displays the 3180 rpm results that exhibit period-2 behavior. Figures 6.30 and 6.31 both demonstrate stable behavior (3300 rpm and 3600 rpm, respectively). The vibration amplitude is larger in Figure 6.31 because this spindle speed is nearer to the first integer fraction of the resonant spindle speed ((125.8 × 60)/2 = 7548/2 = 3774 rpm). The forced vibration amplitude is therefore increased. This would be considered a "best" spindle speed in traditional analyses because it identifies the peak of the corresponding secondary Hopf stability lobe.

The SLE results are presented in Figure 6.32 and Table 6.5. Four tests were completed under period-2 conditions and seven were performed under stable conditions. Good agreement is observed between prediction and measurement. The average error between prediction and measurement is 0.5 μm for the 11 tests.
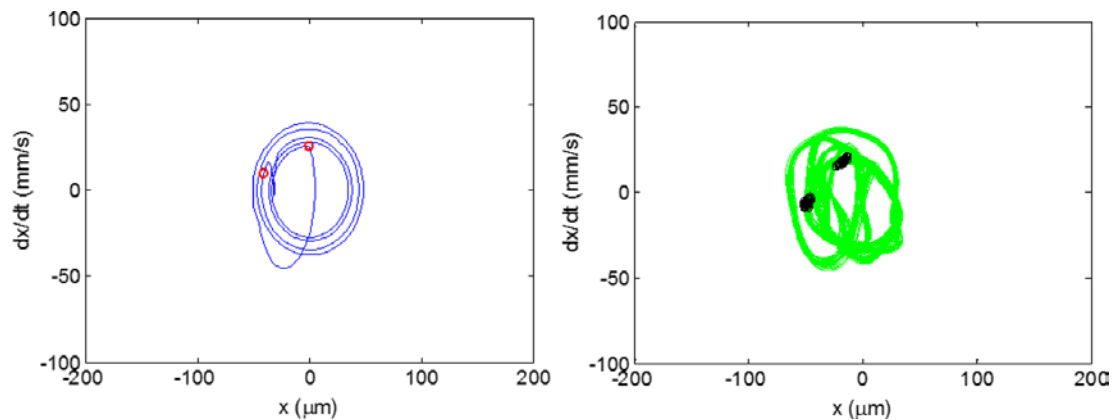
Figure 6.29: Predicted (left) and measured (right) Poincaré maps for 3180 rpm. Period-2 behavior is seen. Note that *x* indicates the flexible direction for the flexure. The feed direction was *y* for these experiments.
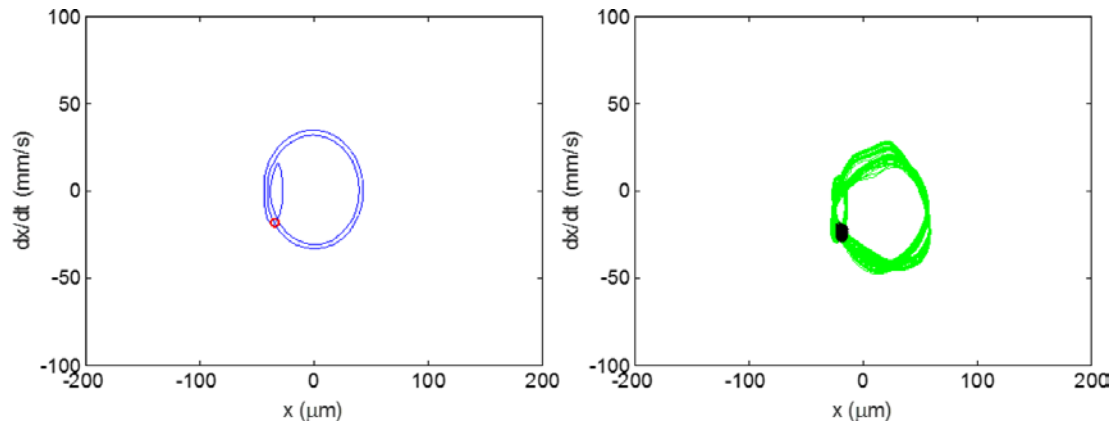
Figure 6.30: Predicted (left) and measured (right) Poincaré maps for 3300 rpm. Stable behavior is seen.
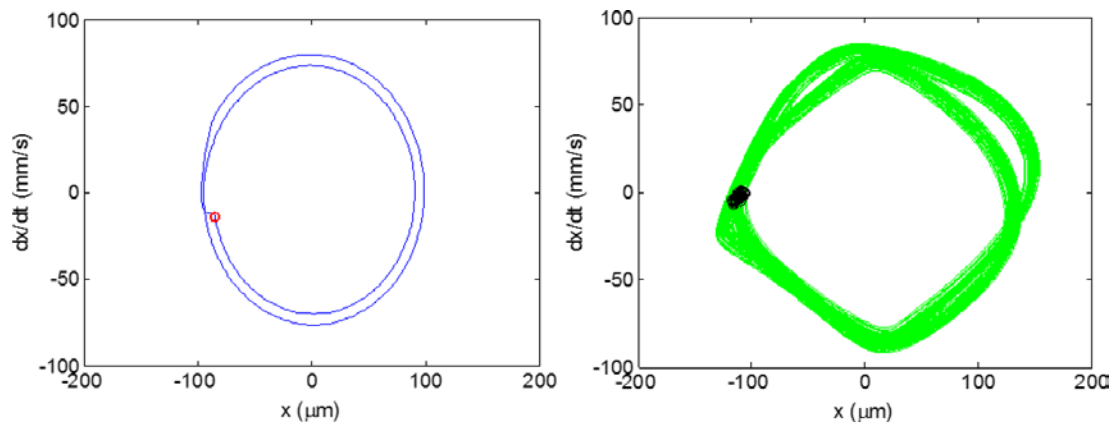
Figure 6.31: Predicted (left) and measured (right) Poincaré maps for 3600 rpm. Stable behavior is seen with increased amplitude relative to 3300 rpm (Figure 6.30).
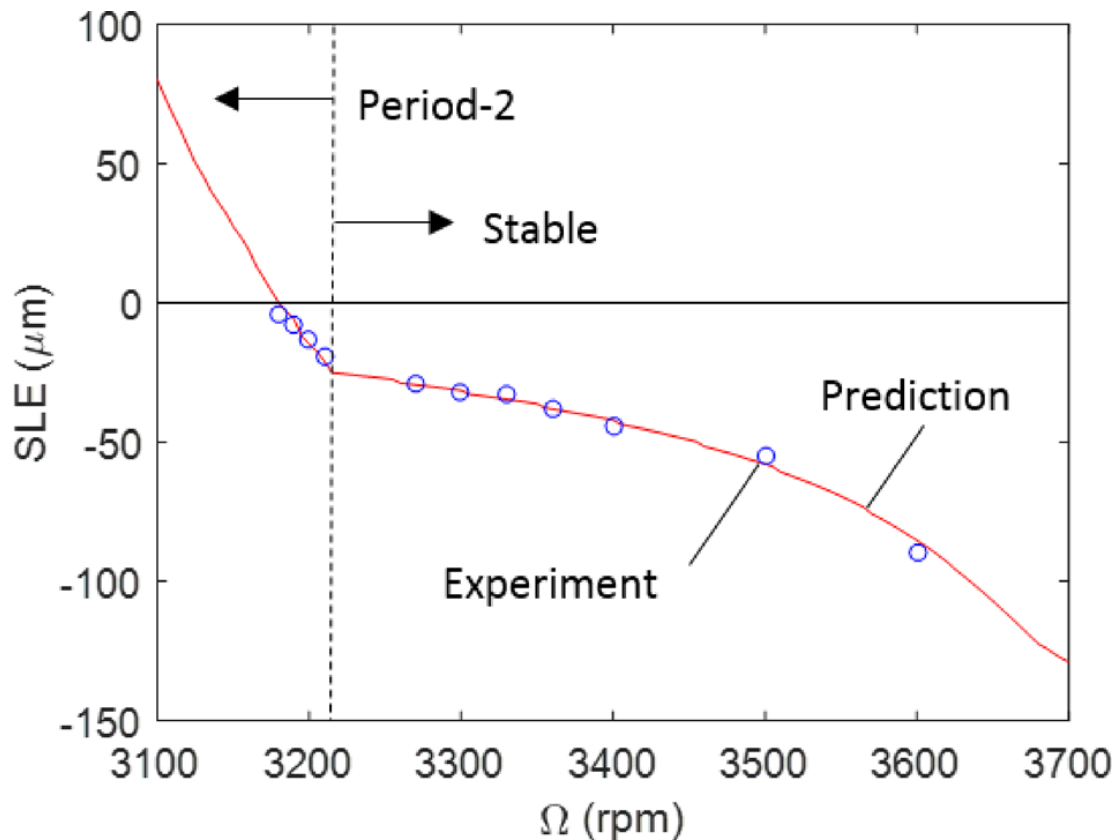
Figure 6.32: SLE prediction from time domain simulation (line) and experimental results from rib cutting tests (circles). The four period-2 bifurcation tests are identified.

Figures 6.33- 6.35 provide a direct comparison between the time domain simulation and the CMM surface points obtained by continuous scanning along the machined surface. In these figures, the commanded surface is identified by the dashed line, the solid line is the CMM data, and the circles are the simulation results. The SLE is the difference between the commanded and actual surface and, again, good agreement is observed between simulation and measurement.
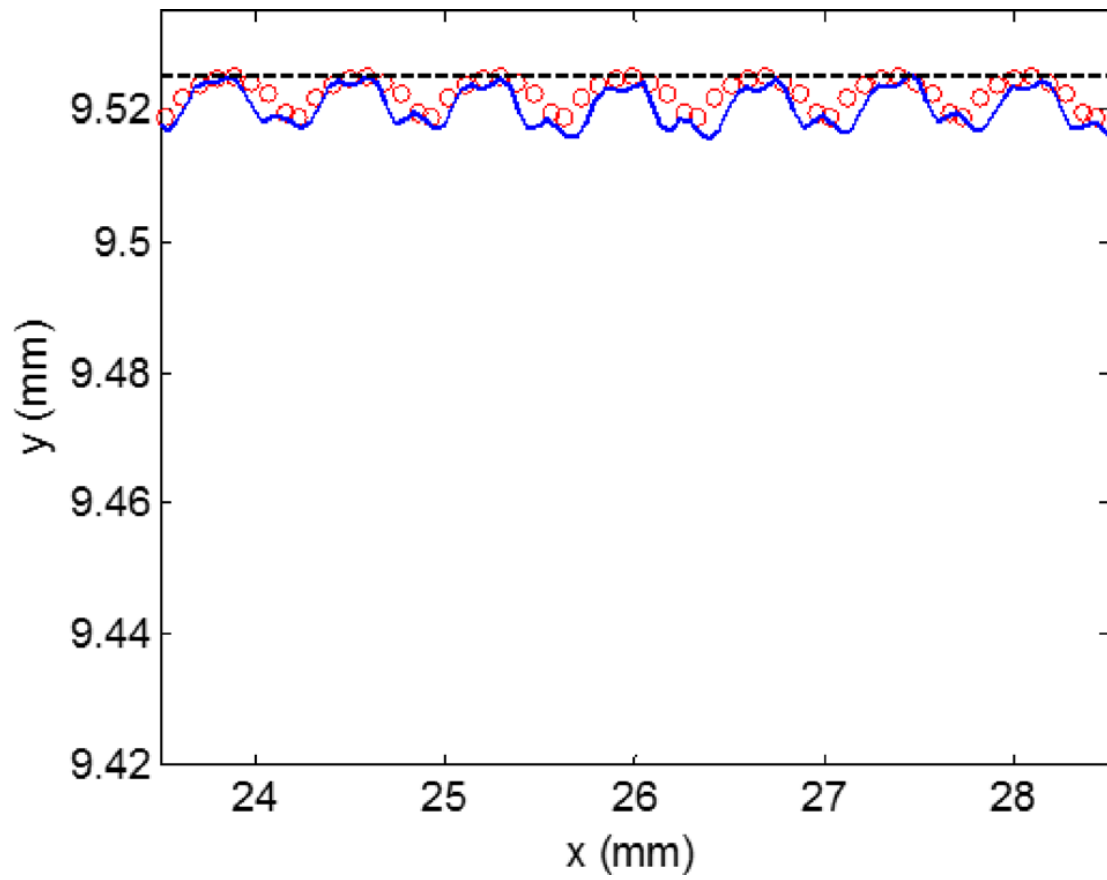
Figure 6.33: Commanded surface (dashed line), CMM scan (solid line), and simulation result (circles) for 3180 rpm (period-2). These results correspond to Figure 6.29.
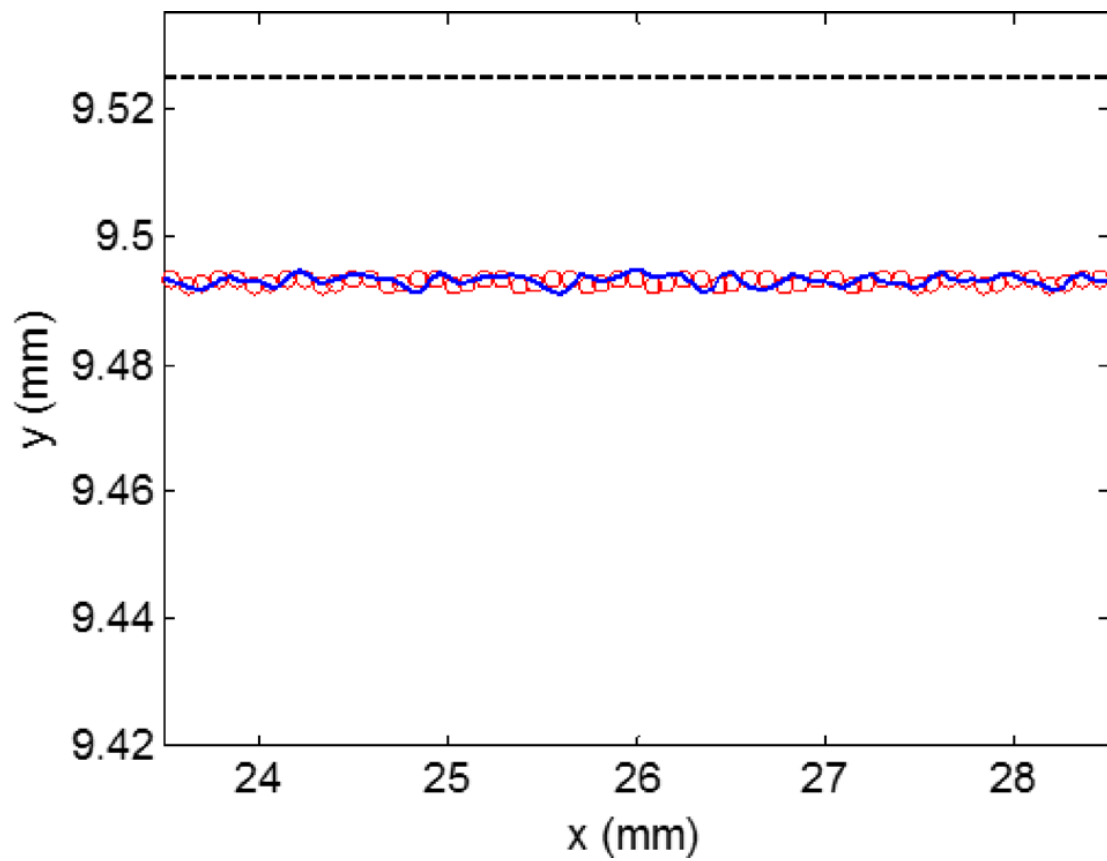
Figure 6.34: Commanded surface (dashed line), CMM scan (solid line), and simulation results (circles) for 3300 rpm (stable). These results correspond to Figure 6.30.
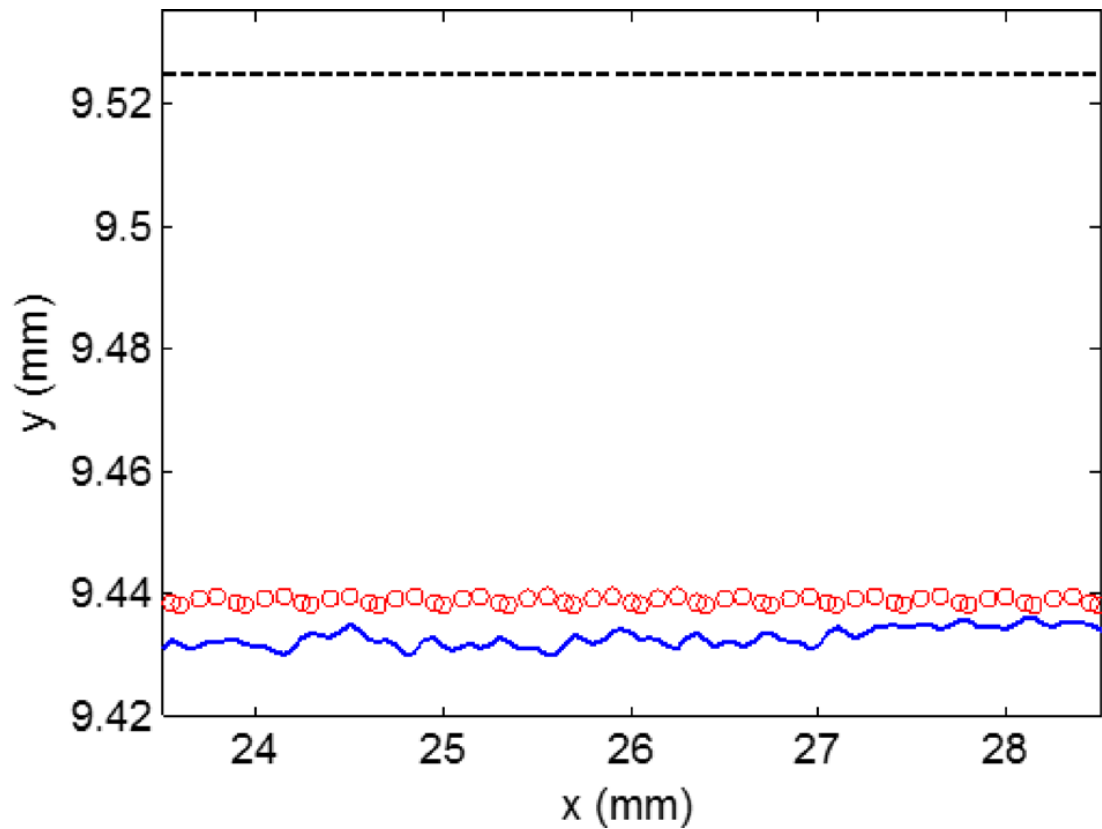
Figure 6.35: Commanded surface (dashed line), CMM scan (solid line), and simulation results (circles) for 3600 rpm (stable). These results correspond to Figure 6.31.

The surface roughness was also measured using a scanning white light interferometer (ZeGage, Zygo Corporation, Middlefield, CT). These results are presented in Table 6.6, where the Ra values were calculated from a line scan at the midpoint of the axial depth of cut extracted from the surface topography. The Ra

is clearly larger for the period-2 conditions, where every other tool passage defines the surface roughness. The mean Ra for the period-2 conditions (four tests, 1.87 μm) is 5.2 times larger than the mean Ra for the stable conditions (seven tests, 0.36 μm).

Table 6.6: Surface roughness results for rib cutting tests

Spindle speed (rpm)	Behavior	Ra (μm)
3180	Period-2	1.76
3190	Period-2	1.77
3200	Period-2	1.87
3210	Period-2	2.09
3270	Stable	0.28
3300	Stable	0.35
3330	Stable	0.44
3360	Stable	0.34
3400	Stable	0.39
3500	Stable	0.36
3600	Stable	0.35

The predicted and measured surface profiles are compared in Figures 6.36-6.38. The change in cusp height and spacing between the period-2 (Figure 6.36) and stable (Figures 6.37 and 6.38) results is clearly seen.
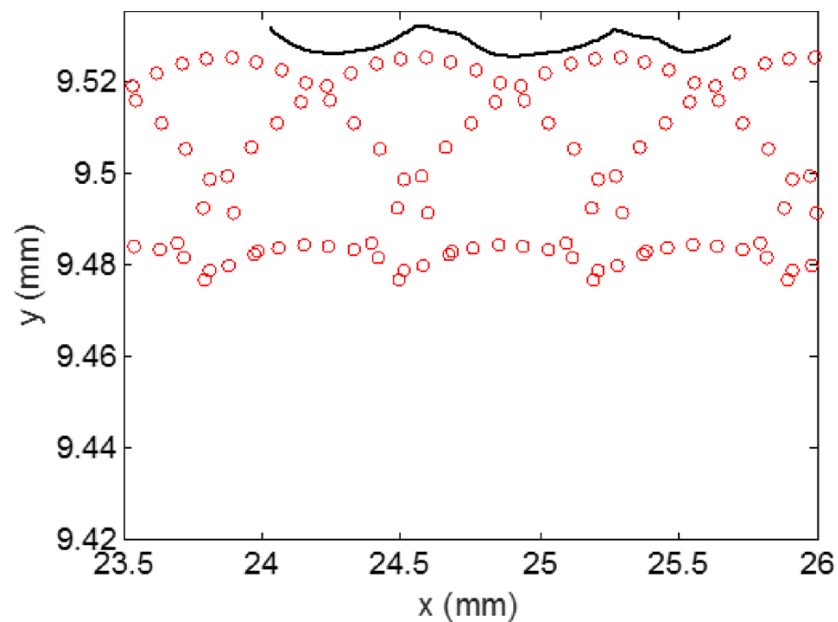
Figure 6.36: Scanning white light interferometer line scan (line) and simulation results (circles) for 3180 rpm (period-2)
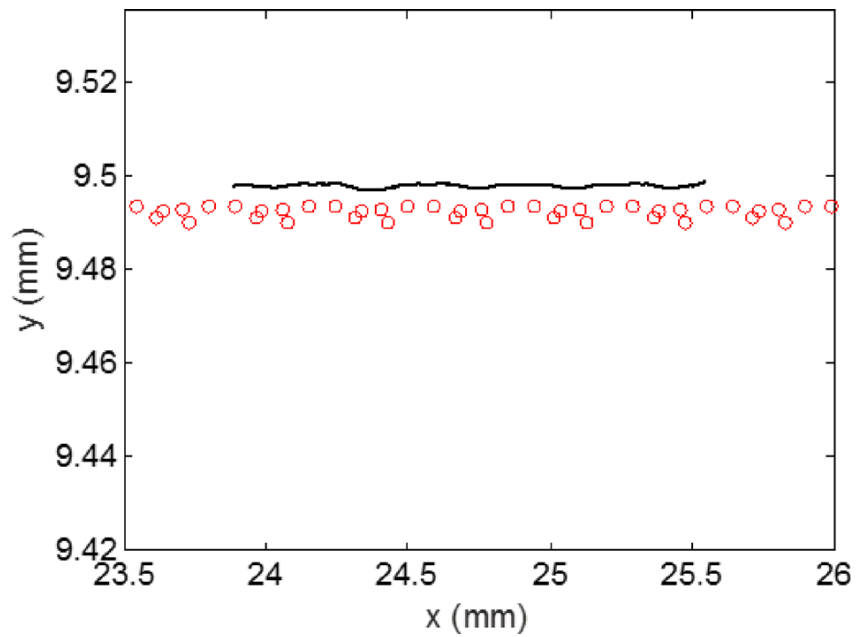
Figure 6.37: Scanning white light interferometer line scan (line) and simulation results (circles) for 3300 rpm (stable)
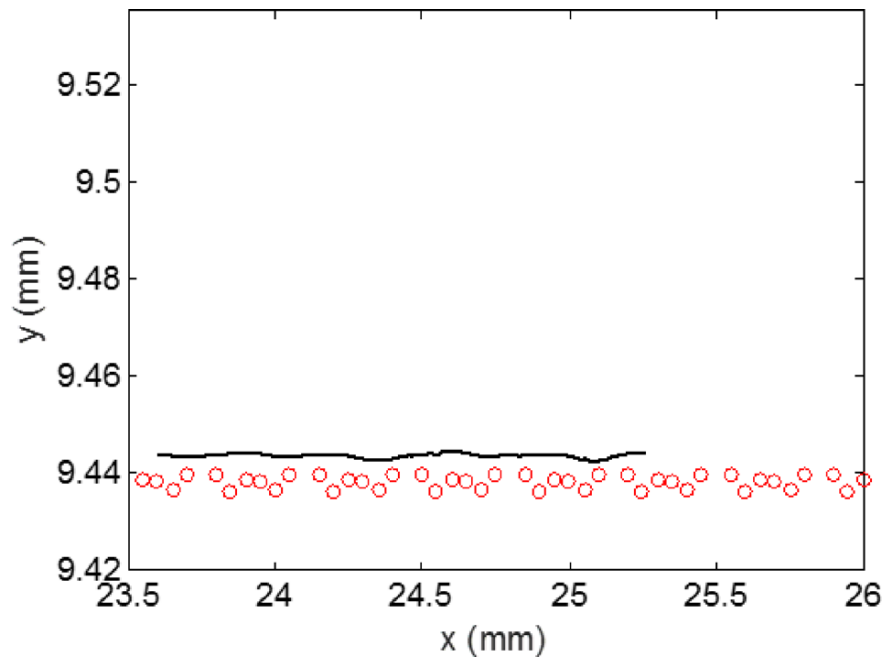
Figure 6.38: Scanning white light interferometer line scan (line) and simulation results (circles) for 3600 rpm (stable)

The stability and SLE information are combined in Figure 6.39. In Figure 6.39, the dark area represents secondary Hopf instability, the dotted area identifies the period-2 bifurcations, and the contour lines give the SLE as a function of spindle speed (horizontal axis) and axial depth of cut (vertical axis). Zero SLE is seen near the traditional best speed of 3774 rpm. However, a steep gradient for small changes in spindle speed is also seen near this speed (i.e., the zero SLE contour is vertical). A zero SLE contour is also observed within the period-2 zone. Interestingly, the SLE gradient is not as steep within the period-2 zone as it is near the best speed at 3774 rpm. This also supports the possibility of producing acceptable parts under period-2 bifurcation machining conditions.
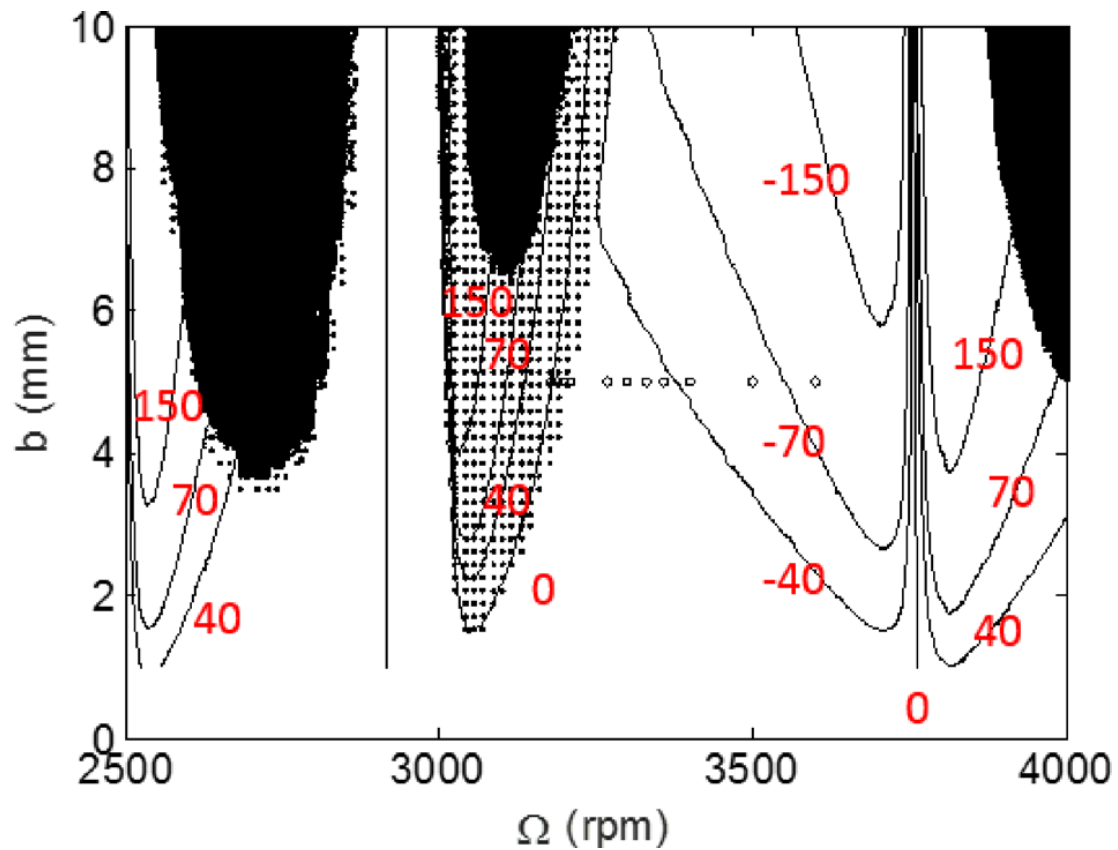
Figure 6.39: Combined stability and SLE map for rib cutting process dynamics. The secondary Hopf instability is represented by the dark zone, the period-2 behavior is identified by the dotted zone, and the SLE is given by the contours (i.e., lines of constant SLE).

Surface location error and surface roughness predictions were completed using time domain simulation for both stable and period-2 milling conditions. The predictions were compared to experiment using a flexure-based platform with displacement and velocity metrology. It was observed that the simulation accurately predicted the milling performance using: (1) Poincaré maps, which plot the displacement versus velocity and are used to identify period-2 behavior via periodic sampling; (2) surface location error measurements completed using a coordinate measuring machine; and (3) surface

roughness measurements carried out using a scanning white light interferometer. It was shown that the surface location error for period-2 (unstable) behavior follows similar trends observed for (stable) forced vibration, so zero or low error conditions may be selected even for period-2 bifurcation conditions. The surface roughness for the period-2 instability was seen to be larger than for stable conditions, although the final surface was still periodic. This increase in surface roughness occurs because the surface is defined by every other tooth passage and the apparent feed per tooth is increased.

CHAPTER 7: CONCLUSIONS AND FUTURE WORK

7.1   Conclusions

Period-n milling bifurcations were further explored using Poincaré maps, time domain simulation and bifurcation diagrams. The milling time domain simulation described in [27] is further improved so that automated determination of stability is possible. The simulation is also improved with the addition of subharmonic interrogation for the automated determination of period-n bifurcations. These new additions to the time domain simulation allow the global behavior of period-n bifurcations to be explored. Human determination of period-n bifurcations is very time consuming and impractical in the study of the global behavior of period-n bifurcations.

The traditional binary description of milling stability should be altered to accommodate different types of instabilities such as secondary Hopf and period-n bifurcations. Milling behavior can now be explored at axial depths of cut that are well beyond the traditional stability limit. New insights and strategies may be discovered and exploited due to the improvements of the time domain milling simulation. Manufacturers are always seeking to increase material removal rates thereby decreasing cycle times and increasing production rates. Experimental exploration of the traditional unstable zones can be very expensive and time consuming due to broken tools and labor costs. The enhanced time domain simulation can now explore these regions of traditional instability in order to better understand the different types of unstable behavior and, possibly, secondary zones of stability that are above the traditional stability limit.

Experimental results show good agreement with the simulated (predicted) results.

Period -2, -3, -6, -7, -8, and -15 bifurcations were both predicted by simulation and

validated by experiment. These high order period-n bifurcation are interesting in that they

do not exhibit forced vibration, or a response period equal to the forcing period, τ.

Typically, any response that does not exhibit a period equal to the forcing period is

considered to be unstable. Period-n bifurcations, however, exhibit a response that is an

integer multiple of the forcing period. This suggests that there is some order in the

response. A chaotic and unpredictable response is easily classified as unstable and

unpredictable, but a period-n bifurcation exhibits a repeatable and predictable response

that shares a relationship with the forcing period. Period-n "stability" may have

advantages that have not yet been exploited.

Period-n bifurcations are, however, sensitive to system natural frequencies.

Simulated and experimental results demonstrated that changes to system natural

frequency on the order of 0.1 Hz can cause a system response to no longer exhibit period-

n behavior. This behavior is especially important when the workpiece stiffness is much

lower than the cutting tool stiffness because the workpiece natural frequency will change

due to material removal. Therefore, small changes in workpiece natural frequency can

have large effects on the process behavior.

Period-n bifurcation behavior is also sensitive to damping. Lowly damped tools can

result in global behavior with lens-like period-2 bifurcation islands. However, simulated

and experimental results demonstrated the existence of this period-2 bifurcation island at

low damping ratios (see Figure 6.19) and no period-2 bifurcation island at higher damping ratios while holding all other parameters constant (see Figure 6.22).

Surface location error and surface roughness values were predicted using the time domain simulation under stable and period-2 conditions. These results were validated by experiments. It was observed that period-2 bifurcation behavior results in a higher surface roughness. This higher surface roughness is due to the fact that the two different tool orbits remove material, but only one of the orbits creates a surface. The surface that is left behind is created by every other tooth passage, and therefore, appears to have a doubled feed rate. However, a surface location error of zero is achievable under period-2 bifurcation behavior and the gradient of SLE due to small changes in spindle speed is much smaller near period-2 zones relative to the traditional optimal spindle speeds (see Figure 6.39).

Since cutting speed is often a limiting factor when selecting machining parameters (especially when cutting hard-to-machine metals), it may not be possible to exploit the higher allowable depths of cut available at higher spindle speeds. It has been shown through experiment that machining under period-2 bifurcation behavior can result in low SLE and a higher surface roughness. It may be advantageous to intentionally select machining parameters that result in period-2 behavior due to higher material removal rates. As an example, consider the global stability map presented in Figure 6.39 where the workpiece material is changed to a low carbon steel and the cutting tool is changed to a 12 mm diameter carbide endmill. A typical cutting speed of a carbide tool and low carbon steel is approximately 1100 m/min. This cutting speed would limit the spindle

speed to 3200 rpm. The best spindle speed of 3780 rpm is no longer appropriate due to cutting speed restrictions and the next best spindle speed of 2520 rpm might be selected. A stable cut at a spindle speed of 2520 rpm, axial depth of 8 mm, and radial depth of 2 mm would result in a material removal rate of 14,100 mm^3/min. If a higher surface roughness was acceptable, then the same cut could be made at 3200 rpm which would result in period-2 bifurcation behavior. By intentionally selecting machining parameters that result in period-2 bifurcation behavior, the material removal rate would be 17,900 mm^3/min, which is a 27% increase from the stable cut made at 2520 rpm.

Selecting period-2 bifurcation behavior may also be advantageous at high spindle speeds as well. As an example, consider the bifurcation diagram presented in Figure 4.3. Stable machining is achievable up to an axial depth of 0.77 mm, while period-2 bifurcation behavior is achievable up to an axial depth of 2.5 mm. The surface roughness of period-2 bifurcation behavior is always worse compared to stable machining behavior. If, however, the decrease in surface quality is acceptable, machining at an axial depth of 2.5 mm would result in a 225% increase in material removal rate. Even though the surface created by machining under period-2 conditions results in higher surface roughness, the surface roughness is uniform and appears as a stable cut with double the feed rate. This increase in surface roughness may even be negligible for parts that require post process surface treatment.

Period-2 bifurcations create uniform surface undulations that may be desirable. The surface undulations of surfaces cut under period-2 conditions appear to have been machined under stable conditions with double the feed rate. Ultimately, machining under

period-2 bifurcation conditions may provide an efficient way to create accurate part features that also possess regular surface undulations with a selectable wavelength.

7.2   Remaining Work

The effect of period-2 bifurcation behavior on tool wear was not considered in this work. Aluminum workpieces and carbide tools were specifically chosen so that the effects of tool wear could be removed from the many input variables. If period-2 conditions are to be intentionally selected for a machining operation, it needs to be known what effect the period-2 bifurcation behavior has on tool wear. To better understand the potential effect of non-constant chip load on multiple teeth, the actual chip thickness will be identified in time domain simulation and the tooth-to-tooth variation will be quantified.

Experimental results have shown that period-n bifurcations have periodic responses that are integer multiples of the forcing period. Even though period-n bifurcations are not considered stable under traditional stability theory, they do represent a response that repeats and is predictable. Using automated period-n bifurcation identification and the system dynamics presented in section 6.1, a new global stability map was generated that includes the zones of period-n behavior in the Tlusty N=0 lobe. Figure 7.1 shows this new global stability map.
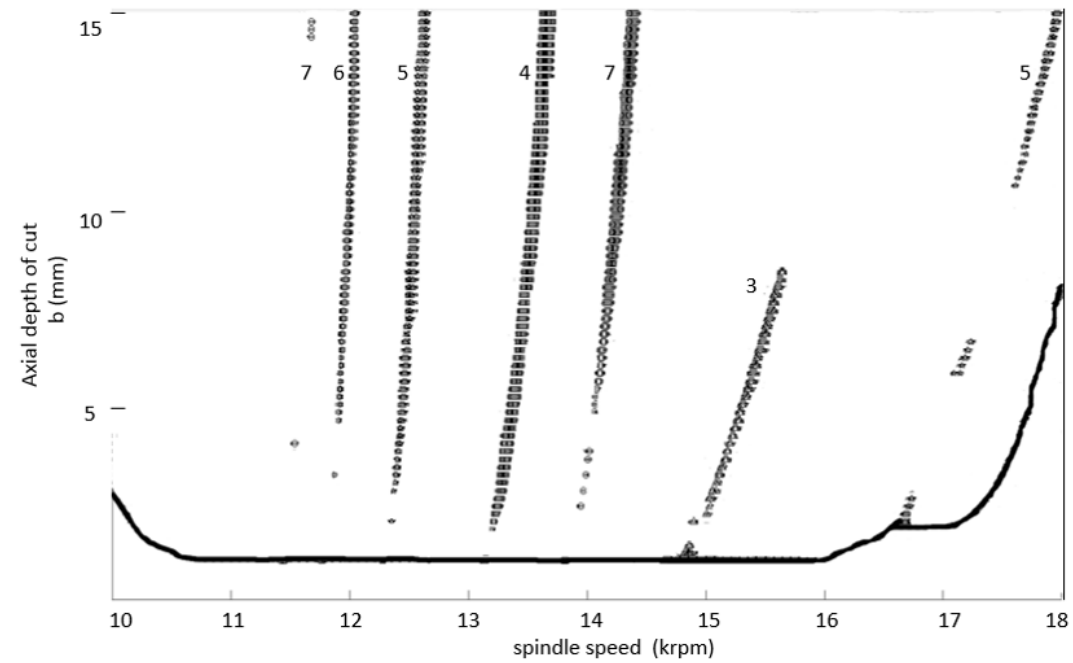
Figure 7.1: Tlusty N=0 lobe global stability map with period-n zones identified.

The period-n zones are identified by the number that is beside the zone. For example, there is a period-7 zone at 14 krpm from 5mm to 15mm axial depth of cut. Everything above the bold black line that is not a period-n zone is secondary Hopf bifurcation behavior and everything below the bold black line is stable behavior. Period-2 behavior is not seen beyond the N=0 lobe. Experimental validation of these period-n bifurcations in the N=0 lobe would also be of value for future work.

REFERENCES

[1]   Arnold, R.N. *The mechanism of tool vibration in the cutting of steel.* Proceedings of the Institue of Mechanical Engineers, 154 (1946).

[2]   Doi, S., and Kato, S. *Chatter vibration of lathe tools.* Transactions of the ASME, 78, 1127-1134 (1956).

[3]   Tobias, S. A., and Fishwick, W. *The chatter of lathe tools under orthogonal cutting conditions.* Transactions of the ASME, 80, 1079-1088 (1958)

[4]   Tlusty, J., and Polacek, M. *The stability of machine tools against self-excited vibrations in machining.* Proceedings of the ASME International Research in Production Engineering Conference, Pittsburgh, PA, 465-474 (1963)

[5]   Tlusty, J., and Polacek, M. *Experience with analyzing stability of machine tool against chatter.* Proceedings of the 9th MTDR Conference, 521-570 (1968)

[6]   Tobias, S. A., *Machine Tool Vibration.* New York: Wiley. (1965)

[7]   Merritt, H. E., *Theory of self-excited machine-tool chatter.* ASME Journal of Engineering for Industry, 87, 447-454. (1965)

[8]   Shridar, R., Hohn, R. E., and Long, G. W., *A general formulation of the milling process equation.* ASME Journal of Engineering for Industry, 90, 317-324 (1968)

[9]   Shridar, R., Hohn, R. E., and Long, G. W., *A stability algorithm for the general milling process.* ASME Journal of Engineering for Industry, 90, 330-334 (1968)

[10]   Hohn, R. E., Shridar, R., and Long, G. W., *A stability algorithm for a special case of the milling process.* ASME Journal of Engineering for Industry, 90, 326-329 (1968)

[11]   Hanna, N. H., and Tobias, S. A., *A theory of nonlinear regenerative chatter.* ASME Journal of Engineering of Industry, 96, 247-255 (1974)

[12]   Tlusty, J., and Ismail, F., *Basic non-linearity in machining chatter.* Annals of the CIRP, 30, 299-304 (1981)

[13]   Tlusty, J., and Ismail, F., *Special aspects of chatter in milling.* ASME Journal of Vibration, Stress and Reliability in Design, 105, 24-32 (1983)

[14]   Tlusty, J., *Machine dynamics.* Handbook of High-speed Machining Technology (Ed. R.I. King). New York: Chapman and Hall, 48-153 (1985)

[15]   Tlusty, J., *Dynamics of high-speed milling*. ASME Journal of Engineering for Industry, 108, 59-67 (1986)

[16]   Minis, I., and Yanusevsky, R., *A new theoretical approach for prediction of chatter in milling.* ASME Journal of Engineering for Industry, 115, 1-8 (1993)

[17]   Altintas, Y., and Budak, E., *Analytical prediction of stability lobes in milling.* Annals of the CIRP, 44(1), 357-362 (1995)

[18]   Davies, M. A., Dutterer, B. S., Pratt, J. R., and Schaut, A. J., *On the dynamics of high-speed milling with long, slender endmills.* Annals of the CIRP, 47(1), 55-60 (1998)

[19]   Moon, F. C., and Kalmár-Nagy, T., *Nonlinear models for complex dynamics in cutting materials.* Philosophical Transactions of the Royal Society London A, 359: 695-711 (2001)

[20]   Davies, M. A., Pratt, J. R., Dutterer, B. S., and Burns, T. J., *The stability of low radial immersion milling*. Annals of the CIRP, 49(1), 37-40 (2000)

[21]   Moon, F. C., *Chaotic dynamics and fractals in material removal processes.* Nonlinearity and Chaos in Engineering Dynamics (Dr. J. Thompson and S. Bishop), Wiley, 25-37 (1994)

[22]   Bukkapatnam, S., Lakhtakia, A., and Kumara, S., *Analysis of sensor signals shows turning on a lathe exhibits low-dimensional chaos.* Physics Review E, 52, 2375-2387 (1995)

[23]   Stépán, G. and Kalmár-Nagy, T., *Nonlinear regenerative machine tool vibrations.* Proceedings of the 1997 ASME Design Engineering Technical conference on Vibration and Noise. Sacramento, CA, DETC 97/VIB-4021, 1-11 (1997)

[24]   Nayfey, A., Chine, C., and Pratt, J., *Applications of perturbations methods to tool chatter dynamics.* Dynamics and Chaos in Manufacturing Processes (Ed F.C. Moon), Wiley, 193-213 (1998)

[25]   Minis, I., and Berger, B. S., *Modelling, analysis, and characterization of machining dynamics.* Dynamics and Chaos in Manufacturing Processes (Ed. F.C. Moon), Wiley, 125-163

[26] Moon, F. C., and Johnson, M., *Nonlinear dynamics and chaos in manufacturing processes*. Dynamics and Chaos in Manufacturing Processes (Ed. F.C. Moon), Wiley, 3-32 (1998)

[27] Smith, K. S., and Tlusty, J., *An overview of modeling and simulation of the milling process.* ASME Journal of Engineering for Industry, 113, 169-175 (1991)

[28] Campomanes, M. L., and Altintas, Y., *An improved time domain simulation for dynamic milling at small radial immersions.* ASME Journal of Manufacturing Science and Engineering, 125(3), 416-422 (2003)

[29] Zhao, M. X., and Balachandran, B., *Dynamics and stability of milling process*. International Journal of Solids and Structures, 38, 2233-2248 (2001)

[30] Davies, M. A., Pratt, J. R., Dutterer, B. S., and Burns, T. J., *Stability prediction for low radial immersion in milling.* ASME Journal of Manufacturing Science and Engineering, 124, 217-225 (2002)

[31] Mann, B. P., Insperger, T., Bayly, P. V., and Stéfán, G., *Stability of up-milling and down-milling, Part 2: Experimental verification.* International Journal of Machine Tools and Manufacture 2003, 43(1), 35-40 (2003)

[32] Mann, B. P., Insperger, T., Bayly, P. V., and Stépán, G., *Stability of up-milling and down-milling, Part 1: Alternative analytical methods.* International Journal of Machine Tools and Manufacture, 43(1), 25-34 (2003)

[33] Insperger, T., Stépán, G., Bayly, P. V., and Mann, B. P., *Multiple chatter frequencies in milling processes.* Journal of Sound and Vibration, 262, 333-345 (2003)

[34] Insperger, T., and Stépán, G., *Vibration frequencies in high-speed milling processes or A positive answer to Davies, Pratt, Dutterer, and Burns.* ASME Journal of Manufacturing Science and Engineering, 126(3), 481-487 (2004)

[35] Mann, B. P., Bayly, P. V., Davies, M. A., and Halley, J. E., *Limit cycles, bifurcations, and accuracy of the milling process.* Journal of Sound and Vibration 2004, 277, 31-48 (2004(

[36] Merdol, S. D., and Altintas, Y., *Multi frequency solution of chatter stability for low immersion milling*. ASME Journal of Manufacturing Science and Engineering, 126, 459-466 (2004)

[37]   Govekar, E., Gradišek, J., Kalveram, M., Insperger, T., Weinert, K., Stépán, G., and Grabec, I., *On stability and dynamics of milling at small radial immersions.* Annals of the CIRP, 54(1), 357-362 (2005)

[38]   Gradišek, J., Kalveram, M., Insperger, T., Weinert, K., Stépán, G., Govekar, E., and Grabec, I., *On stability prediction for milling.* International Journal of Machine Tools and Manufacture, 45(7-8), 769-781 (2005)

[39]   Mann, B. P., Garg, N. K., Young, K. A., and Helvey, A. M., *Milling bifurcations from structural asymmetry and nonlinear regeneration.* Nonlinear Dynamics, 42(4), 319-337 (2005)

[40]   Stépán, G., Szalai, R., Mann, B. P., Bayly, P. V., Insperger, T., Gradišek, J., and Govekar, E., *Nonlinear dynamics of high-speed milling – Analysis, numerics, and experiments.* Journal of Vibration and Acoustics, 127, 197-203 (2005)

[41]   Zatarain, M., Muñoa, J., Peigné, G., and Insperger, T., *Analysis of the influence of mill helix angle on chatter stability.* Annals of the CIRP, 55(1), 365-368 (2006)

[42]   Insperger, T., Muñoa, J., Zatarain, M. A., and Peigné, G., *Unstable islands in the stability chart of milling processes due to the helix angle*. CIRP 2nd International Conference on High Performance cutting, Vancouver, Canada, June, 12-13 (2006)

[43]   Patel, B. R., Mann, B. P., and Young, K. A., *Uncharted islands of chatter instability in milling.* International Journal of Machine Tools and Manufacture, 48(1), 124-134 (2008)

[44]   Schmitz, T., Davies, M., Medicus, K., and Snyder, J., *Improving High-Speed Machining Material Removal Rates by Rapid Dynamic Analysis.* Annals of the CIRP, 50(1), 263-268 (2001)

[45]   Schmitz, T., Medicus, K., and Dutterer, B., *Exploring Once-Per-Revolution Audio Signal Variance as a Chatter Indicator.* Machining Science and Technology, 6(2), 215-233 (2002)

[46]   Schmitz, T., *Chatter Recognition by a Statistical Evaluation of the Synchronously Sampled Audio Signal.* Journal of Sound and Vibration, 262(3), 721-730 (2003)

[47]   Schmitz, T., Smith, S., *Machining dynamics: frequency response to improved productivity.* New York, NY: Springer (2009)

[48]   Altintas, Y., *Manufacturing automation: metal cutting mechanics, machine tool vibrations, and CNC design.* 2nd Ed. New York, NY: Cambridge University Press (2012)

[49]   Altintas, Y., Weck, M., *Chatter stability of metal cutting and grinding.* CIRP Annals of Manufacturing Technology, 53(2), 619-642 (2004)

[50]   Smith, S., *Flexures: elements of elastic mechanisms.* London, UK: CRC Press (2000)

[51]   Bai, J. S., Moon, K., Inman, D., *Vibration suppression of a cantilever beam using eddy current damper.* Journal of Sound and Vibrations 284:805-824 (2005)

[52]   Mann, B. P., Insperger, T., Bayly, P.V., and Stépán, G., *Stability of Up-Milling and Down-Milling – Part 2: Experimental Verification.* International Journal of Machine Tools Manufacturing, 43(1) 35-40 (2003)

[53]   Ransom, T., Honeycutt, A., Schmitz, T., *A New Tunable Dynamics Platform for Milling Experiments.* Precision Engineering, 44, 252-256 (2016)

PUBLICATIONS

[1]   Honeycutt, A., and Schmitz, T., *The Extended Milling Bifurcation Diagram.* Procedia Manufacturing 43rd Proceedings, Vol 1, pp. 466-476 (2015)

[2]   Ransom, T., Honeycutt, A., Schmitz, T., *A New Tunable Dynamics Platform for Milling Experiments.* Precision Engineering, 44, 252-256 (2016)

[3]   Honeycutt, A., and Schmitz, T., *Experimental Validation of Period-n Bifurcations in Milling*, Procedia Manufacturing, 44th Proceedings, Vol 5, pp. 362-374 (2016)

[4]   Honeycutt, A., and Schmitz, T., *A new Metric for Automated Stability Identification in Time Domain Milling Simulation*, JMSE, Vol 138, 07450 (2016)

[5]   Honeycutt, A., and Schmitz, T., *A Numerical and Experimental Investigation of Period-n Bifurcations in Milling,* JMSE, Vol 139, 011003, (2016)

[6]   Menezes, J., Rubeo, M., Kiran, K., Honeycutt, A., and Schmitz, T., *Productivity Progression with Tool Wear in Titanium Milling*, Procedia Manufacturing, Vol 5, pp. 427-441 (2016)

[7]   Honeycutt, A., and Schmitz, T., *A Study of Milling Surface Quality during Period-2 Bifurcations,* Procedia Manufacturing, Vol 10, pp. 183-193, (2017)

[8]   Honeycutt, A., and Schmitz, T., *Analytical Solutions for Fixed-free Beam Dynamics in Thin Rib Machining*, Journal of Manufacturing Processes, Vol 30, pp.41-50, (2017)

[9]   Honeycutt, A., and Schmitz, T., *Milling Stability Interrogation by Subharmonic Sampling*, JMSE, Vol 139, 041009, (2017)

[10]   Honeycutt, A., and Schmitz, T., *Surface Location Error and Surface Roughness for Period-n Milling Bifurcations*, JMSE, Vol 139, 061010, (2017)

[11]   Honeycutt, A., and Schmitz, T., *A Numerical and Experimental study of Milling Bifurcations*, Nova Science Publishers, Vol 12, Chapter 2 (2016)